The HARP Time Projection Chamber

Gabriel Vidal Sitjes
Supervisors: Juan José Gómez Cadenas, Piero Zucchelli

CERN-THESIS-2003-011
01/02/2003

Febrero 2003

Universidad de Valencia, CERN

Primero hay que saber sufrir,
despues amar, despues partir

NARANJO EN FLOR
Virgilio y Homero Exposito.

CONTENTS

LIST OF FIGURES

LIST OF TABLES

ACKNOWLEDGMENTS

It is my pleasure to thank all those who have made possible this thesis. The underlying work has been carried out at CERN from November 2000 to October 2002 under the financial support of the CERN Doctoral Students Program, a grant of Collaboration from the Universidad de Valencia (SPAIN) with Professor J.J. Gómez Cadenas, and the contribution of the HARP experiment at CERN. This work has been performed under the guidance and supervision of Professors Juan José Gómez Cadenas and Piero Zucchelli to whom I am extremely grateful, not only for professional reasons but also for their invaluable friendship and enthusiasm without which this thesis would have not happened. I am equally grateful to Jean Claude Legrand for all I have learned from his experience and for his friendship. I thank Friedrich Dydak and Lucie Linssen for the numerous ideas that came out from the discussions we had and, specially, for their encouragement and enthusiasm. To be mentioned A. Braem, M. Brehm, C.David, H.G. Fisher, G. Giannini, J.L. Loquet, J. Mulon, L. Musa, M. Scandurra and R. Veenhof for their advise, professionality and help, and my colleagues A. Cervera, M. Chizhof, G. Prior, V. Serdiouk, A. Sfyrla and C. Wiebush. Last but not least I want to thank each of the members of the HARP collaboration. Special mention is for all those who have made their contribution indirectly in a human way, and from whom I will not mention their names, but, whose contribution is of utmost importance.

EXECUTIVE SUMMARY

Chapter 1 describes the aims and motivations of the HARP experiment, designed to measure the absolute and differential cross-sections of secondary hadron production over the full solid angle for proton-nuclei collisions. The energy range covered by the experiment is 2 to 15 GeV/c, and a wide collection of targers was studied. The motivation of such a measurement is the lack of experimental data necessary to calculate accurately the hadronic flux determining the atmospheric neutrino flux, that producing neutrinos in existing experiments (K2K, MiniBoone), and that relevant to the design of future neutrino facilities.

The HARP experiment is described in Chapter 2. A beam of protons and pions impinges onto fixed targets producing secondary hadrons that are measured by various sub-detectors. Each sub-detector is described briefly and its "raison d'etre" discussed.

The working principles of a Time Projection Chamber are explained in Chapter 3. A TPC is a gaseous detector with 3D tracking and particle identification capabilities. Particle detection with a TPC implies different processes, mainly gas ionization, drift of low energy electrons in the gas and avalanches generated in the wire chamber.

Chapter 4 describes the HARP TPC: the mechanical structure of the detector, the electrostatics configuration, gas mixture, analog and digital electronics, data acquisition, voltage supply system and cooling system.

Chapter 5 describes the TPC laser calibration system. This is based on a novel technique that we have developed. It consists of a number of quartz fibres, whose ends are aluminized and, that guide UV laser light. The fibre tips, located precisely inside the detector volume, act as photoelectron sources, producing the calibration signals. The technique has been tested on a TPC prototype, where the parameters relevant for the design of a system appropiate for the TPC have been measured. Such a calibration system has been designed, constructed and implemented to the HARP TPC.

Chapter 6 treats the electronic signals of the TPC readout channels. The analog signals are characterised and the methods to extract the information from the digitized signals are discussed and compared. An undesired cross-talk effect has been found in the analog frontend electronics. A series of measurements have been performed in order to localize, quantify and model the effect. The measurements consist in the excitation of a determined channel while the signal generated in all channels is recorded. The generated signals have been studied offline and the effect has been traced and modelled.

1. GOALS FOR A HADRON PRODUCTION EXPERIMENT

The HARP experiment is performing a measurement of the hadronic productions cross-section over the full solid angle. A wide range of fixed targets on a beam of protons with momentum varying from 2 to 15 GeV/c is used. Its aim is to reach an accuracy of 2%. HARP has three different goals:

- Compute the hadron flux resulting in the atmospheric neutrino flux (collisions of protons with N_2 and O_2 nuclei).
- Compute the hadronic production cross-sections of heavy targets relevant to the design of future neutrino facilities such as the "Neutrino Factory".
- Measure the hadron flux for specific setups (K2K, MiniBoone experiments) as an input to the precise calculation of neutrino the flux in these experiments.

1.1 Atmospheric Neutrinos

Atmospheric neutrinos are dominated by ν_μ , $\bar{\nu}_\mu$, ν_e and $\bar{\nu}_e$ which are produced in the hadronic showers induced by primary cosmic rays in the earth's atmosphere. Fig. 1.1 shows the measured primary comic ray spectrum. The main mechanism of production of the atmospheric neutrinos is the chain of reactions:

$$\begin{array}{rcll} p(\alpha,...) + Air & \rightarrow & \pi^{\pm}(K^{\pm}) + X & \\ & & \pi^{\pm}(K^{\pm}) \rightarrow \mu^{\pm} + \nu_\mu(\bar{\nu}_\mu) & \\ & & \mu^{\pm} \rightarrow e^{\pm} + \nu_e(\bar{\nu}_e) + \bar{\nu}_\mu(\nu_\mu) & \end{array} \quad (1.1)$$

Atmospheric neutrinos provide us with a unique tool for studying neutrino properties over a wide range of neutrino energies and for vastly differing distances between the neutrino source and a neutrino detector. These neutrinos have energies ranging from $\sim$ 0.1 GeV to several GeV and their interaction rate is of the order of 0.1 interactions per year per ton. Atmospheric neutrinos are observed directly in large mass underground detectors predominantly by means of their CC interactions:

$$\begin{array}{l} \nu_e(\bar{\nu}_e) + A \rightarrow e^-(e^+) + X\,, \\ \nu_\mu(\bar{\nu}_\mu) + A \rightarrow \mu^-(\mu^+) + X\,. \end{array} \quad (1.2)$$

In the hypothesis that the effective μ lifetime in the earth's reference frame allows all the muons to decay before reaching the ground, about two atmospheric muon neutrino / antineutrino are expected for every electron neutrino. An accurate calculation of the fluxes is made by

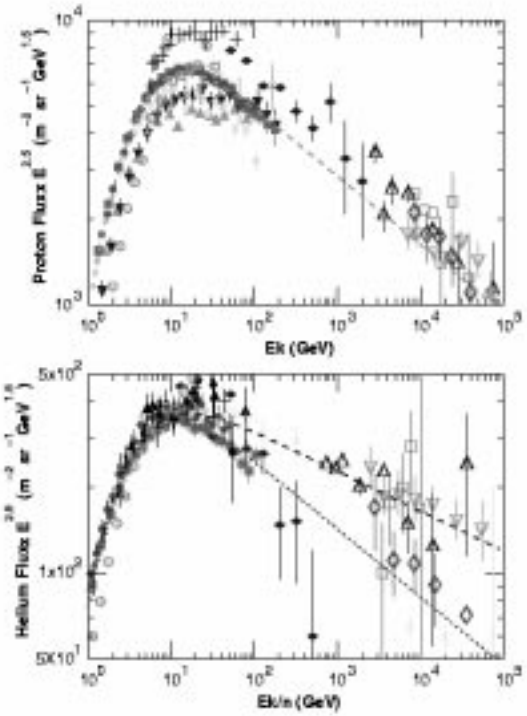

Fig. 1.1: Observed flux of cosmic-ray proton and helium. The dashed lines show the theoretical fits described in [2]. The data are: Webber [3]-crosses; LEAP [4]-upward triangles; MASS1 [5]-open circles; CAPRICE [6]-vertical diamonds; IMAX [7]-downward triangles; BESS98 [8]-circles; AMS [9]-squares; Ryan [10]-horizontal diamonds; JACEE [11]-downward open triangles; Ivanenko [12]-upward open triangles; Kawamura [13]-open squares; Runjob [14]-open diamonds. From [2].

Monte-Carlo simulation taking into account effects like geomagnetism, spectra and chemical composition of the cosmic rays, cross section of π and K production, Monte-Carlo transport of hadronic cascades in the atmosphere and calculation of neutrino energy spectra. Each of the above effects introduces some uncertainty in the calculation of the atmospheric ν flux leading to a total uncertainty of $\sim$30% in the atmospheric neutrino flux. Despite this big uncertainty, the ratio of fluxes $\frac{\Phi_{\nu_\mu}}{\Phi_{\nu_e}}$ is quite insensitive to the lack of knowledge and the uncertainty on this ratio is $\sim$ 7%. Calculations of the atmospheric neutrino fluxes predict the ν_μ/ν_e ratio to depend on neutrino energy and zenith angle of neutrino trajectory, approaching two for low energy neutrinos and horizontal trajectories but exceeding this value for higher energy neutrinos and for trajectories close to vertical, [2]. The SuperKamiokande experiment has recently measured a predicted ratio of fluxes ν_μ/ν_e of R=$0.663^{0.044}_{-0.041} \pm 0.079$, where R is the double ratio:

$$R = \frac{(\Phi_{\nu_\mu}/\Phi_{\nu_e})_{measured}}{\Phi_{\nu_\mu}/\Phi_{\nu_e})_{predicted}} \tag{1.3}$$

This deficit and its dependence with the zenith angle, together with other experimental data, has been interpretes as evidence for neutrino oscillations experienced by atmospheric neutrinos [15]. Whatever strong evidence is reported, the detailed interpretation of SK data requires reliable determination of atmospheric neutrinos fluxes.

The dominant sources of uncertainty in the atmospheric neutrino flux calculation are: (a) the poor knowledge of the primary cosmic rays energy spectrum and chemical composition and (b) the uncertainty of pion production in collisions of the primary cosmic rays with nitrogen and oxygen nuclei. Next in order of uncertainties is the neutrino-nucleon cross-section at low neutrino energies.

New measurements of the primary cosmic rays flux are consistent among them (Fig. 1.1), and a new round of long-duration balloon flights will reduce the uncertainty of the primaries spectrum and composition to negligible levels. The pion production mechanism on light nuclei is the remaining major obstacle to a precise calculation of the atmospheric neutrino flux. This uncertainty comes from the lack of experimental pion production,Sec. 1.3, data for an impinging proton(pion) momentum below 15 GeV.

1.2 Neutrino Beams

Accelerator neutrino beams have been extensively used in high energy physics during the last decades. The discovery of the neutral currents, the measurement of the Weimberg angle, the study of weak currents and of nuclear quark structure are among the highlight applications of neutrino beams performed before the 90's. From the 90's, neutrino beams have been intensively used in the search for neutrino mass and neutrino oscillations [18]. Neutrino beams are typically produced in pion and kaon decay and more rarely in muon decay. To produce a pion beam a proton beam impinges on a target producing pions which are collected by a magnetic field. The generic layout of the machines producing such beams consists of a proton accelerator, a target, a system of magnets to filter and focus the pions and a decay tunnel. Control of the neutrino beam energy and direction is achieved through the control of the pion beam [19].

Recent beams, like the Fermilab booster neutrino beam-line and the KEK PS neutrino beam-line achieve high neutrino intensity by means of a high flux of low energy protons (8 GeV/c and 12 GeV/c for the Fermilab booster and KEK PS, respectively) impinging on a fixed target. In the same direction, a new generation of neutrino beams is currently being studied: the neutrino beam of the Japan Hadron Facility (JHF) [22] and the neutrino beam of the CERN Super-conducting Proton Linac (SPL) [23]. These are conventional neutrino beams but produced from extremely intense proton beams, of the order of 4 MW, and receive the name of "Super Beams" after their high proton flux. These beams are used for neutrino oscillation experiments, for which precise knowledge of the composition of the beam and energy spectra is as important as their intensity. The required accuracy in the determination of the beam composition is only achievable through precise knowledge of the pion yield at the target and precise simulation of the beam optics. Existing data is not sufficient neither to calculate existing beams properties with the required accuracy nor to support the design of new super-beams. Because of this reason, the HARP experiment has carried out a series of measurements with the primary targets used by the Fermilab booster and KEK PS neutrino beam-lines.

The Neutrino Factory is a proposed facility in which neutrinos are produced from circu-

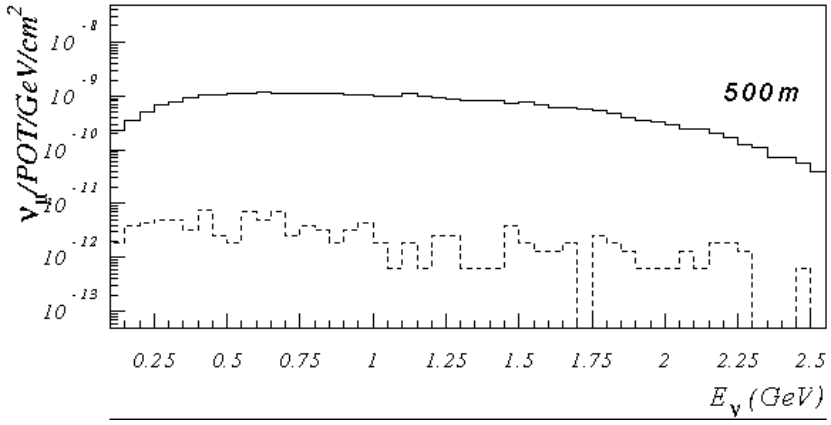

Fig. 1.2: Flux of ν_μ (solid histogram) and ν_e (dashed histogram) from a 50 m decay length beam line at 500 m, at the Fermilab booster. From [20].

lating muons decaying in a storage ring. In such a machine the muons are produced in pion decays. A high intensity (4 MW) low energy proton beam impinges on a target producing the pions. Accurate knowledge of pion production yield is a requisite for the efficient design of the target region and the choice of the proton driver energy. The Neutrino Factory concept is discussed in Sec. 1.2.3.

1.2.1 The Fermilab booster neutrino beam-line

The Fermilab booster neutrino beam-line has been built for the MiniBoone experiment [20], a ν_μ disappearance and $\nu_\mu \rightarrow \nu_e$ appearance experiment. The detector is located at 500 m from the origin of the neutrino beam. Neutrinos are produced by means of a proton beam of 8 GeV/c momentum impinging on a Berilium rod of 8 mm diameter and 55 cm length followed by a horn and a decay tunnel. The energy of the neutrino beam ranges from 0.1 to 3 GeV as shown in Fig 1.2. The proton beam intensity is 2.5×10^{13} protons per second, that allows to record 10^6 events per year in the MiniBoone Detector. If the signal they are seeking for is there they expect $\sim$ 1000 ν_e events over a background of 1700 events related to the beam contamination and 1200 events from detector misidentification. The error on the central value of the beam background is assumed in their analysis to be 10%. This accuracy relies mainly on hadron production measurements, Monte-Carlo simulations (both of hadron production and beam optics) and beam monitoring. For this reason the MiniBooNE collaboration is collaborating with the HARP experiment at CERN by joining dedicated runs meant to measure the hadron production yields onto a replica of their targets and target supports with a 8 GeV/c proton beam.

1.2.2 The KEK PS neutrino beam-line

In the K2K experiment, the KEK PS is used to produce a neutrino beam that is sent to the Super-Kamiokande detector [15], which is at a distance of 250 Km from the accelerator. The aim of the experiment is to measure ν_μ disappearance in order to verify, with accelerator

Magnitude	Range	Precision
P_L for π	100-700 MeV/c	<25 MeV/c
P_T for π	0-250 MeV/c	<25 MeV/c
# of secondary π		5%
π^+/π^- ratio		5%

Tab. 1.1: Precision requirements for Neutrino Factory design.

neutrinos, that the atmospheric neutrino deficit is due to neutrino oscillations [21]. The proton beam has a momentum of 12 GeV/c and a nominal intensity of 2.7×10^{12} protons per second, corresponding to about 150 ν_μ interactions in the Super-Kamiokande detector in a year. The small interaction rate makes the flux maximization crucial: the target is designed as a carrying current component of the central part of the focusing horn and it is transversed by a current of 250 kA. It is an Aluminum rod of 3 cm diameter and 66 cm length.

For a ν_μ disappearance measurement, a very precise knowledge of the beam flux in the far detector is required. For this reason, a front neutrino detector has been built at 300 m distance from the target in order to measure the absolute neutrino flux in absence of oscillations. Nevertheless, due to the different solid angle coverage, the far detector flux extrapolation requires detailed knowledge of the proton beam divergence and shape, pion spectrum and divergence at different longitudinal position inside the decay tunnel and neutrino energy as a function of the radial distance from the beam axis. Despite the presence of beam instrumentation (proton, muon and pion monitors) this extrapolation is only possible by Monte-Carlo simulation of pion and kaon production at the target and of the focusing system. In addition, the angle of the direction of the neutrino with the beam axis is the result of the kinematics of the decay, in which the parent particle is involved. Thus, precise knowledge of the neutrino beam that arrives to the far detector is the outcome of a model dependent analysis of the near detector and monitors. The K2K collaboration collaborates with the HARP experiment, which has performed a series of dedicated runs with a replica of the K2K target.

1.2.3 The Neutrino Factory

A neutrino factory is a proposed machine to produce neutrinos from circulating muons decaying in a storage ring. In such a machine the pion production mechanism is conventional, however they are used to produce muons. The muons are then collected, collimated by ionization cooling [16], accelerated to the desired momentum (10-50 GeV/c) and then fed into a storage ring [17]. The storage ring has two straight sections and collimated neutrino beams are emitted along them. By changing the sign of the charge of the collected pions it is possible to get the two conjugate neutrinos, $\overline{\nu}_e+\nu_\mu$ or $\nu_e+\overline{\nu}_\mu$. Again the yield of secondary pions, the π^+/π^- ratio, the longitudinal and transverse momentum distribution of the pion determine the design of the collimation and cooling devices and, at the end, the final performances of a neutrino factory.

Current simulations of the pion yield lead to discrepancies between 30 and 100% [58] due to hadro-production modeling and lack of data. We anticipate the aimed precision of the HARP experiment on the parameters relevant to the neutrino factory in Table 1.2.3.

1.3 Existing data

Existing data below 20 GeV/c are mostly from single arm hadron production experiments carried out in the seventies. The most relevant data are p-Be collisions at 24 GeV/c measured by Eichten at al [24], proton collision at 19.2 GeV/c measured by Allaby et al [25] and Abbott et al [26], p-C and P-Ta collisions at 10 GeV/c/nucleon, measured by Armutliiski et al [27] and p-C, d-C, α-C and C-C collisions at 4.2 GeV/c/nucleon measured by Agakishiyev et al [28]. More recently, the E910 experiment at BNL [29], designed for strange particle production, made some proton-nucleus measurements at proton momenta of 12 and 18 GeV/c in 1996. However, this data is difficult to interpret. The measurements done by Eichten, Allaby and Abbott did not cover the full solid angle (70 mrad in the forward direction) and model dependent extrapolations to uncovered regions lead to a 30% systematic error. The Armutliiski and Agakishiyev measurements were done with a bubble chamber detector covering the full solid angle but have low statistics (1500-2200 events per setting) and two target materials only.

2. THE HARP EXPERIMENT

As explained in Chapter 1, the HARP experiment aims to measure the absolute and differential cross-section for hadron production over the full solid angle, onto fixed targets by beams of protons and pions with momentum in the range between 2 and 15 GeV/c. This is equivalent to count the secondary particles of each species in momentum and solid angle bins:

$$\frac{d\sigma}{dpd\Omega} = \frac{N(p,\Omega)}{\phi} \tag{2.1}$$

where ϕ is the incident flux.

The HARP experimental setup allows momentum measurement, particle identification and tracking over the full solid angle with good geometrical and particle identification efficiency. To minimize costs the maximum possible existing equipment has been reused.

One of the most important sub-detectors of the experiment is a Time Projection Chamber (TPC), a three-dimensional tracking device with particle identification capabilities. This detector and its working principles are explained in detail in Chapters 3 and 4. In this chapter a brief description of all other sub-detectors and their "raison d'etre" is given.

Two main parts constitute the HARP detector (Fig. 2.1): a forward spectrometer covering the forward cone of the solid angle and a large angle spectrometer surrounding the target , covering the solid angle outside the forward cone.

In the forward spectrometer, particle identification is carried out by a threshold Cherenkov detector and a Time-Of-Flight detector, covering complementary regions of the momentum spectrum. There are also an electro-magnetic calorimeter and a muon detector to identify leptons. Momentum measurement and particle tracking in the forward spectrometer is performed by a set of Drift Chambers measuring the deviation of the particles as they transverse the magnetic field generated by a dipole magnet .

In the large angle region, particle identification is performed by the TPC, described in Chapter 4, that measures the dE/dx of the particles traversing a gas, and a Resistive Plate Chamber Time-Of-Flight detector. Momentum measurement is achieved by measuring, in the TPC, the curvature of the particles trajectories in the magnetic field generated by a solenoid.

2.1 The beam

The HARP detector was operating in the CERN PS T9 beam line, which provides charged beam particles with a momentum resolution of about 0.24% in the range from 1.0 to 15.0 GeV. Its composition depends on beam momenta and is typically dominated by protons and pions. The T9 beam is produced by protons from the PS impinging onto a primary target. The spill structure of the beam is a single 400 ms burst every 16.4 s PS cycle. Each spill provides about 2×10^{11} protons on the primary target. The flux of protons and pions produced

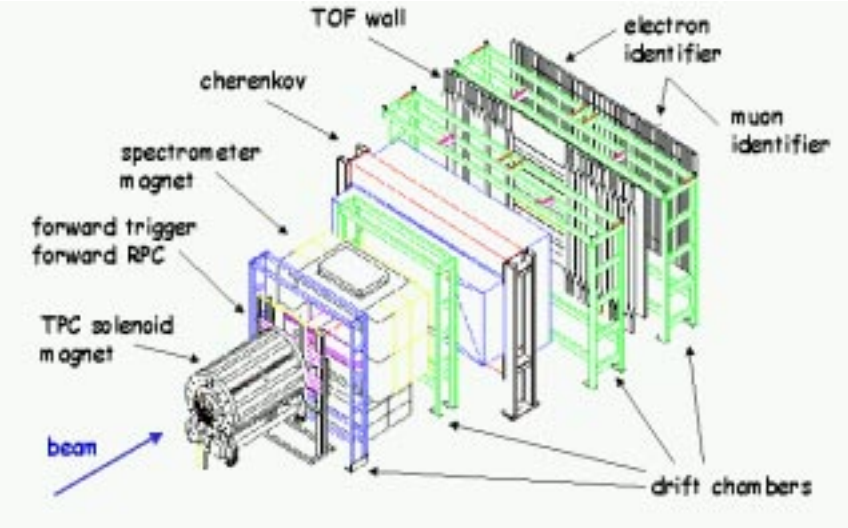

Fig. 2.1: The HARP Detector.

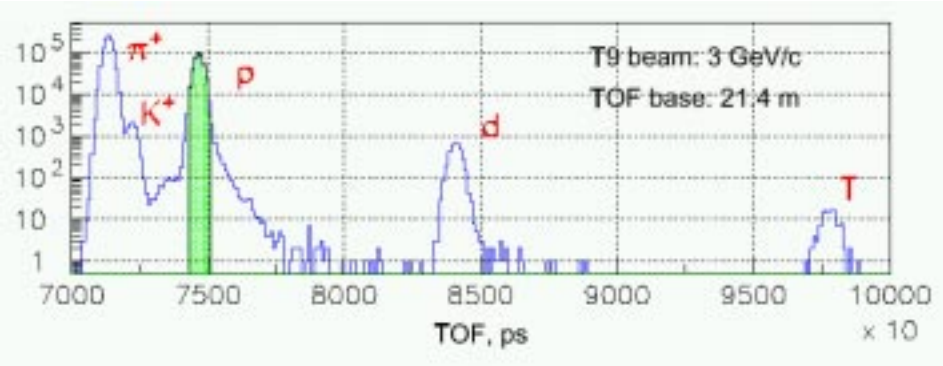

Fig. 2.2: An example of beam population.

in the primary target is about 10^5 per spill, integrated over all momentum range. A momentum selected fraction of the secondaries is transported toward the Harp experiment by an instrumented beam-line that allows us to measure accurately its composition. Beam particle identification is performed by a Time Of Flight detector and two Cherenkov detectors (BCA and BCB), located between the primary target and the HARP detector. The TOF detector is formed by two planes of scintillators, 21.4 m apart, with an overall resolution of 160 ps [40] allowing for a separation, at 3σ level, between pions and protons up to 8 GeV, pions and kaons up to 4 GeV and protons and kaons up to 7 GeV. In Fig. 2.2 the time-of-flight distribution for beam particles of 3 GeV momenta is shown. Two CO_2 gas Cherenkov detectors are installed along the beam-line. They work in threshold mode and their pressure (and therefore, their refractive indexes) are changed depending on beam momenta allowing for complementing the TOF particle identification capabilities at high beam momenta.

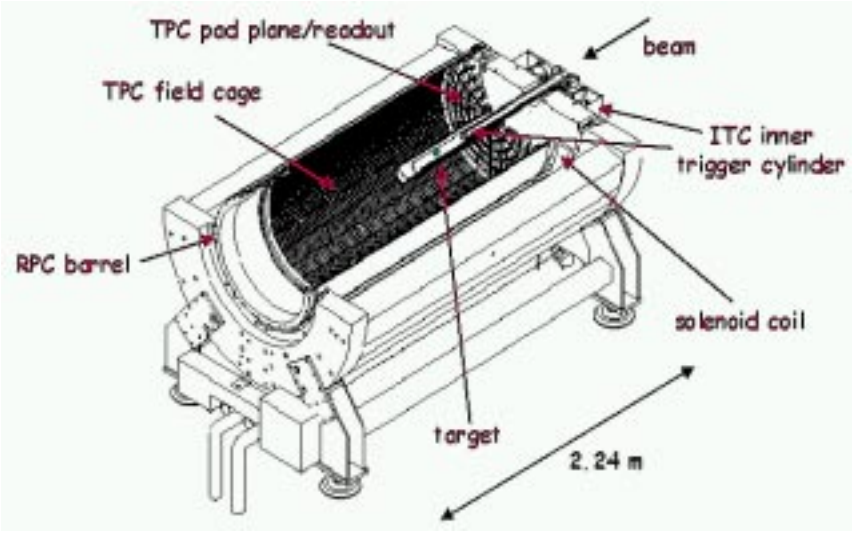

Fig. 2.3: Longitudinal section of the solenoid, TPC and target support.

2.2 The Multi Wire Proportional Chambers

Beam particles trajectories are tracked by four Multi Wire Proportional Chambers located upstream of the HARP detector, immediately upstream of the target. Each chamber is positioned perpendicular to the beam and is formed by one cathode wire plane and two anode wire planes, being the cathode plane in the middle. The three planes in one chamber are rotated by 90^o to each other allowing a simple chamber to reconstruct a three dimensional point along a beam particle trajectory with a resolution of 0.5 mm [40]. Using the information from the four chambers, the trajectory of the beam particles is obtained and extrapolated to the target with a spatial resolution of 0.8 mm [40].

2.3 The Solenoidal magnet

In the large angle region, particle momentum is determined by measuring the particle trajectory deviation due to a magnetic field[1], provided by a solenoidal magnet of 90 cm inner diameter and 225 cm length. Its global location in the experiment can be seen in Fig. 2.1 and a more detailed view of the magnet itself is shown in Fig. 2.3. The magnet consists of a copper solenoid coil, an iron return yoke and an iron end-cap for flux return at the upstream side. The downstream end of the solenoid cannot be closed by an iron end-cap since it would stop small angle particles going to the forward spectrometer. The magnet is 75 cm longer than the TPC to provide an homogeneous axial field of 0.7 T ($B_T/B_L < 1\%$) through all the TPC. Fig. 2.4 shows the MC simulated axial and radial components of the magnetic

[1] Particle trajectories are bend due to the magnetic field according to the formula:

$$P_T[GeV/c] = 0.3zB[T]R[m] \tag{2.2}$$

where z is the charge of the particle expressed as a multiple of the electron charge, B is the magnetic field, R is the radius of curvature and P_T is the particle transverse momentum with respect to the beam direction

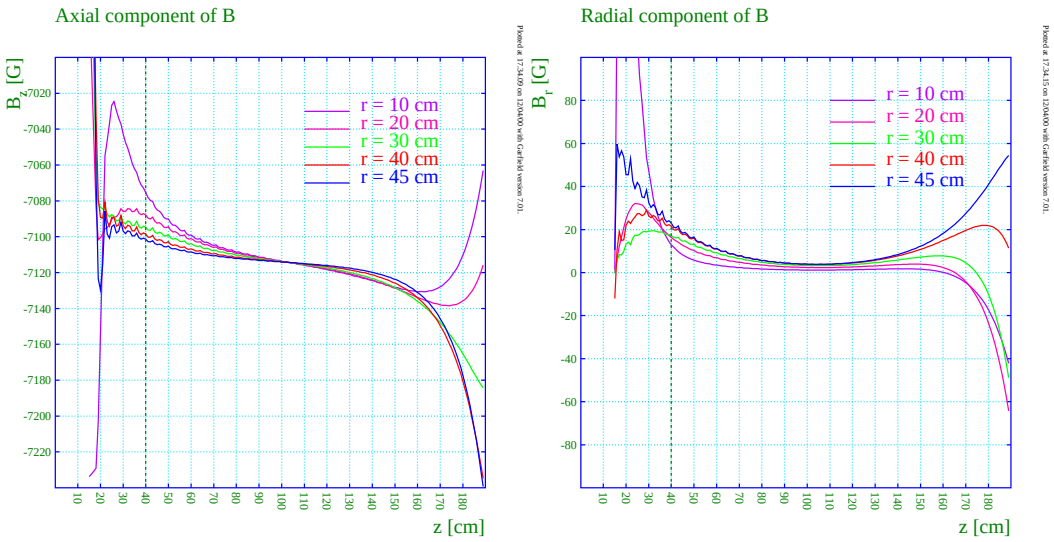

Fig. 2.4: Axial (left) and radial (right) components of the magnetic field simulated with TOSCA [34]. The vertical dotted lines correspond to the location of the downstream end of the TPC.

field generated by the solenoid.

2.4 The target

The target, where the proton interactions occur, is located inside the TPC and it is mounted on a structure that allows for a fast target change (Fig. 2.3). The TPC, in turn, sits in the magnetic field of the solenoidal magnet previously described. HARP has measured a series of solid and cryogenic targets whose features are tabulated in Tab 2.1 together with the number of events taken per target and per beam momentum setting. The solid targets are disks of 30 mm diameter and correspond to 2%, 5% and 100% of a nominal hadronic interaction length. The 2% and 5% interaction length targets are meant to minimize re-interactions while keeping a reasonable hadronic interaction rate. The 100% radiation length targets are used for checking the simulation of re-interactions. A number of targets with different forms have been used in order to test the vertex reconstruction.

2.5 The Resistive Plate Chambers

Between the TPC and the solenoid of the magnet there is a Resistive Plate Chamber detector. The detector is composed by 30 units, $200\times15\times1$ cm^3, that surround the TPC barrel. The units are disposed in two overlapping layers of 15 chambers each. Each chamber is formed by two double-gas-gaps RPC with pick up electrodes between the two double-gaps and a central pad plane between the pick up electrodes (Fig. 2.5). The gas gaps are 0.3 mm wide and are separated by sheets of insulating glass of 0.7 mm thickness. The gas is a mixture containing $C_2F_4H_2/SF6/C_4H_{10}$ at proportions 90/5/5 respectively. The pad plane is divided into 7 pads in the longitudinal direction. Each pad is readout on both sides by stan-

Target	+3 GeV/c	+5 GeV/c	+8 GeV/c	+12 GeV/c	+15 GeV/c
Be 2% λ	2.2	2.3	—	5.9	1.8
Be 5% λ	1.54	1.95	2.23	0.63	0.91
Be 100% λ	1.16	1.09	1.09	1.81	0.74
C 2% λ	2.4	—	—	—	2.7
C 5% λ	1.63	3.37	2.27	2.15	0.81
C 100% λ	1.11	1.12	1.01	0.66	0.96
Al 2% λ	2.4	2.1	—	3.8	2.3
Al 5% λ	1.93	2.07	2.22	0.73	0.71
Al 100% λ	1.34	1.29	1.27	1.15	0.70
Cu 2% λ	3.6	1.5	—	2.0	3.0
Cu 5% λ	1.16	2.49	2.95	0.85	0.65
Cu 100% λ	1.12	1.58	1.40	1.93	0.83
Sn 2% λ	1.3	—	—	—	2.2
Sn 5% λ	1.87	3.25	3.15	2.05	0.63
Ta 2% λ	4.9	1.5	—	1.6	2.6
Ta 5% λ	2.62	2.38	2.33	1.04	0.62
Ta 100% λ	2.11	1.33	1.49	1.56	0.61
Pb 2% λ	4.4	1.5	—	2.5	2.3
Pb 5% λ	2.49	3.41	3.32	0.72	0.64
Pb 100% λ	1.76	1.26	0.98	1.12	1.10
H_2	6.2	3.9	2.5	2.4	1.8
D_2	4.4	4.1	2.6	1.1	0.9
N_2	4.2	2.9	1.4	1.0	1.1
O_2	1.8	1.4	0.7	1.6	2.9
Target	-3 GeV/c	-5 GeV/c	-8 GeV/c	-12 GeV/c	-15 GeV/c
Be 2% λ	0.2	0.76	—	1.2	1.3
Be 5% λ	2.33	1.39	1.76	1.21	0.85
C 2% λ	—	—	—	0.86	1.1
C 5% λ	2.26	1.81	1.63	0.74	0.62
Al 2% λ	0.27	0.79	—	0.88	0.90
Al 5% λ	2.17	1.11	1.38	0.75	0.62
Cu 2% λ	—	—	—	1.11	0.7
Cu 5% λ	3.20	1.23	2.28	0.85	1.06
Sn 2% λ	—	—	—	—	1.2
Sn 5% λ	2.08	1.82	1.58	1.35	0.27
Ta 2% λ	0.82	0.80	—	0.6	2.1
Ta 5% λ	1.66	1.60	1.38	1.03	0.40
Pb 2% λ	0.94	0.34	—	0.7	1.4
Pb 5% λ	1.54	2.33	1.65	1.92	1.08
H_2	1.0	0.9	0.7	0.8	0.8
D_2	0.7	0.6	0.5	0.6	0.7
N_2	1.0	1.7	0.7	0.4	0.9
O_2	1.3	0.9	0.8	0.6	0.5
Special Targets					
K2K replica at 12.9GeV/c	4.05				
MiniBoone Be replica at 8 GeV/c	7.0				
Cu “skew” at 12 GeV/c	1.71				
Cu “button” at 15 GeV/c	0.24				
H_2O (10%) λ at 1.5 GeV/c	3.5				
H_2O (100%) λ at 1.5 GeV/c	2.9				

Tab. 2.1: Summary of the number of recorded events per setting. Event number units are Million events.

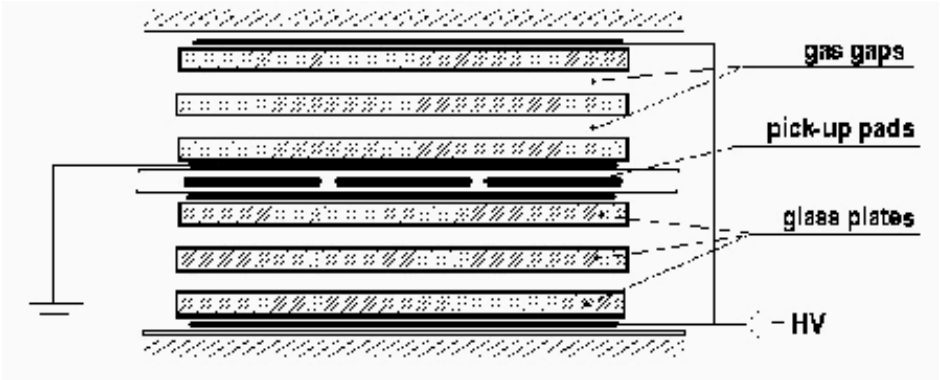

Fig. 2.5: Section of an RPC.

dard ADCs and high resolution TDCs. With this configuration the HARP RPCs have a time resolution better than 150 ps and an efficiency better than 99% as measured in a test beam.

The purpose of the HARP RPCs is particle identification of large angle particles inside the TPC by time-of-flight measurement. Particularly, the aim to distinguish between electrons and pions between 150 and 250 MeV/c, where no separation can be done by dE/dx measurement in the TPC. With the time resolution of the RPC this can be statistically resolved since the difference in time of flight between e and π at 250 MeV for the shortest path length in the TPC (45 cm) is 220 ps.

Downstream of the TPC, before the spectrometer dipole, there is a planar RPC detector consisting of eight chamber modules in the horizontal direction and eight in the vertical direction. This plane serves for the same purpose as the barrel RPC, covering the smaller production angles.

2.6 The Spectrometer magnet

The downstream spectrometer measures high-momentum small production angle ($\theta < 17^o$) tracks. The structure of the spectrometer magnet can be seen in Fig. 2.1. It provides a vertical magnetic field of 0.5 T and its bending power is 0.68 Tm, thus deviating the trajectories of charged particles according to the formula:

$$\theta = \frac{0.3zdB}{p_{||}} \quad \frac{[m][T]}{[GeV]} \tag{2.3}$$

where $p_{||}$ is the component of the particle momentum projected on the horizontal plane. For example, the angular deflection is 40 mrad for a particle with $p_{||}$ = 5 GeV.

2.7 The Nomad Drift Chambers

Particle tracking in the forward direction is provided by 23 drift chambers from the NOMAD experiment [37]. Since these drift chambers where designed to be an active neutrino target, they are more massive than ordinary drift chambers. Each chamber consists of three gas gaps

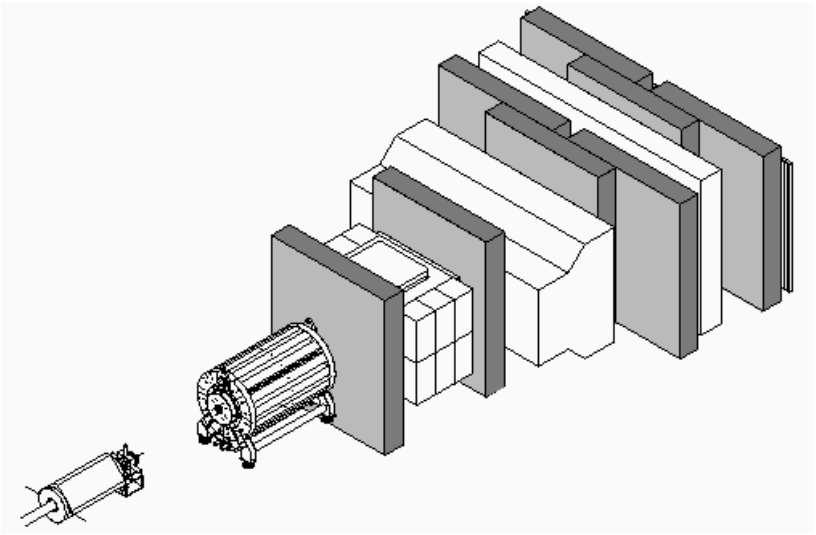

Fig. 2.6: Location of the NOMAD Drift Chambers (grey shade).

(8 mm) separated by 1.5 cm of honeycomb-structured panels representing 2% of a radiation length. Inside each of the three gas gaps there is a plane of sense wires, the central one being vertical and the first and third ones being rotated by +5 and -5 degrees, respectively. The chambers, in HARP, are filled with a gas mixture containing $Ar/CO_2/CH_4$ at proportions 90/9/1. The gas mixture used for HARP is different from that used in the NOMAD experiment (Ar/CH_4 at $50/50$ proportions) in order to obey to stricter rules in terms of flammable gas safety. The wires are now maintained at 1800 V voltage. The signal is read directly from the sense wires through a preamplifier, a fast discriminator and a TDC. A particle typically creates a signal on the three wires of a chamber allowing a 3D measurement of a point on the trajectory is reconstructed.

The drift chambers are grouped in eight modules containing four chambers each. The position of the modules (Fig. 2.1) is that to provide maximum geometrical acceptance. The Drift Chambers, in the NOMAD experiment typically had 97% efficiency, 150 μm for normally incident particles, 700 μm for 45^o tracks, and a minimum track separation of 1mm. This good resolution came as a result of a refined alignment of the wires using the muon halo of the beam [38]. In HARP a similar procedure is being carried out although the chamber efficiency is expected to be limited to $\sim$93% due to the different gas mixture and this complicates the reconstruction algorithms.

2.8 The Cherenkov Detector

The Cherenkov detector (Fig. 2.1) has been designed and built explicitly for the HARP experiment. Its dimensions have been chosen for a 95% acceptance of pions capable to provide a signal. The detector is filled with C_4F_{10}, a high density gas with high refraction index allowing the detector to be operated at atmospheric pressure and in threshold mode. The momentum threshold for pions, kaons and protons is 2.6, 9.3 and 17.6 Gev/c respectively. The main chemical and physical characteristics of the gas are listed in table 2.8.

Boiling point (C)	-2
Molecular weight (g / mol)	238.0
(n-1)$\times 10^6$	1415
y_{thr}	18.8
Pion Threshold (Gev / c)	2.6
Kaon Threshold (Gev / c)	9.3
Proton Threshold (Gev / c)	17.6
θ_c^{max} (mrad)	53
$d^2N/dxdE$ (photons / cm / eV)	1.04

Tab. 2.2: C_4F_{10} main chemical and physical properties.

The light produced in the gas is guided by mirrors toward Winston cones and reflected onto 38 photo-multipliers where the signal is detected and read out. The detector is capable of recording the emitted light intensity thus being able to distinguish between particles above threshold according to the known relation:

$$N_{p.e.} = LN_0 sin^2\theta \tag{2.4}$$

where θ is the emission angle, known by momentum hypothesis, L is the path-length in the radiator, which depends on geometry, and N_0 is a calibration constant that can be determined on data.

2.9 The Time Of Flight wall

Complementing the Cherenkov particle identification a Time-Of-Flight detector is installed 10 m downstream of the target to identify the low momentum (p<3.5 GeV / c) particles. It consists of a two layer 20 m^2 wall made of plastic scintillator. The plastic scintillator used is NE110, which has a fast response suitable to achieve a good timing, and the detectors achieve 160 ps time intrinsic resolution. There are two types of slabs according to their size: 28 slabs of $210 \times 21 \times 2\ cm^3$ and 46 slabs of $300 \times 21 \times 2\ cm^3$. All of them are wrapped in a thin aluminum sheet and in black plastic, and are equipped with light guides and Phillips XP2020 photo-multipliers at both ends. An optical fiber is connected to the center of each scintillator through a prism which is glued on the scintillator. For calibration, the scintillators are fed, via optical fibers, with laser pulses of 532 nm wavelength and 65 ps duration (FWHM). Laser calibration, cosmic ray calibration and correction for time of walk have currently allowed to achieve an overall resolution of $\sigma \sim 200\ ps$, as shown in Fig. 2.7.

2.10 The Electron and Muon identifiers

The downstream end of the forward spectrometer is formed by an electro-magnetic calorimeter and a muon wall. The purpose of the electron calorimeter is twofold: detect knock-on electrons, produced by a pion in the Cherenkov detector, that could fake pions time-of-flight and detect photons coming from neutral pion decay. For the latter purpose a 2 cm thick iron layer is installed upstream of the electro-magnetic calorimeter to convert the photons

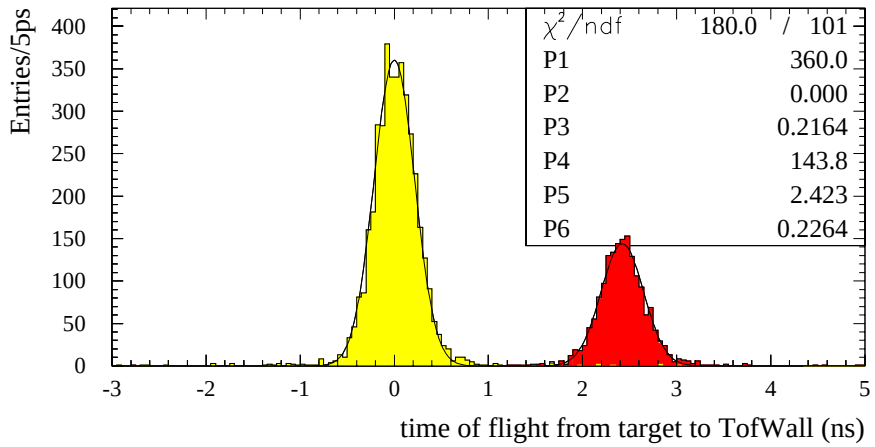

Fig. 2.7: Time-of-flight for 3 GeV/c π (left) and p (right), as measured in HARP for the beam particles. A resolution of $\sigma \sim 220\ ps$ is achieved.

into electrons and three NOMAD drift chambers are installed between the iron layer and the calorimeter with the purpose of reconstructing the photon position.

The muon identifier, called "muon wall" in Fig. 2.1, is a scintillator iron sandwich sampling calorimeter, detecting muons going through the calorimeters and the shielding. Its purpose is to monitor the muon content of the beam, due to beam pions decay, allowing a correct flux normalization.

2.11 The trigger detectors and logic

There is a set of detectors for trigger purposes. Under normal running conditions there are two kinds of triggers: beam triggers and interaction triggers. The first indicating the presence of a desired beam particle and the latter the presence of an interaction in the HARP target, being the second one correlated with the first one. The trigger logic can be adapted to the the performance of the data-acquisition system, the performance and properties of the beam, the main features of the interactions in the target and the required data sample. Fig. 2.8 shows a schematic layout of the detectors used for triggering.

The beam trigger is composed of the beam Cherenkovs explained in Sec. 2.1, two beam halo scintillators (Halo-A and Halo-B), with different acceptance, which veto the non collimated part of the beam and a Target Defining Scintillator disk (TDS) defining a target fiducial volume. Particles coming from interactions in the target are detected by two different trigger detectors according to their polar production angle. Large angle particles are detected by the Inner Trigger Chamber (ITC), a triple layer of scintillating fibers surrounding the target along the beam direction and providing an overall efficiency above 99%. Secondary particles at small production angles are detected by a Forward scintillating Trigger Plane (FTP), located downstream of the TPC. The FTP is formed of two perpendicular planes with seven scintillator units each and a hole of 6 cm diameter to avoid false triggers originated by beam particles. The Cherenkov detector (Sec. 2.8) also has a role in the trigger system at low beam

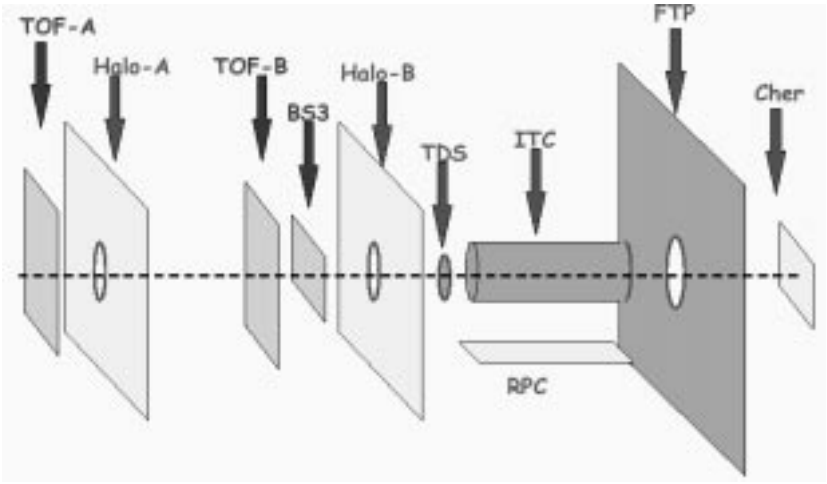

Fig. 2.8: Trigger Detectors.

momentum. At beam momentum below 4 Gev/c proton production dominates over pion production. The pion/proton separation capabilities of the Cherenkov detector are used to enrich the data with pion production.

3. PRINCIPLES OF DRIFT CHAMBERS

A Time Projection Chamber is a gaseous detector with 3D tracking and particle identification capabilities. It consists of a gas volume and a wire chamber immersed in an electric field often complemented by a parallel magnetic field. A charged particle traversing the volume interacts with the gas molecules resulting in both excitation and ionization of the gas molecules along the particle's trajectory. Electric and magnetic fields are set and oriented to make the generated electrons drift toward the wire chamber at constant velocity. The wire chamber records the 2D position of the drifting electrons in the plane perpendicular to the drift direction. The remaining coordinate is determined by the electrons drift time, which is the difference between the time of their arrival to the wire chamber and that of the passing particle, typically recorded by an external system, i.e. the trigger. The gas, its temperature and pressure, and the electro-magnetic field are chosen and tuned to produce a constant and uniform drift velocity in the gas volume. Presence of a magnetic field allows momentum determination by measuring track curvature. Energy loss measurement is possible by recording the signal amplitude and proper detector calibration. Combined measurement of energy loss and momentum provides particle identification. Particle detection with a TPC involves many different physical phenomena that can be gathered in three main groups: those related to gas ionization (Sec. 3.1), those related to the drift of the electrons (Sec. 3.2) and those related to the creation of the signals at the wires (Sec 3.3).

3.1 Gas Ionization

3.1.1 Energy loss

The most probable interaction between a fast charged particle and a gaseous medium is the incoherent Coulomb interaction, which results, on one hand, in excitation and ionization of the gas molecules and on the other in particle energy loss. Other electro-magnetic processes like bremsstrahlung, Cherenkov emission and transition radiation emission are negligible, in terms of contribution to particle energy loss, for particles heavier than electrons. Electromagnetic energy loss is the result of a number of discrete interactions and, therefore, has the characteristics of a statistical process. Bethe and Bloch derived an approximation of the average energy loss per particle trajectory unit length due to Coulomb interactions in the framework of relativistic quantum mechanics:

$$\frac{dE}{dX} = -\kappa \frac{Z}{A}\frac{\rho}{\beta^2}(ln\frac{2m_e c^2\beta^2 E_M}{I^2(1-\beta^2)} - 2\beta^2 - \delta - 2\frac{C}{Z}) \tag{3.1}$$

$$\kappa = \frac{2\pi N z^2 e^4}{m_e c^2} = 0.154 \;\; MeVg^{-1}cm^2 \tag{3.2}$$

where N is the Avogadro number, m_e and e are the electron mass and charge, Z, A and ρ are the atomic number and mass, and the density of the medium, respectively, I is its effective

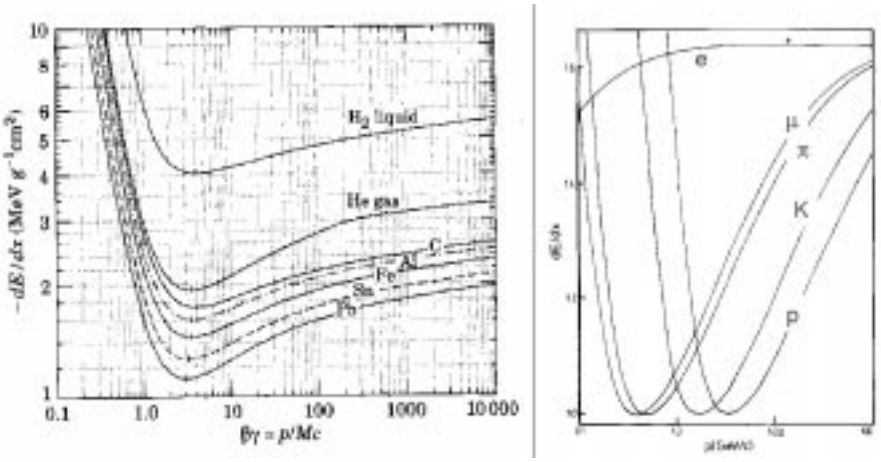

Fig. 3.1: Left plot: Reduced energy loss in different liquid materials Right plot: dE / dx as a function of the particles momentum for μ, π, p and d traveling in a Ar/CH_4 mixture at 80 / 20 proportion.

ionization potential, z is the charge and β the velocity of the particle (in units of the speed of light c). E_M is the maximum energy transfer allowed in each interaction, that can be estimated:

$$E_M = \frac{2mc^2\beta^2}{1-\beta^2} \tag{3.3}$$

δ and C are the corrections for the density and shell effects respectively [53]. It is useful to substitute the length X by a reduced length defined as x=Xρ, and then, the reduced energy loss is simply:

$$\frac{dE}{dx} = \frac{1}{\rho}\frac{dE}{dX} \tag{3.4}$$

as plotted in Fig. 3.1 (left). An approximation of the effective ionization potential is $I = 12$ Z eV, however various experimental measurements are published [42].

In formula 3.1 the energy loss depends only on the particle's velocity β and not on its mass. Thus, for particles of known momentum, measuring the quantity dE / dx provides particle identification. The main features of dE / dx as a function of β are a fast decrease with particle momenta, dominated by the β^{-2} term, followed by a constant value, called Minimum Ionizing Region, and a slow increase for $\beta \to 1$ called the "relativistic rise". Different particles reach the minimum ionizing region at different energies, at a typical momentum value of a few hundred MeV, Fig. 3.1. The non localized nature of the ionization process sets a limit to the best tracking accuracy. For example, in argon, this limit has been computed to be between 20 and 30 μm [41].

3.1.2 Energy loss distribution

In thick materials , the total energy lost by a particle is the result of a large number of interactions and the distribution of energy loss has a Gaussian shape. On the contrary, in thin materials, the total energy loss is the energy lost through a small number of interactions, each with a wide range of possible energy transfers, and its distribution is not Gaussian. For

this case, an approximation to the energy loss distribution, f, was derived by Landau in a classical framework to be[53]:

$$f(x,\Delta) = \frac{\Phi(\lambda)}{\xi} \tag{3.5}$$

where x is the thickness of the absorber and Δ the energy lost in it. The function $\phi(\lambda)$ is defined as:

$$\Phi(\lambda) = \frac{1}{\pi}\int_0^\infty e^{-ulnu-u\lambda} sin\pi u du \tag{3.6}$$

and only depends on the parameter λ which, at its turn is related with the parameter ξ as

$$\lambda = \frac{1}{\xi}[\Delta - \xi(ln\xi - ln\epsilon + 1 - C)] \tag{3.7}$$

where C is the Euler constant and

$$ln\epsilon = ln\frac{(1-\beta^2)I^2}{2mc^2\beta 2} + \beta^2 \tag{3.8}$$

The parameter ξ depends on the most probable energy loss [53]:

$$\Delta_{mp} = \xi[ln(\xi/\epsilon) + 0.198 - \delta] \tag{3.9}$$

where δ represents the density effect (Sec. 3.1.1). Allison and Cobb published [31] a Monte-Carlo Approach consisting in dividing the absorber into thin slices and choose the energy transfer randomly from the distribution in Fig. 3.2 (left). Fig. 3.2 (right) shows the comparison between the two models mentioned above for the specific case of Ar-CH_4 (93/3 proportions).

3.1.3 Relation energy loss-number of electrons produced

The energy lost by the particle is mainly used in gas ionization, complemented by atomic and molecular excitation. The total number of electron-ion pairs generated in a medium by a ionizing particle is proportional to the total energy lost by the particle in the medium:

$$n_T = \frac{\Delta E}{W_i} \tag{3.10}$$

where ΔE is the total energy lost by the particle in the gas volume considered and W_i is the effective average energy that produces one electron/ion-pair. Experimental data are reported in Fig. 3.3.

3.2 Motion of charges in a gas

Charges produced by an ionizing particle undergo multiple collisions with the electrons of the gas molecules and thermalize. The collective thermal motion of the charges while this process is called diffusion. Even in presence of an external E/B field on the collisions of the charges with the gas affect significantly the drift properties.

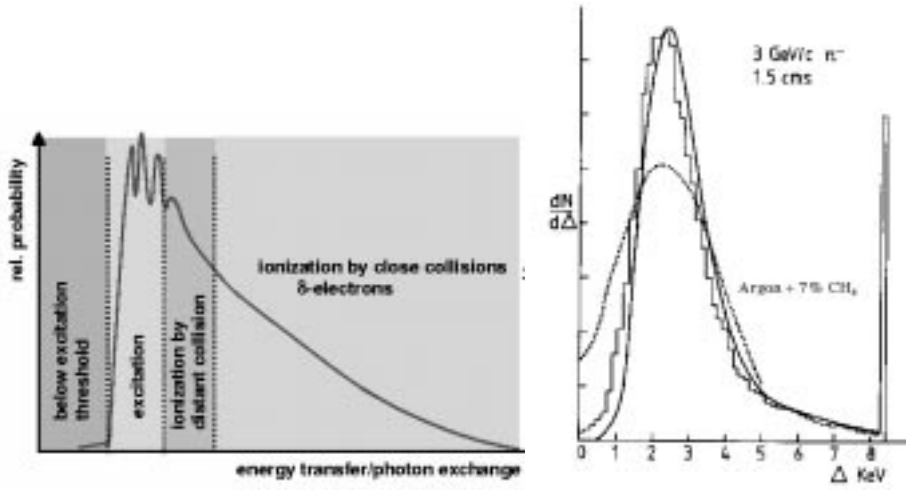

Fig. 3.2: Right plot: Schematic relative probability for different processes occur as a function of the energy transfer. From [49]. Left plot: Comparison of energy loss by 3 GeV/c pions in a mixture of Argon-Methane at proportions 93-7%. The histogram corresponds to data [32], dotted curve corresponds to the Landau approximation and the solid curve to the Allison and Cobb approximation [31].

3.2.1 Free ion and electron diffusion

In absence of any external field the charges thermal energy distribution is:

$$F(\epsilon) = c\sqrt{\epsilon}e^{-\frac{\epsilon}{KT}} \tag{3.11}$$

and the average value of the thermal energy is $\epsilon_T = (3/2)KT \sim 0.04$ eV [41].

A localized distribution of charges diffuses by multiple collisions following a gaussian law:

$$\frac{dN}{N} = \frac{1}{\sqrt{4\pi Dt}}e^{-\frac{x^2}{4Dt}}dx \tag{3.12}$$

being dN / N the fraction of charges present in the element dx at a distance x from their origin after a time t. D is the diffusion coefficient that determines how the cloud of charges expands in the gas volume. Calling σ_v the radius of the sphere containing 68.27% of the charges, then:

$$\sigma_v = \sqrt{6Dt} \tag{3.13}$$

Due to the small mass of electrons, the corresponding diffusion coefficient is typically significantly larger than that of ions.

3.2.2 Ion and electron drift in the presence of an external electric field

When in an electric field, in addition to the instantaneous and randomly oriented thermal velocity c, there is a net movement along the electric field with net velocity equal to the

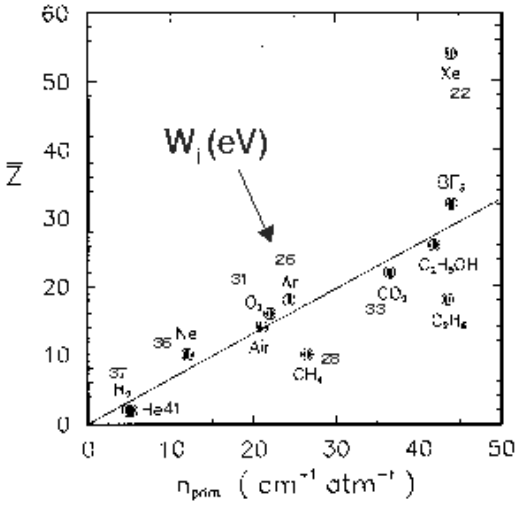

Fig. 3.3: Number of primary electrons generated by an ionizing track and effective average energy needed to produce an electron / ion pair for different materials as a function of their atomic number [54].

charge acceleration multiplied by the average time elapsed between collisions:

$$\vec{u} = \frac{e\vec{E}}{m}\tau \tag{3.14}$$

where τ can be expressed in terms of the collision cross-section and the number density N:

$$\frac{1}{\tau} = N\sigma c \tag{3.15}$$

This microscopic average velocity between two collisions appears macroscopically as the drift velocity. In a macroscopic frictional-motion picture, the equation of motion of the particle is:

$$\frac{m}{k}\frac{d\vec{u}}{dt} = \frac{e}{k}\vec{E} - \vec{u} \tag{3.16}$$

where k describes a frictional force proportional to $\vec{u}$, and the ratio m/k has the dimensions of a characteristic time. The solution of Eq. 3.16 for $t >> m/k$ is a state for which $d\vec{u}/dt = 0$ and the drift velocity is:

$$\vec{u} = \frac{e\vec{E}}{k} \tag{3.17}$$

Comparing the microscopic and macroscopic pictures we see that the macroscopic characteristic time m/k corresponds to the microscopic average time between collisions τ.

The drift velocity of the ions, u^+, is linearly proportional to the reduced field E / P, P being the pressure of the gas. This is due the fact that σ, and thus, τ is independent of the electric field up to very high fields. The quantity:

$$\mu^+ = \frac{u^+}{E} \tag{3.18}$$

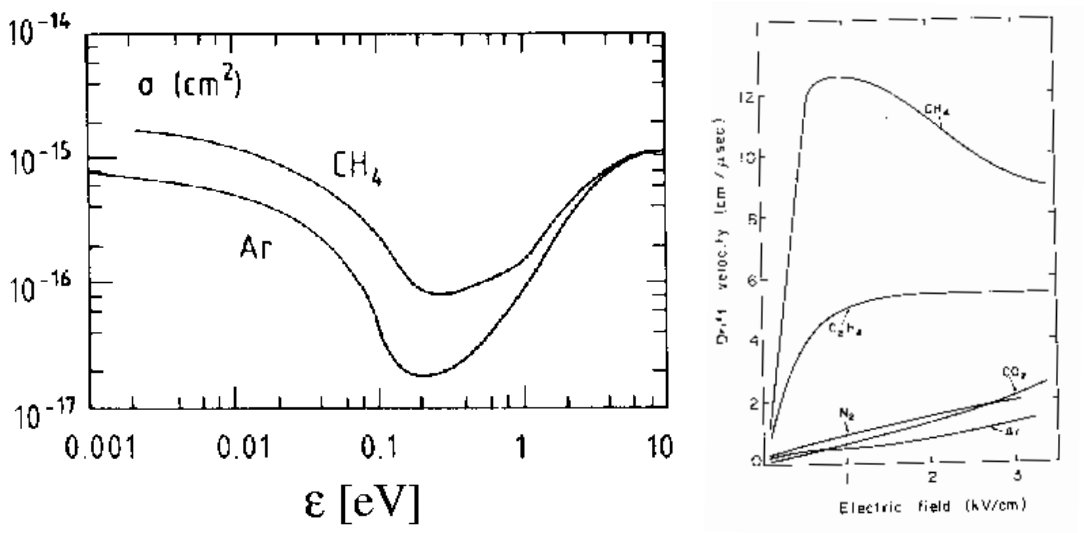

Fig. 3.4: Left plot: cross-section for electrons in argon as a function of their energy. Right plot: drift velocity of electrons in several gases at normal conditions.

is defined as the ion mobility and is specific for each ion and gas. Mobility and diffusion are related according to:

$$\frac{D^+}{\mu^+} = \frac{KT}{e} \tag{3.19}$$

Drifting ions diffuse according to equation 3.12, and the standard deviation is given by 3.13, that can be expressed in terms of the electric field:

$$\sigma_x = \sqrt{2Dt} = \sqrt{\frac{2KTu^+t}{eE}} = \sqrt{\frac{2KT}{eE}x} \tag{3.20}$$

Therefore, σ_x does not depend neither on the nature of the ion nor of the gas.

Drift of electrons differs from that of ions because for these the mobility is not constant, except for very low fields. The drift velocity of electrons can be written as:

$$u = \frac{e}{2m}E\tau \tag{3.21}$$

τ being the mean time between collisions. It has been found that the collision cross-section, and therefore τ, for some gases depends very strongly with the electric field. This dependence comes from the complex interactions that take place between the drifting electron and those of the molecular shells. This effect is called “Ramsauer effect” and one of its consequences is that the electrons energy distribution does not follow the maxwell probability distribution and the electrons average energy can exceed the thermal value by several orders of magnitude. This results in a non linear dependence of the drift velocity with the electric field (Fig. 3.4). Another consequence of the Ramsauer effect is that the addition of even small fractions of other gases changes slightly the electrons average energy and thus the drift properties (Fig. 3.5).

Rigorous theory of electron drift exists and fits very well the experimental measurements which are available for various gas mixtures [55].

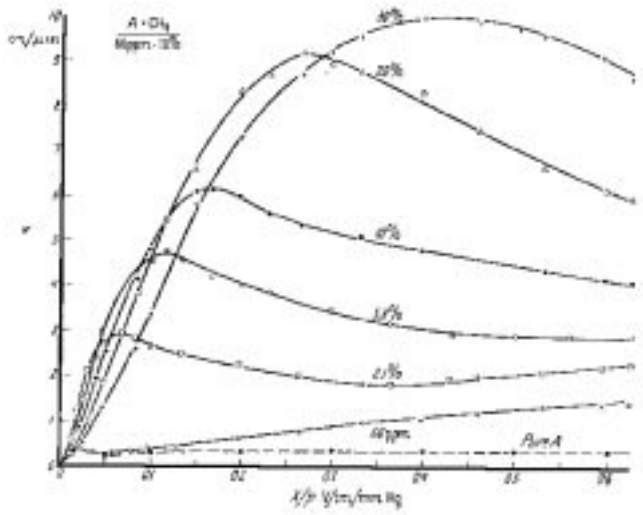

Fig. 3.5: Drift velocity of electrons in different mixtures of Argon and methane.

3.2.3 Diffusion of electrons in a magnetic field

When in addition to the electric field there is a magnetic field, the drift of electrons is modified. Between collisions, the electrons trajectories are helices rather than straight lines. For the particular case of parallel electric and magnetic field, the projection of the trajectory in the plane perpendicular to the fields direction becomes a circle. The mean free path projection in the plane perpendicular to the fields, is therefore smaller than in the absence of magnetic field. On the contrary, the projection of the trajectory along the fields direction is not affected by the presence of the fields. The conclusion is that the longitudinal diffusion does not depend on the magnetic field, while the transverse diffusion is reduced. The quantitative reduction is:

$$\frac{D_T(w)}{D_T(0)} = \frac{1}{1 + w^2\tau^2} \tag{3.22}$$

3.2.4 Electron attachment

In gas mixtures, a very effective process of charge transfer between positive ions takes place by charge transfer to the molecules with lowest ionization potential after a small drift length. Typically it takes between 100 and 1000 collisions for an ion to transfer its charge to a molecule with lower ionization potential, depending on its nature and on the difference in ionization potentials. Mean paths for ion-gas collisions are of the order of 10^{-5} cm under normal conditions [41], thus, after a drift length $\sim 10^{-3} - 10^{-2}\, p^{-1}$ cm there is only one kind of ion, where p is the percentage of lowest ionization molecules.

If electro-negative pollutants are present in a gaseous detector a fraction of the ionization electrons are captured by the pollutant gas molecules, and, the signal is reduced. Electron capture cross-section depends on electron energy and, thus, on electric field. Typical electro-negative pollutants are oxygen and water, which have an attachment probability per collision of 2.5×10^{-5}, Tab. 3.2.4, while attachment probability is negligible for hydrogen

Gas	h	N (sec^{-1})	t (sec.)
CO_2	6.2×10^{-9}	2.2×10^{11}	0.71×10^{-3}
O_2	2.5×10^{-5}	2.1×10^{11}	1.9×10^{-7}
H_2O	2.5×10^{-5}	2.8×10^{11}	1.4×10^{-7}
Cl	4.8×10^{-4}	4.5×10^{11}	4.7×10^{-9}

Tab. 3.1: Electron attachment probability per collision, average number of collisions and average time before attachment [41].

and noble gases. The effect of a fraction of pollutant can be roughly estimated with the formula [41]:

$$n = n_0 e^{-x/\lambda_c} \tag{3.23}$$

where n is the remaining number of electrons, of a cloud of originally n_0 electrons, after having travelled a distance x. λ_c is the mean free path for electron capture:

$$\lambda_c = \sqrt{\frac{m_e}{2\epsilon}} \frac{w}{Nhp\sigma(\epsilon)} \tag{3.24}$$

where ϵ is the electric field, w the electron drift velocity, m_e the electrons mass, h the attachment probability, p the fraction of pollutant and N the number of gas molecules per unit volume. As an example, a 1% air pollution in Argon, where electrons drift due to a 500 V/cm electric field, removes about 33% of the drifting electrons per cm.

3.3 Amplification on the sense wires

Typically a few tenths of electrons per cm of track are produced by an ionizing particle. Amplification is commonly achieved by generating electron avalanches around wires held at high potential. As an electron approaches a high voltage wire it feels an increasing field and increases its average energy between collisions. When the energy of an electron is bigger than the first ionization potential of the gas, different processes may occur in its next collision with different probabilities depending on the electron energy. Fig. 3.6 shows the cross section for the different processes that can occur when a collision takes place: elastic scattering, excitation leading to photon emission and ionization. Avalanche multiplication is based on the process of ionization by collision. The inverse of the mean free path of the ionization phenomena is called the First Townsend coefficient α and it represents the number of ion pairs produced per unit length of drift. If there are n electrons at a given position, after a path dx, the increase in their number can be approximated by:

$$dn = n\ \alpha\ dx \tag{3.25}$$

Integration of this formula from the point where the electrons leave the constant electric field zone to the surface of the wire, leads to:

$$n_{final} = n_{initial} e^{\int_{x_i}^{x_f} \alpha(x) dx} \tag{3.26}$$

In case of α independent of the electric field Eq.3.26 turns into $n_f(x) = n_i e^{(\alpha\ x)}$.

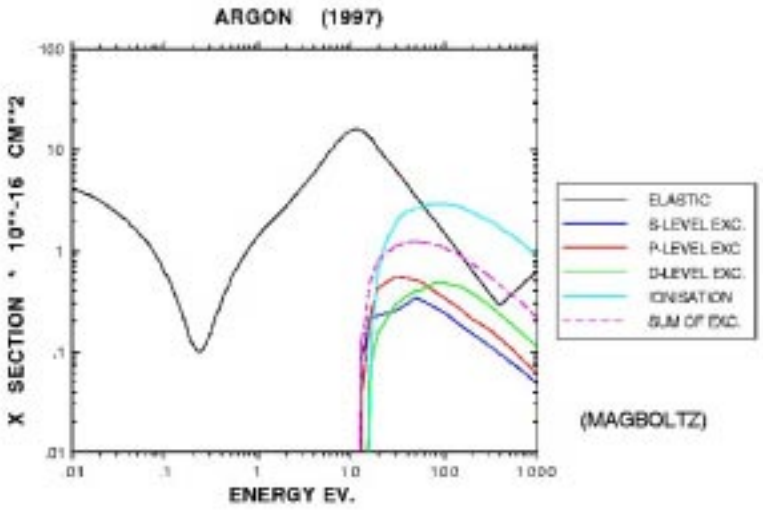

Fig. 3.6: Cross section for elastic scattering, excitation leading to photon emission and ionization as a function of electron energy [33].

Due to the statistical nature of the amplification process, the final number of electrons generated by a given number of initial electrons has a gaussian distribution when the amplification is large. The average ratio $n_{final}/n_{initial}$ is called gain and in practice it is measured for each experimental conditions. Space and time development of the avalanches is typically studied by means of detailed Monte-Carlo simulation of the detector and wires geometry, electric field and gas quality. The electrons produced in the avalanches are collected very rapidly by the wires (typically in less than 1 ns), while a cloud of positive ions is formed behind and moves slowly toward the cathode. The form of the cloud of ions is quite complex but it is worth to note that approximately half of the charges are produced in the last electron ionization mean free path.

3.3.1 Quencher gases

Polyatomic molecular gases have many excited states and many non radiative deexcitation modes. For this reason, avalanche multiplication occurs at lower fields for noble gases than for polyatomic molecular gases and noble gases are commonly used as detector gases. However, the avalanche processes leave a high number of both excited and ionized atoms. Excited noble gas atoms only return to their ground states emitting a photon. Photon energy (the minimum photon energy is 11.6 eV and corresponds to Argon) is above the ionization potential of any metal constituting the cathode (7.7 eV for copper). Therefore, photoelectrons can be extracted from the cathode producing avalanches and entering a vicious circle. Another process that can produce uncontrolled discharge is bremsstrahlung from accelerated electrons in the avalanche. In addition, positive ions are neutralized capturing an electron, typically from the cathode. Also in this process photons can be radiated resulting in undesired avalanches.

All these spurious processes are minimized by means of mixtures of noble and polyatomic gases. Polyatomic gases receive the name of quenchers. These polyatomic molecules

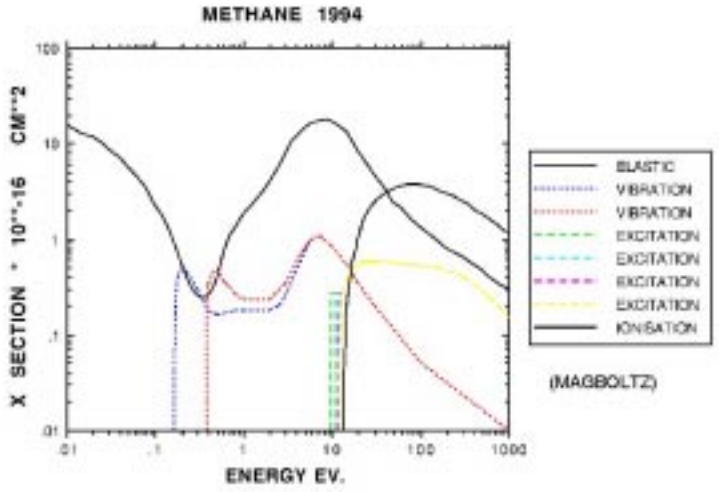

Fig. 3.7: Cross section for the different interactions photon-CH_4: elastic scattering, ionization, excitation leading to photon emission and absorption leading to vibrational state [33].

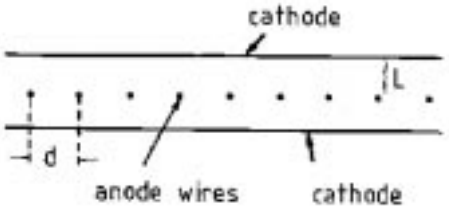

Fig. 3.8: Cross section of a multi-wire proportional chamber [41].

and absorb photons in a wide spectrum of energy, as can be evinced from the cross-sections for the different photon-CH_4 interaction processes shown in Fig. 3.7. Quenching efficiency typically increases with the number of atoms in the molecule. The most commonly used quenchers are methane (CH_4) and isobutan (c_4H_{10}). These molecules dissipate the excess of energy through elastic collisions or by dissociation into simpler radicals. For this molecules, secondary emission is very unlikely, neither when they absorb photons nor when recombine with electrons. Large photon absorption and suppression of secondary emission allows high gains before discharge. Properties of mixtures of noble gases with quenchers are extensively studied phenomenologically and published [41].

3.4 Multi Wire Proportional Chambers

A multi wire proportional chamber essentially consists of a set of thin, parallel and equally spaced anode wires, symmetrically sandwiched between two cathode planes (Fig. 3.8). Free electrons inside the chamber drift along the drift lines (Fig. 3.9) until they approach the high

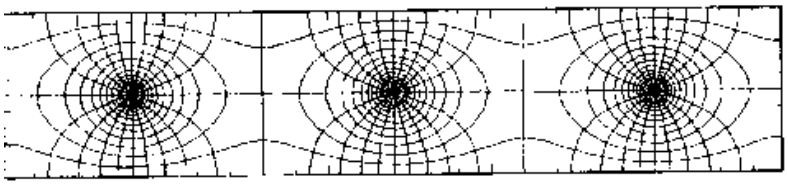

Fig. 3.9: Schematic form of the equipotential and field lines produced in a layout as that of Fig. 3.8 [41].

field region, very close to the anode wires, where they produce avalanches as explained in previous section. When avalanches occur on one sense wire a signal is induced on that wire. Signal is also induced in the neighboring wires through two mechanisms:

- directly by the charge cloud of the avalanche. The amount of signal on each wire depends on the distance to the cloud and on the detector geometry.
- from the capacitive coupling between wires. This signal is much smaller and of opposite sign from that induced directly from the cloud of charge, as realized by Charpak $et.\ al.$ and reported in [47].

Thus, the recorded signal from each wire gives an information on the position of the drifting electrons in the direction orthogonal to the wires orientation. The weighted average position of the hit wires provides an accurate information on the trajectory of the particle crossing the chamber. Position in this direction can be reconstructed with different methods [49].

3.5 Pad-type Multi Wire Proportional Chamber

A pad-type MWPC is a MWPC with 2D tracking capabilities. In these devices one of the cathode planes is composed of pads isolated one from each other, and maintained at the same potential. When avalanches occur at the wires, signals are induced on the pads of the pad plane by the same capacitive mechanism explained in the previous section for the wires. Information of the 2D position of the avalanche is extracted from the signal recorded on each pad and the known position of each pad. Accuracy of localization depends on the pads size, wire spacing, distance between pads and wires and, in general, on the detector geometry.

3.5.1 Signal induced on the pads

Using the signal induced by the ions during the whole time of their motion toward the cathodes would result in extremely long signals and thus, extremely long dead times. On top of this, the signal induced on the pads would strongly depend on factors like geometry and wire displacements through the direction of the ion motion. A typical electronic amplifier produces its signal in a short time by using only the early part of the induced signal, when the ions are still in the vicinity of the wires. A simplified example of a pad-type MWPC is that of Fig. 3.10. Two cathode planes are separated by a distance D and in between them

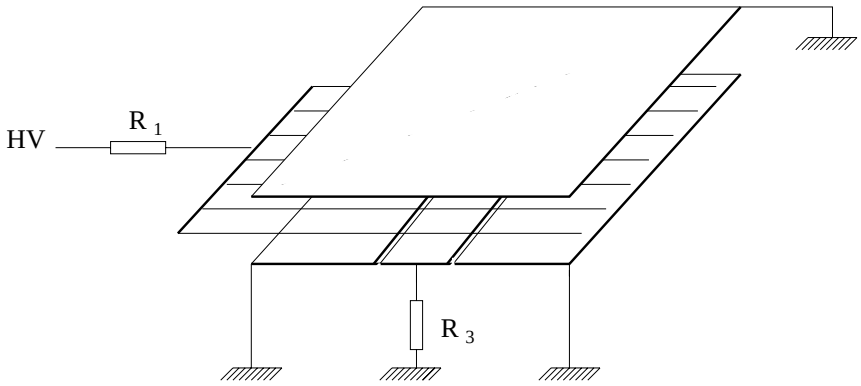

Fig. 3.10: A MWPC where a wire grid is in between two cathode planes, one of which has an isolated pad connected to ground through a resistor.

there is a grid of anode wires. One cathode plane has an isolated strip, of width W, connected to ground through a resistor. The pitch of the wires, l, is much smaller than the length of the strip. To derive an analytical expression for the charge induced on the pads let us consider a straight particle track, parallel to the planes and perpendicular to the anode wires. Since $l << W$ we can think of the charges produced by the avalanches on the wires as a line of charge density λ in between the cathode planes, parallel to them and perpendicular to the wires. The surface charge density $\sigma(x)$ induced on the cathode plane, by the "line of charge", can be calculated using the method of images:

$$\sigma(x) = \frac{-\lambda}{2D} \frac{1}{cos(\pi x/D)} \tag{3.27}$$

where x is the transverse distance to the track[1]. The pad response function (PRF) represents the total amount of induced charge on one pad as a function of the transverse distance between the pad center and the avalanche [45]. The PRF is obtained by integrating 3.27 over the area of the strip. In the particular case considered above this is:

$$P_0(x) = \int_{x-\frac{W}{2}}^{x+\frac{W}{2}} \sigma(x')dx' \tag{3.28}$$

It has been found that $P_0(x)$ is well approximated by a gaussian within a few per cent of its maximum value [48]:

$$P_0(x) \simeq e^{-\frac{x^2}{s_0^2}} \tag{3.29}$$

As an example, a gaussian fit to a typical PRF $P_0(x)$ for W=6 mm and D=8 mm gives $s_0 = 3.5$ mm [45]. In a more realistic approximation the spatial spread of the avalanches ,mainly due to the diffusion of primary electrons, has to be taken into account. Since the transverse displacement of an electron is governed by a gaussian distribution 3.2.1 with characteristic

[1] It is interesting to note that the integral of the charge density is half of the charge reaching the wires and it has opposite sign.

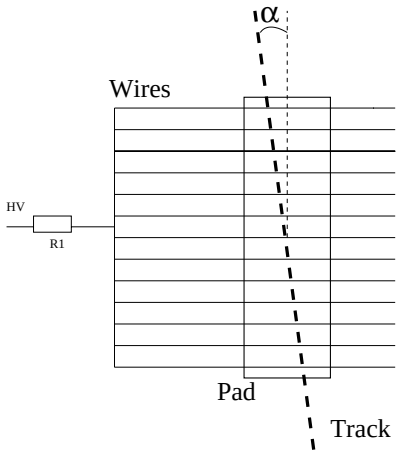

Fig. 3.11: Track parallel to the wire plane, and thus to the cathode and pad plane, and with an angle α respect to the pad.

width S_{diff} that depends on the drift length and magnetic field, its effect to the PRF could be taken into account by adding a correction to the s_0:

$$P(x) \simeq e^{-\frac{x^2}{s^2}} \tag{3.30}$$

$$s^2 = s_0^2 + s_{diff}^2(z, B) \tag{3.31}$$

In the case where the track has an small angle α with respect to the strip, Fig. 3.11, the integral in 3.28 turns into a 2D integral over the surface of the pad. In reference [45] the authors report an approximation equivalent to formula 3.30 in which they introduce an additional effective width due to the small angle α:

$$s^2 = s_0^2 + s_{diff}^2(z, B) + \frac{\alpha^2 l^2}{12} \tag{3.32}$$

Typically, the PRF for a given detector is measured using a localized source of electrons and measuring the integral charge induced on the pads as a function of the transverse distance to the source. To determine the position of an avalanche, typically, the PRF is fitted to the recorded signal of a cluster of pads.

3.6 Principles of operation of a Time Projection Chamber

A TPC basically consists of a gas volume immersed in an electric field, often complemented by a parallel magnetic field, plus a pad-type multi-wire proportional chamber (Fig. 3.12). A charged particle traversing the gas volume generates ionization and the electric (and magnetic) fields make the generated electrons drift toward the wire chamber where the arrival position of the drifting electrons is recorded. The remaining coordinate, in the direction of the drift, is determined from the measured electrons drift time. Drift time is the time difference between the time of the arrival of the electrons to the MWPC and the time of the passing of the particle, which is typically measured by some other detector (i.e. trigger detectors).

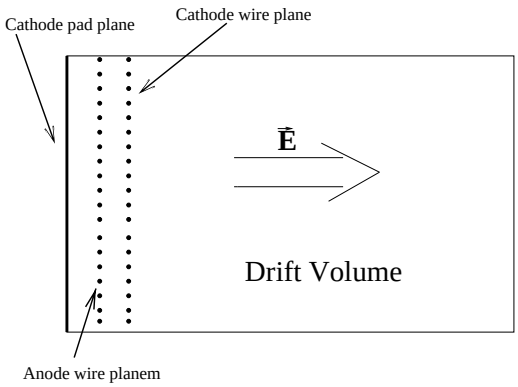

Fig. 3.12: Schematic layout of a Time Projection Chamber.

Momentum measurement can be performed by means of measuring the particle trajectory curvature due to the magnetic field. MWPCs provide a proportional response to the number of electrons that originated the signal which is related to the energy loss of the particle, which depends on its identity. Thus, the MWPC provides an energy loss determination that, together with momentum measurement, allows for independent particle identification.

3.6.1 Gating grid

In a TPC a problem emerges since not all the ions produced in the avalanches are collected by the cathode planes. The quantitative fraction depends on field intensities and geometry configuration and it can be of the order of 90%. These ions drift inside the drift volume moving toward the HV anode plane. Ions from many events can accumulate inside the drift volume, depending on the event rate and drift length, producing electric field distortions. Therefore it is necessary to prevent positive charges going from the amplification region into the drift region. This is achieved with an ion gate, which is an additional grid, usually named “gating grid”, located inside the drift volume and close to the cathode grid. The transparency of the grid to ions and electrons can be regulated through its potential. Typically, the gate “opens” when there is a trigger and stays open for the maximum electron drift time [45]. The small speed of ions with respect to electrons explains, together with the argument on drift electrons concluding the next paragraph, why ions are fully trapped in the gating grid while electrons can traverse it.

3.6.2 Drift of electrons in parallel electric and magnetic fields

The equation of the macroscopic motion of a particle under the influence of electric and magnetic fields, $\vec{E}$ and $\vec{B}$, is:

$$m\frac{d\vec{u}}{dt} = e\vec{E} + e[\vec{E} \times \vec{B}] - k\vec{u} \tag{3.33}$$

where m and e are the mass and electric charge of the particle, $\vec{u}$ is its velocity vector, and k describes a macroscopic frictional force proportional to $\vec{u}$ caused by the interaction of the

particle with the gas. The solution of Eq. 3.33 for $t >> m/k$ is a state for which $d\vec{u}/dt = 0$ and the drift velocity is determined by the equation:

$$\vec{u} = \frac{e}{m}\tau|\vec{E}|\frac{1}{1+w^2\tau^2}[\hat{E} + w\tau(\hat{E}\times\hat{B}) + w^2\tau^2(\hat{E}\cdot\hat{B})\hat{B})] \tag{3.34}$$

being w_i:

$$w = \frac{e}{m}B \tag{3.35}$$

In most TPC's as well as in the HARP TPC $\vec{B}$ is parallel to $\vec{E}$ and both orthogonal to the wire plane. This is because we want the electrons to drift in a straight line orthogonal to the wire plane in order to be able to easily reconstruct the track. Perfectly parallel $\vec{E}$ and $\vec{B}$ are impossible, mainly due to mechanical misalignments of the magnet with respect to the electric field cage and to field distortions due to materials and charging up. In the case where $\vec{E}$ and $\vec{B}$ are nearly parallel:

$$\vec{E} = (0,0,E_z) \quad , \quad \vec{B} = (B_x, B_y, B_z) \quad |B_x|, |B_y| << |B_z| \tag{3.36}$$

the B_x and B_y generate a change in the drift direction

$$\frac{u_x}{u_z} = \frac{-w\tau B_y + w^2\tau^2 B_x}{(1+w^2\tau^2)B_z} \tag{3.37}$$

$$\frac{u_y}{u_z} = \frac{w\tau B_x + w^2\tau^2 B_y}{(1+w^2\tau^2)B_z} \tag{3.38}$$

that produces a displacement of the drift electrons at a distance L:

$$\delta_x = L\frac{u_x}{u_z} = L(\alpha_x\frac{w^2\tau^2}{1+w^2\tau^2} - \alpha_y\frac{w\tau}{1+w^2\tau^2}) \tag{3.39}$$

$$\delta_y = L\frac{u_y}{u_z} = L(\alpha_x\frac{w\tau}{1+w^2\tau^2} + \alpha_y\frac{w^2\tau^2}{1+w^2\tau^2}) \tag{3.40}$$

where:

$$\alpha_x = \frac{B_x}{B_z} \qquad and \qquad \alpha_y = \frac{B_y}{B_z} \tag{3.41}$$

It is evident, from Eq. 3.37 and Eq. 3.38 that the drift electrons, for large B fields, in this configuration eventually follow the $\vec{B}$ field lines, while ions follow the $\vec{E}$ field lines due that for the same B field $w_{ions} << w_{electrons}$.

3.6.3 Momentum measurement in a TPC

A particle traversing a TPC describes a helix due to the magnetic field. The projection of the track onto the pad-plane of the TPC, perpendicular to the magnetic field, is an arc of a circle or radius:

$$R = \frac{P_T}{0.3\ q\ B}\ \frac{[GeV/c]}{T.m} \tag{3.42}$$

where P_T is the transverse component of the particle momentum w.r.t the magnetic field direction. By measuring the Sagitta of the projection of the track onto the pad plane the

transverse momentum is therefore measured. The error in the measure of P_T, when measured with N equidistant measurements of the saggita can be parametrized as [59]:

$$\frac{\sigma(P_T)}{P_T} = \sigma(x)\frac{P_T}{0.3\ B\ L^2}\sqrt{\frac{720}{N+4}} \tag{3.43}$$

where $\sigma(x)$ is the resolution of the detector and L the distance between measurements. Momentum along the $\vec{B}$ direction can be determined from the angle, θ, between the track and the magnetic field:

$$P_T = Psin\theta \tag{3.44}$$

4. THE HARP TIME PROJECTION CHAMBER

4.1 Overview

The HARP TPC has a cylindrical shape with its axis of symmetry parallel to the beam. Its main structure is formed by two coaxial cylinders of different radius confining the detector active volume. The smaller cylinder houses the target where the interactions occur (Fig. 4.1). End-plates at both ends of the volume are supported by the outer cylinder. The upstream end-plate serves as support for the inner cylinder and for the readout electronics. The TPC parallel electric and magnetic fields are oriented parallel to the beam. The electric field is provided by a system of strips attached to the inner surfaces of the cylinders and maintained at degrading potential, while the magnetic field is provided by a solenoid surrounding the TPC. The gas mixture used is a well known and documented mixture, Argon-methane (91%-9%), already used by the ALEPH and DELPHI experiments at CERN . The upstream end of the TPC is instrumented with a wire chamber, parallel to the end-plate, formed by a readout pad-plane, a plane of sense wires, a plane of cathode wires and a plane of gate wires. The total width of the wire chamber is only 21 mm and covers 97% of the TPC active volume. The pads of the pad-plane are physically printed on the same Printed Circuit Board (PCB) hosting the analog front-end electronics. Analog signals induced on the pads are digitized by a fast 10 bit Analog to Digital converter (ADC) and recorded by a Data Acquisition System.

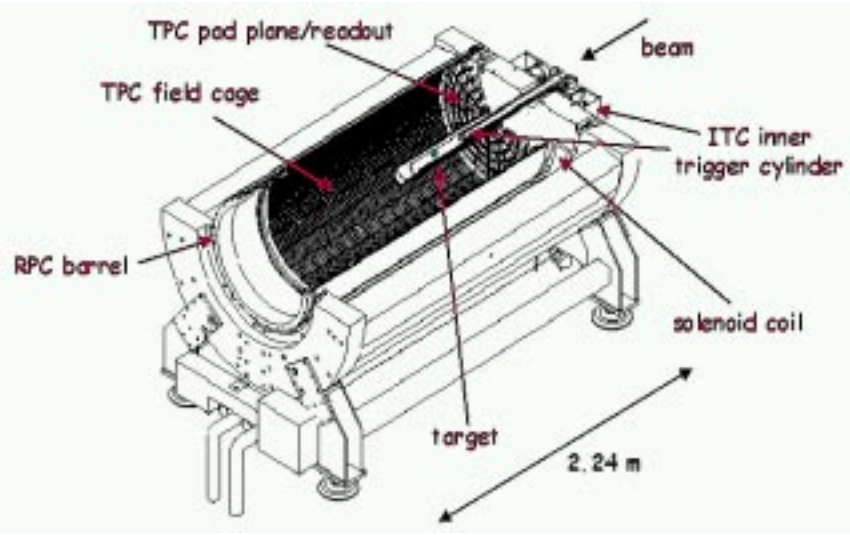

Fig. 4.1: (alias Fig. 2.3) Longitudinal section of the solenoid, TPC and target support.

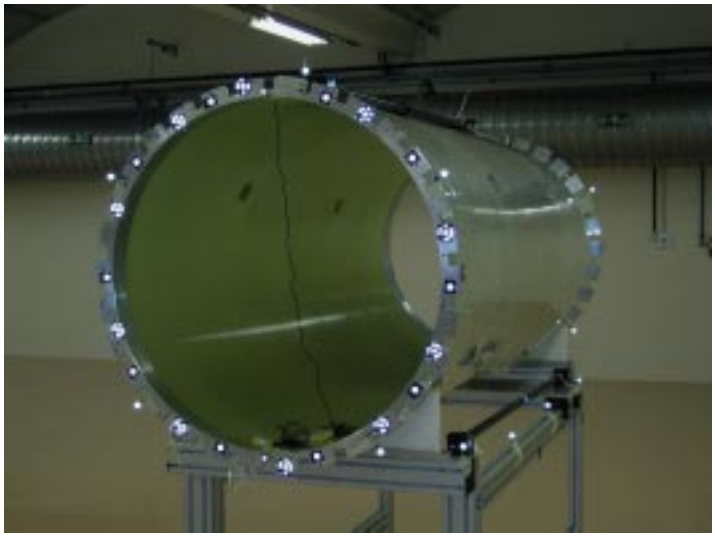

Fig. 4.2: The outer barrel before assembling of all the other parts.

4.2 Mechanical structure

4.2.1 The outer barrel

The outer barrel is a Stesalit cylinder of 800 mm of inner diameter, 820 mm of outer diameter and 2010 mm length. The outer barrel is the main TPC structure. The outer field cage is directly mounted on its inner surface. Two aluminum flanges are glued by Araldit at both ends of the cylinder (Fig. 4.2) in order to support the "cork" end-cap and the pad plane structure. The materials used in the TPC construction are mainly Stesalit, aluminum and mylar [1] and have been chosen according to their properties. Stesalit [2] is well known for its low degassing properties, high electric field rigidity, mechanical strength. it is also relatively easy to machine and has a low radiation length ($X_0 \sim 19.4$ cm). An aluminum alloy has been chosen because it is amagnetic, easy to machine and has a low radiation length ($X_0 = 8.9$ cm). Mylar has been used for its excellent mechanical properties, especially its low deformation with temperature, high electric field rigidity (10^{18} MΩ/cm) and especially because it is easy to metallize.

4.2.2 The downstream end-cap

The downstream end of the TPC volume is closed by an aluminized Mylar membrane held at high voltage. This membrane is glued on an aluminum flange, which at its turn is held in place by a floating mechanical support on the end-cap, also called "cork". The cork end-cap is a Stesalit and aluminum structure with cylindrical symmetry. Apart from the high voltage membrane, the cork also supports a honey-comb plate, downstream of the HV membrane, that delimits the gas volume (Fig 4.3). In this way, deformations of the HV Mylar membrane due to different pressures are avoided. The honeycomb is also aluminized and held

[1] Mylar is one of the trade names of ethylene polytereohtalate
[2] Stesalit is a particular fiberglass composite material

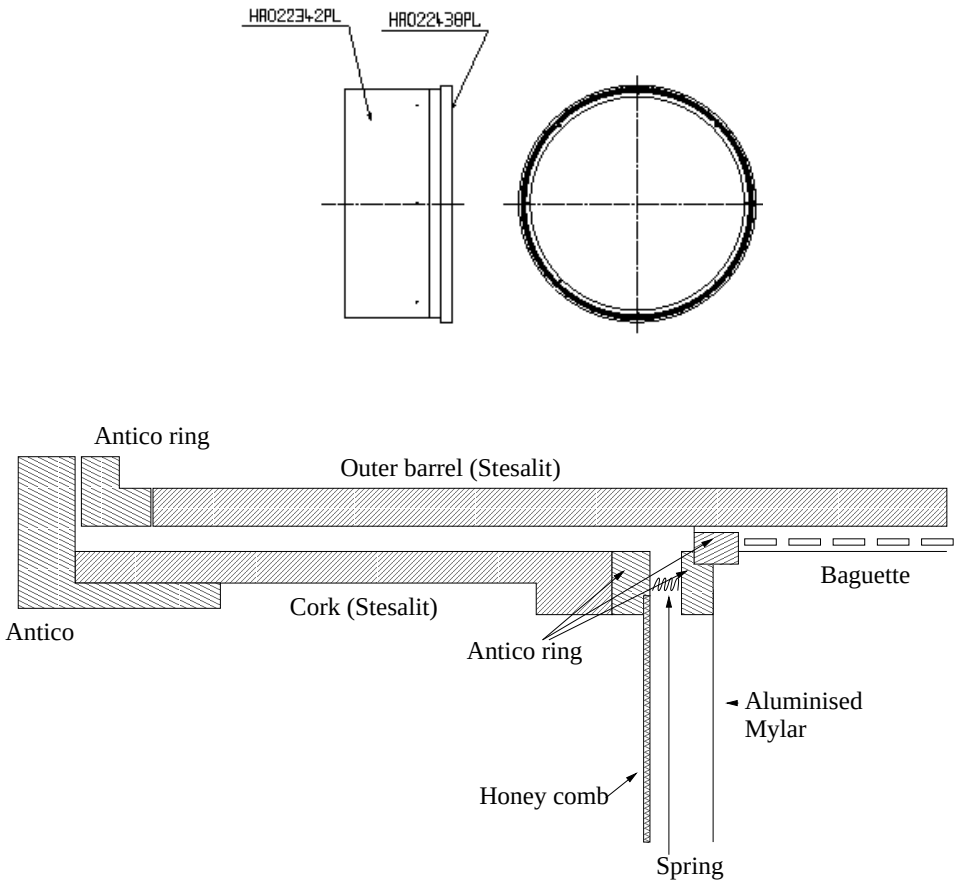

Fig. 4.3: The cork end-cap. Side view (top left), top view (top right) and cross section once assembled to the outer barrel (below).

at the same voltage as the membrane in order to avoid electrostatic forces on the membrane, these could heavily deform its shape introducing distortions of the electric field. At its turn, the honeycomb structure holds in place the optical fibers of the laser calibration system described in Chapter 5. The distance between the honeycomb and the end of the cork, which is held at ground potential, is 352 mm. This is necessary to avoid the formation of dangerous breakdown being the honeycomb at ~ 20 kV.

4.2.3 The pad plane support

The upstream end of the TPC is closed by the pad plane. This is mounted on an aluminum structure consisting of six concentric rings 16 mm thick, 25 mm wide kept together by six spokes of the same dimensions. Complementing the spokes, there are spoke segments between rings (Fig. 4.4). The support structure has been designed to keep the pad plane motherboard flat by gluing it at this the support with epoxy to achieve a planarity better than 100 μm. The space between the rings allows the analog electronics cabling to reach the pad plane. The inner support ring holds in place the inner barrel.

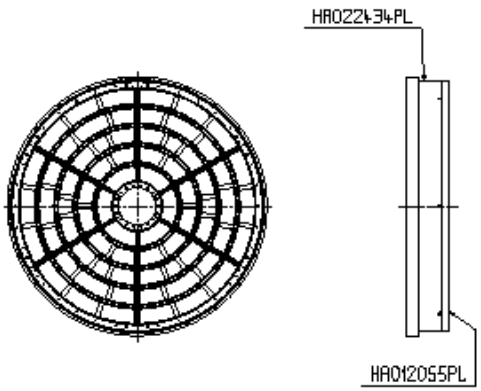

Fig. 4.4: Pad plane support, top view (left) and side view (right).

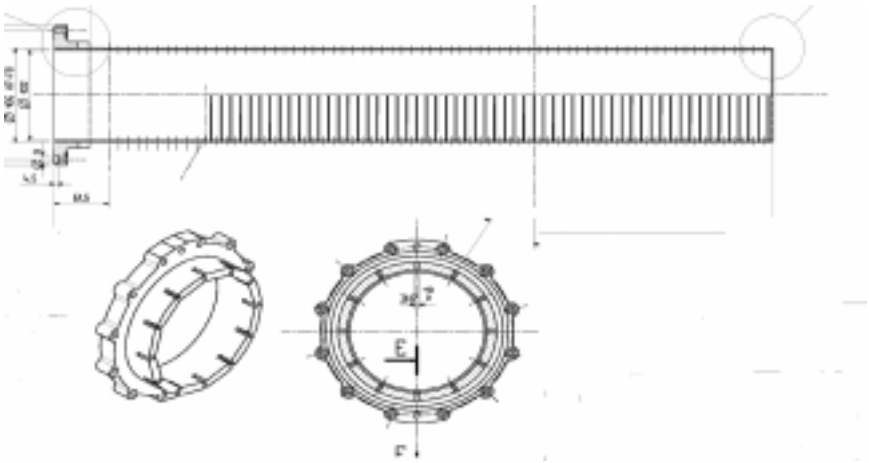

Fig. 4.5: Scheme of the inner barrel.

4.2.4 The inner barrel

The inner barrel consists of a Stesalit cylinder of 51 mm inner radius, 798.5 mm length and 2 mm thick. Its upstream end has an aluminum flange, 27.5 mm thick, that allows its fixation on the pad plane support. Its downstream end is closed by a 25 μm thick aluminized Mylar membrane (Fig 4.5). The inner barrel houses the target and the Inner Trigger Cylinder and supports the inner field cage described later.

4.2.5 The wire chamber

At the upstream end of the TPC, three planes of wires complement the pad plane to form the HARP TPC chamber. These are the sense wires, the cathode wires and the gate wires, extending from 5 mm up to 15 mm downstream of the pad-plane respectively. Each plane of wires is mounted on an insulating Stesalit structure which basic geometry is that of two

Plane	Thickness	Pitch	Distance to pad plane	Potential	Material
Sense wires	$20\mu m$	4 mm	5 mm	1830 V	W / Au
Cathode wires	$80\mu m$	2 mm	10 mm	0 V	Cu / Be
Gate wires	$80\mu m$	2 mm	16 mm	Nominal / $\pm$35 V	Cu / Be

Tab. 4.1: Wires characteristics.

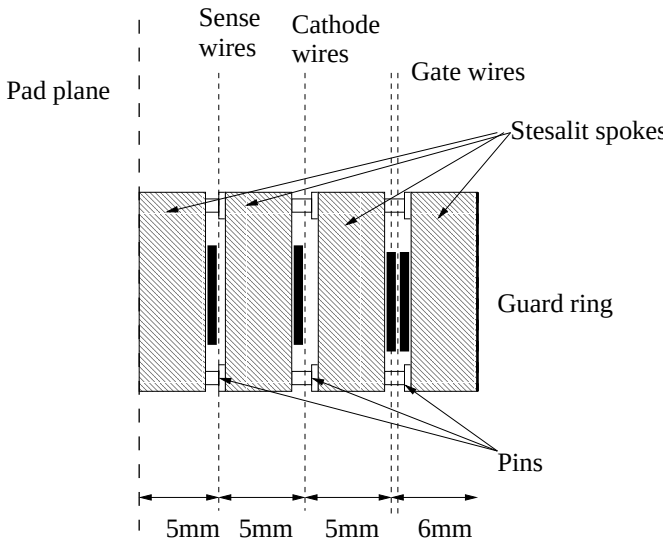

Fig. 4.6: Schematic wire and pad plane structure.

concentric circles of different radius interconnected by six spokes, dividing each structure in six sectors (Fig. 4.6). Each structure occupies only 5 mm in the z direction and is therefore a flexible support. However it has been computed to be strong enough to support the wires tension by finite elements method simulation [50]. The spokes hold the wires as in an hexagonal "spider's web". The properties of the wires of each plane are described in Tab. 4.1. The wires are strung around pins precisely located on the spokes (Fig. 4.7). The sense and cathode wire planes are formed of a single wire strung in an hexagonal spiral from start to end. The wire makes one symmetric hexagon and then increases the radius inside the spoke up to the largest hexagon inscribed in the TPC. The remaining parts of the circle are covered by six shorter wires in every plane strung in different sectors (Fig. 4.7). This is possible since none of the wires is read out. For the gate wires plane there are two different wires strung in two different supports which are faced (Fig 4.6). The pitch of the wires in each support is 4 mm. The wires of one support are shifted by 2 mm with respect to the other support to achieve a pitch of 2 mm. The wires from one plane are shifted 100 μm in the z direction for gating performance reasons as will be explained in Section 4.3.4.

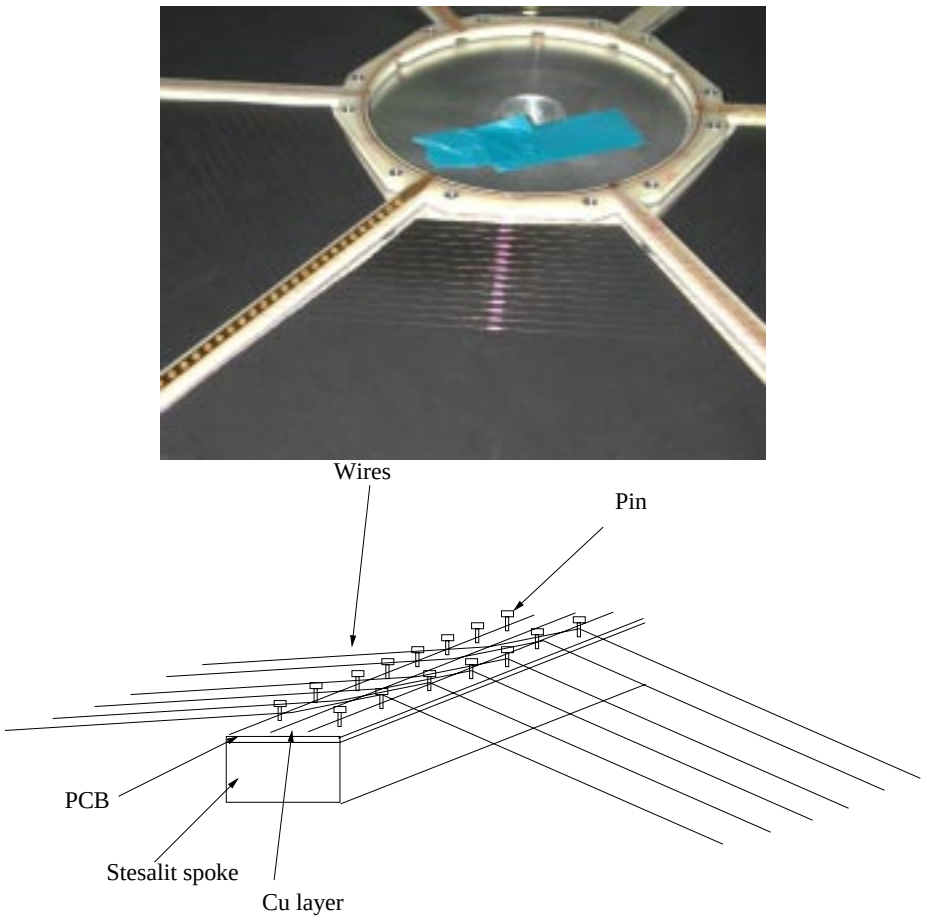

Fig. 4.7: Picture of a gate wire plane (top). Detail of the spoke where the wires increases the "radius" of the hexagon.

4.3 Electrostatic configuration

The electric field in the drift volume of the TPC is of 115.1 V/cm, over a maximum drift length of 154 cm. This field is provided by the anode HV plane at the downstream end of the active volume, the grounded pad plane at the upstream end of the active, and the inner and outer field cages that define the field along the whole drift length.

4.3.1 The anode high voltage plane

The anode plane consists of a mylar membrane (25 μm thick) aluminized with an aluminum thickness of 250-350 Å on both sides. The membrane is 800 mm in diameter and it is glued with Araldit on an Antico ring of 750 mm inner diameter and 800 mm outer diameter. It is kept at 17100 V.

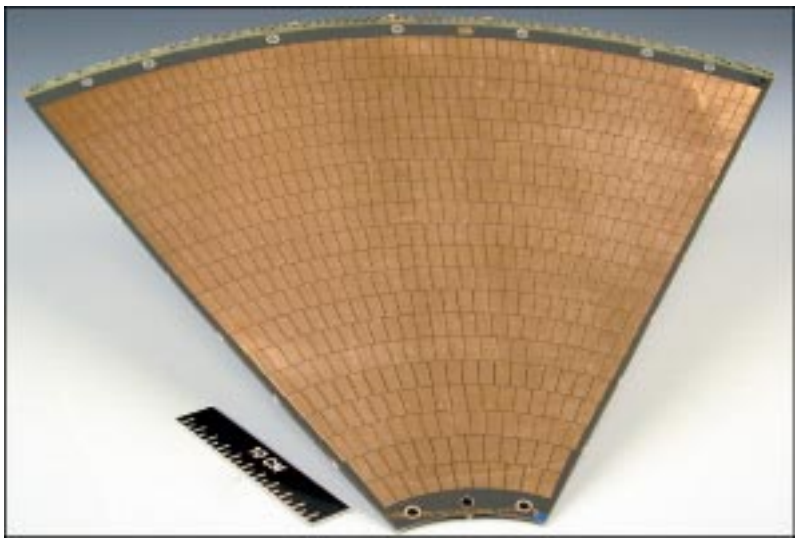

Fig. 4.8: One sector of the pad plane

4.3.2 The pad plane

The pad plane is a six-layer printed circuit board containing the readout pads and part of the analog electronics, specifically the pre-amplifiers. The readout pads are directly printed on the outer layer. The pad plane is divided into six boards, called sectors, following the symmetry of the pad plane support which is divided in six sectors by the spokes. The pads are gold plated and 35 μm thick, and are printed on the mother-board by standard photolitographic techniques. Each pad is approximately 15.0 mm length and 6.5 mm width, slightly varying according to their position in the sector. Each sector is covered by 662 pads, ϕ distributed over 20 rows as shown in Fig. 4.8. It is visible that the pads eventually cover the full active volume not covered by the spokes.

4.3.3 The multi-layer field cages

To correctly define the field along all the drift volume, a structure of electrodes, each kept at a precise degrading potential, is attached to the Stesalit barrels, surrounding the gas volume. For the outer field cage three layers of electrodes are necessary in order to correctly define the electric field and avoid distortions and “field ejection” [3]. Facing the drift volume there is a layer of 10 mm aluminized mylar strips, separated by 1 mm gaps. These are positioned onto Stesalit support bars, known as ”baguettes”, which are glued with Araldit onto the Stesalit barrel and parallel to the axis of symmetry (Fig. 4.9). There are 24 baguettes glued onto the inner surface of the outer barrel. A strip passes through the hole of each baguette and is tensioned. Attached to the surface of the Stesalit cylinder there is a kapton foil with printed copper strips 10 mm wide and 1 mm gap separation, on both sides. Strips at each

[3] Field ejection is the phenomenon of large fringe fields in the proximity of conductors. If the fridge field occurs in the gas, it can originate ionization and consequent charging up or, worst, sparks. In our case, field ejection could be caused by the high potential difference between the two sides of the Stesalit barrel, where the outer part is grounded while the inner one has the mylar strips potential [43]

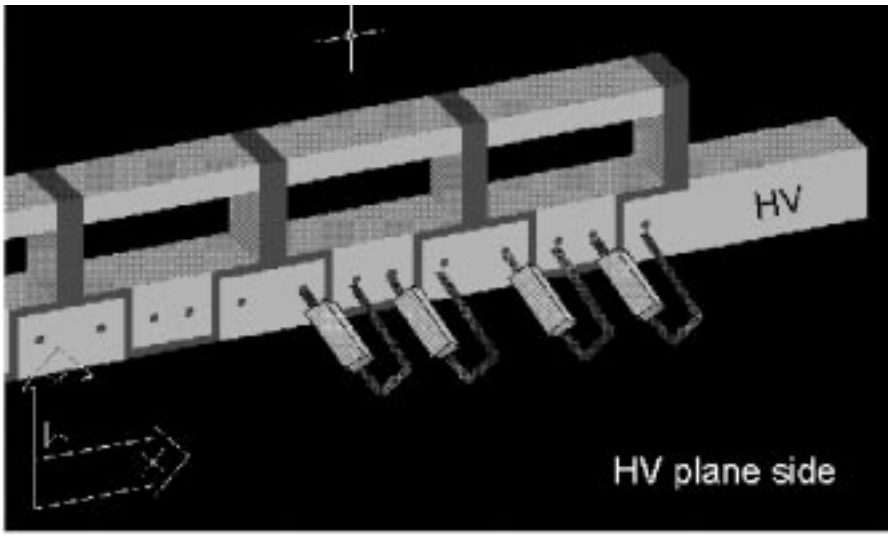

Fig. 4.9: A scheme of a baguette with the conductive printed circuit and the resistors mounted.

side are shifted by half a period and are connected as shown in Fig. 4.10 together with the potential steps. A system of resistors sets the potential of each strip (voltage divider). High precision resistors (10^{-4} accuracy), obtained by metallic technology, are mounted onto the baguettes and are in contact with their respective strips through three-dimensional circuits printed directly onto the baguettes (Fig. 4.9). Very schematically, the layer closest to the drift volume defines the axial electric field. The middle one avoids field distortions close to the cylinder walls. The third one avoids field ejection.

For the inner field cage, the layer further from the drift volume is not present. To prevent the field ejection problem, five different strips at increasing potential are etched on the inner surface of the inner barrel and covered by a thin layer of conformal coating. This different strategy was motivated by keeping a low amount of insulator to prevent gas discharges inside the field cage.

4.3.4 The chamber wires

The sense wires are kept at 1830 V while the cathode wires are kept at ground and the gate wires are at -67 V, according to their position in the drift volume, during readout and alternated at -67+35 V and -67-35 V when no readout is in progress. These potentials are provided to the wires by means of a copper strip printed on a printed PCB which is glued on the spokes. The pins force the wires to be in contact with the copper. For the two different spoke-structures of the gate wires, only three of the spokes have the copper foil. The three spokes having copper are chosen in such a way that contiguous planes have the copper foils in different spokes (Fig. 4.7). This is to avoid having two copper conductors at different potential near in space and with gas between them. Facing the drift space, the last support structure is covered by a thin copper guard ring maintained at the potential that corresponds to the field cage strips at the same longitudinal position. This is to prevent the spokes from polarizing and distorting the field nearby [43].

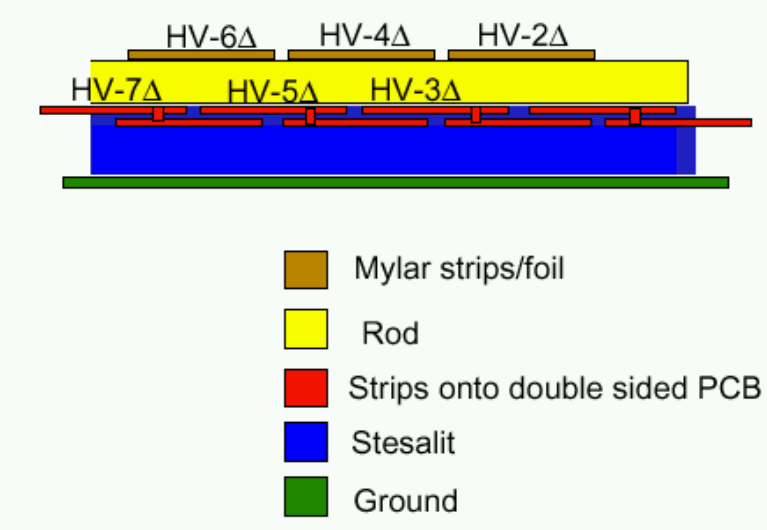

Fig. 4.10: The TPC outer field cage cross-section scheme.

For the gate wires, alternated wires are located at slightly different distances from the pad plane. The motivations for this are twofold:

- to avoid a complicated distribution schemes for delivery of the correct potential to the wires. If both planes of wires were at the same nominal distance from the pad plane, each plane of wires would touch the spokes that provide the voltage to the other plane.
- having two layers of gate wires results in a better performance of the gate [34].

4.4 Gas mixture

For the HARP TPC a well known and documented gas mixture was chosen: argon-methane at 91%-9%. For the harp nominal electric and magnetic fields the electrons drift velocity is 5.17 cm / μs and the transverse and longitudinal diffusion are 378 and 208 μm per cm of drift respectively, as reported in Figs. 4.13 and 4.12. The most probable number of electrons generated per cm of track for an ionizing pion is shown in Fig. 4.11, according to simulations [33].

The gas mixture is provided by a pre-mixed system that allows for continuous gas quality monitoring (Fig. 4.14) before and after it has gone in the TPC volume.

4.5 Read-out analog electronics

The signal induced on the readout pads described above is amplified by a preamplifier and a shaper and fed into an analog to digital converter, hereafter referred to as ADC. The shaping and amplification is performed by an ALCATEL SMB302 circuit which is an integrated four channel preamplifier / shaper that we have put in a TSSOP 24 package (Fig. 4.15). Each channel of the SMB302 consists of a single preamplifier and shaper block. The preamplifier

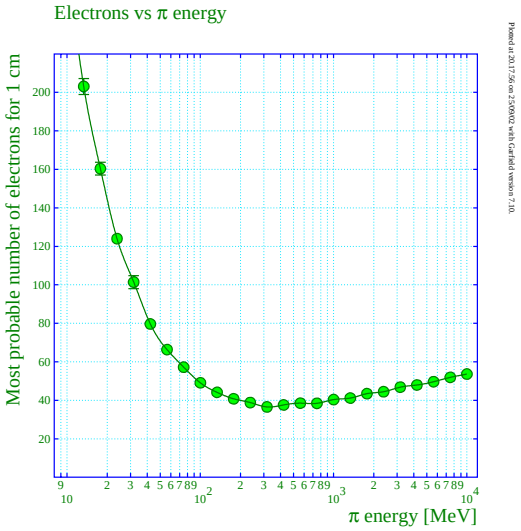

Fig. 4.11: Most probable number of electrons generated per cm of track for an ionizing π as a function of its energy.

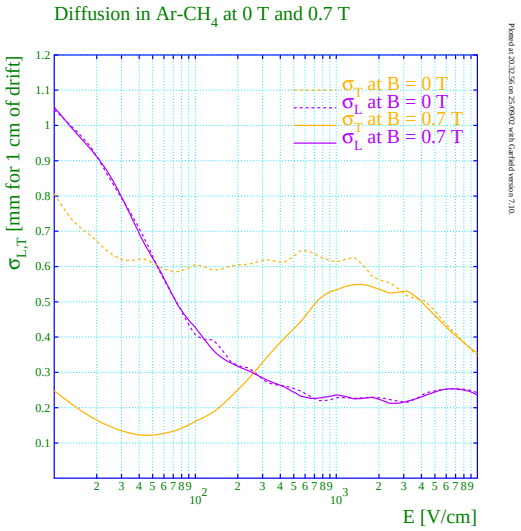

Fig. 4.12: Transverse and longitudinal electron diffusion per cm of drift as a function of the electric field for magnetic field values of 0.0 and 0.7T.

is a low input impedance current sensitive type amplifier allowing for fast response. Fast amplification and shaping is required in order to cancel the long tails of the ion signals. Each chip has two separate power supplies: a positive one, with a nominal value of +3.0 V and a negative one with a nominal value of -2.5 V. The circuit acts as an inverting amplifier, optimized for negative output pulse. The TSSOP 24 packages are mounted on the outer layer of the pad plane PCB and the pre-amplifiers of one chip share common voltage supplies.

Six layers of printed circuit are needed to drive the signals from the pads to the pre-

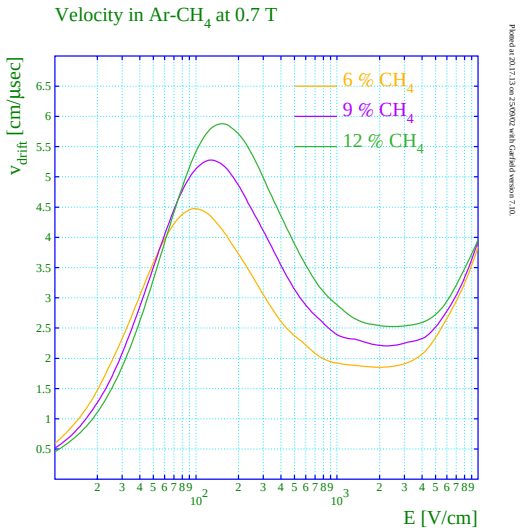

Fig. 4.13: Electron drift velocity as a function of the electric field for three different mixtures of Ar/CH_4.

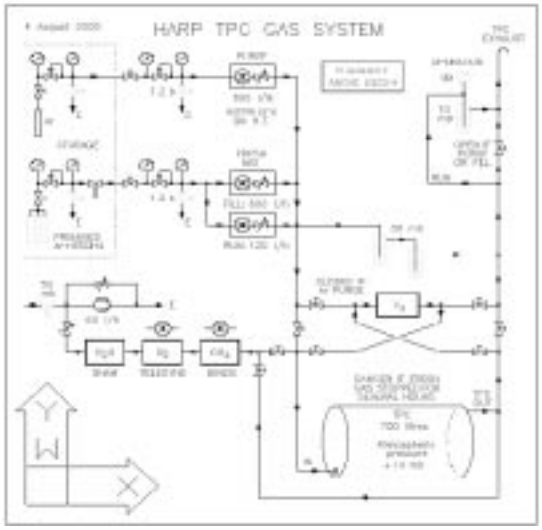

Fig. 4.14: A schematic layout of the HARP TPC gas system.

amplifiers and from these to the micro-flex cables used to drive the signals to an external buffer card. (Fig 4.15). Each micro-flex has a capacity of 24 channels plus low voltage supplies and ground for the amplifier circuits. A small number of chips ($< 5\%$) have two different voltage supplies from two different flexes, otherwise all micro-flex groups are electrically separated from the others.

The analog signal is transmitted from the buffer cards to the ADC by means of coaxial cables, called pico-coax, which are shielded conductors with an overall outer diameter of 500 μm.

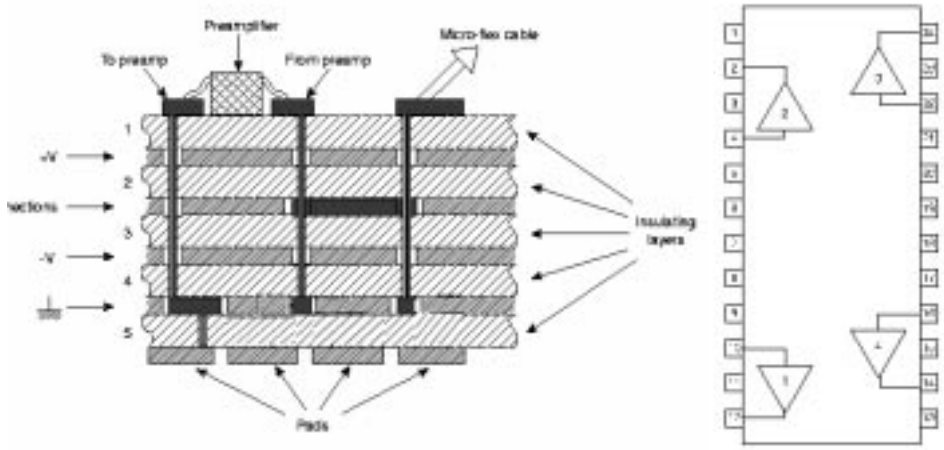

Fig. 4.15: Left: cross section of the pad plane. Right: schematic layout of a package containing four pre-amplifiers.

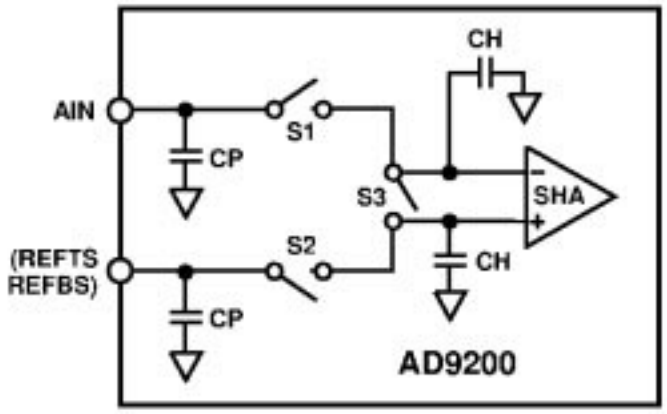

Fig. 4.16: Schematic layout of equivalent circuit of the AD9200 analog to digital converter.

4.6 Digital electronics

The analog signal is digitized with a 10 MHz 10 bit Analog to Digital Converter ANALOG DEVICES AD9200. The AD9200 uses a multistage differential pipeline architecture at a maximum data rate of 20 million samples per second [4], it has an on-chip sample and hold amplifier and voltage reference. The equivalent analog input structure of the sample and hold amplifier is that of Fig. 4.16. The analog input signal is connected to AIN. Switches S1, S2 and S3 open and close according to a clock signal. When the clock signal is low, S1 and S2 close and S3 opens. During this time the capacitor CH is charged by the input signal. When the clock signal is high, S1 and S2 open and S3 closes forcing the output of the operational amplifier to equal the voltage stored on CH. During the time that the clock signal is high,

[4] The AD9200 ADC can perform at 20MHz but in the HARP experiment they are used at 10MHz.

the value of the voltage stored in CH is digitized. The S1 switch has a resistance of 50Ω and the combined capacitance of the pin capacitance and the hold capacitance is typically less than 5 pF. In addition, in the HARP experiment, the input analog signal reaches the AD9200 through a resistance of 20 Ω. The ADC boards used in the HARP experiment allow to digitize the data above threshold, perform pedestal subtraction and compress the data in a coded format that allows to reconstruct easily the recorded signals [51]. An ADC pedestal is set for each pad at the average amplitude of noise. It is computed from the raw noise signals during three empty events at the beginning of each run, stored internally within each ADC and automatically subtracted from signals arriving to the ADC. On top of this, a threshold of 10 ADC counts is set to trigger the data recording. In addition to the signals above threshold a pre- and post-sampling of 3 samples is stored in the data. Negative signals are set to zero and suppressed.

4.7 Data Acquisition

The HARP Data Acquisition System is based on DATE [52]. The data flow architecture is organized along parallel data streams. The six TPC sectors data plus a master crate collecting general event information, e.g. timings, are read in parallel. An "event builder" builds an event from all data and stores it in a data base. The master crate is responsible for recording the synchronism between the trigger, the ADC clocks and the laser shot which are necessary in the analysis steps of next chapters. There is a time jitter [5] of 100 ns between the ADC clocks and the reference trigger signal.

4.8 The voltage supply system

High voltage for the anode plane and the outer field cages is supplied by a FUG HCN 140-35000 unit, capable of supplying 35kV and a maximum current of 4 mA. High voltage to the inner field cage is provided by a FUG-HCN 35-25000 unit capable of supplying 20 kV and at a maximum current of 2.5 mA. Low voltage for the analog electronics is provided by a three PL6021 power supply, distribution and current limiting units.

4.9 The cooling system

Between the solenoid and the RPC barrel there is a heat screen through which cooled water circulates, shielding the RPC and TPC from the heat generated by the solenoid. Between the solenoid end-cap and the pad plane support, there are three concentric rings of inox tubes, at three different radius, with a hole every 20 mm. The tubes are connected among them and cooled air is blown into the piping. The air flow escaping from the tubes constitutes an effective heat screen between the buffer cards (our major source of heat in the TPC) and the TPC pad plane.

[5] We define jitter as the length of a time difference distribution which is flat.

5. THE LASER CALIBRATION SYSTEM

5.1 Photo-electron point-like source for calibration purposes

In a TPC with parallel electric and magnetic fields, the effect of a small angle misalignment between the electric and magnetic field results in a displacement of every track element proportional to the drift length of the electrons. This is the so-called $\vec{E} \times \vec{B}$ effect (Sec. 3.6.2). From existing experience, for example ALEPH [60] and DELPHI [61], it is known that detector distortions have to be monitored. These can be evaluated by looking where drifting electrons from a known origin are reconstructed. Elsewhere [60] [61], this has been done using laser beams producing direct gas ionization inside the TPC volume [45]. However, such an optical system is typically delicate, expensive and complicate to build. In HARP, a novel calibration system, based on point-like photo-electron sources located at precise positions inside the detector volume, has been proposed, tested and constructed. The system consists of 198 quartz fibers held in place on the high voltage membrane. The fibers are coated with 80 Å of aluminum. UV light pulses, produced by a laser, generate photoelectrons on the aluminum photo-cathode. These photoelectrons drift inside the detector and produce the calibration signals. The technique allows to measure distortions, drift time, ion feedback and time stability in real time. Since the photoelectrons are all produced at the downstream end of the detector volume, only integrated corrections can be determined. However, this information can be used to qualify distortions generated by the B field dis-homogeneity (cylindrical symmetry) or by the wire chamber structure, in particular, spoke effects, Fig 5.1.

5.2 The Photoelectric effect

The photoelectric interaction is the most probable interaction of photons with matter at energies similar to those of the atomic K shells. For photon energies above the K-shell, assuming that only K electrons are involved and that the photon energy is non relativistic, the photoelectric cross-section can be approximated to [53]:

$$\sigma = 4\alpha^4 \sqrt{2} Z^5 \phi_0 (\frac{m_e c^2}{h\nu})^{7/2} \tag{5.1}$$

where: $\phi_0 = 8\pi R_e^2/3$, α is the fine structure constant ($\alpha = 1/137$), Z is the atomic number of the medium and $h\nu$ is the photon energy. The main features of Eq. 5.1 are the decrease with photon energy as $(h\nu)^{-7/2}$ and the dependence with the atomic number as Z^5. This principle is here used to have the calibration fibers act as a source of electrons in the TPC when excited by a light from the outside.

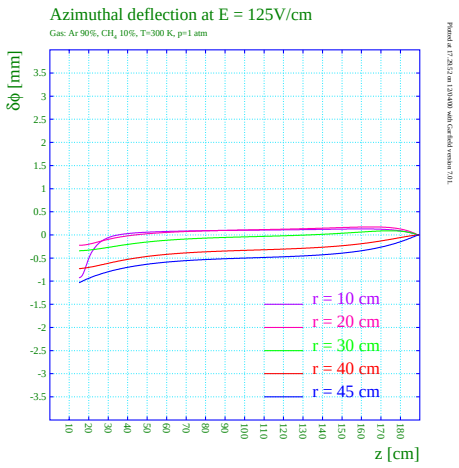

Fig. 5.1: Azimuthal deflection. The regions close to the spokes and to the field-cages are those were field distortions are expected to be more severe, according to MC simulation, [34].

5.3 Tests performed on a TPC Prototype

In order to test the working principles of this novel technique, a series of tests were carried out on a TPC prototype. Specifically, the aim of these tests were:

- check that the generated photo-electrons can escape the fiber tip
- optimize the aluminum thickness on the fiber tip
- determine the optimum UV light wavelength
- determine the energy of the light pulse necessary to generate a detectable signal in the gas detector
- determine the optimal fiber radius
- study the possible causes of instability in the electron emission (charging up)

5.3.1 Prototype Design

Fig. 5.2 shows a schematic layout of the prototype. It consists of a rectangular drift volume $30\times50\times10$ mm^3 closed by a HV aluminized mylar membrane at one end and a wire chamber at the other. The electric field in the drift volume is generated by a field cage consisting on 32 parallel conductive strips surrounding the volume and maintained at precise potentials through a voltage degrader. The strips are 1.5 mm wide and the pitch between them is of 2 mm. The strips are connected to a resistor chain (10 MΩ between strips) and a high voltage supply. Since they surround the drift volume, the strips are rectangles 30×10 mm^2 whose longer segments are directly printed on two PCBs (Fig. 5.2). For the tests described in the following sections, the field-cage was set to provide an electric field of E=150 V/cm. A Teflon structure above the HV membrane and fixed on the field cage PCBs allows the insertion of

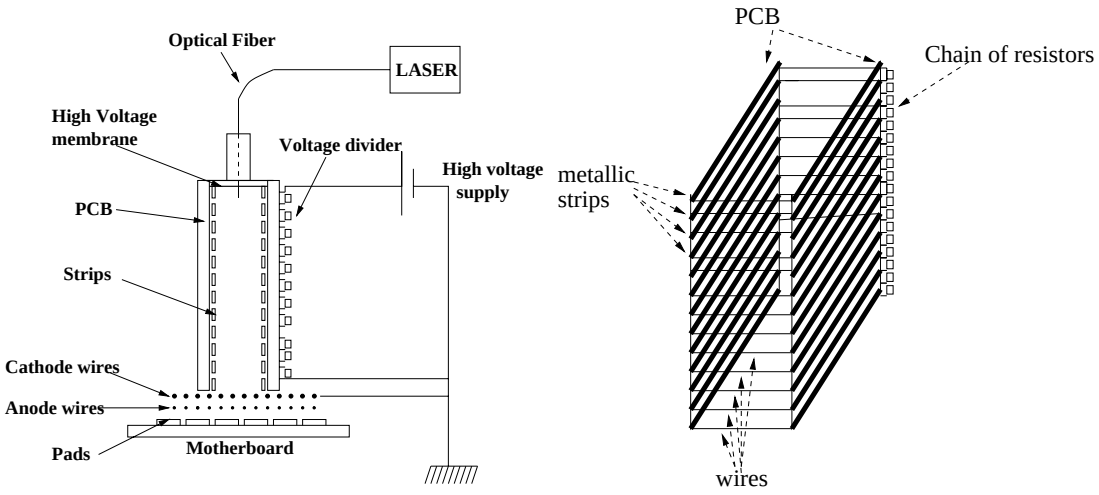

Fig. 5.2: Scheme of the TPCino.

an optical fiber inside the drift volume through a 3 mm diameter hole on the HV membrane. We had the possibility to put in electrical contact the fiber tip and the HV membrane to verify charging up. The other end of the fibers is connected to a Ultraviolet laser light source. The wire chamber consists of a plane of cathode wires, a plane of anode wires and a cathode readout pad plane. The wires are of the same material and have the same spacing than those of the real chamber. The readout pad plane consists of a rectangular six layer motherboard with 48 pads printed on the layer facing the detector volume. The pads are 6×15.5 mm^2 and are distributed over eight rows containing six pads each. The motherboard is equipped with an ALCATEL SMB302 preamplifier / shaper (Sec. 4.5) per channel. The field-cage structure can be accurately moved over the chamber in order to perform measurements like the PRF.

5.3.2 Fiber aluminisation

The tip and the lateral surface, up to 1 cm from the end, of different optical quartz fibers of 100 and 200 μm diameter were aluminized by evaporation techniques with three different aluminum thickness: 40, 80 and 120 Å. The attachment of the aluminum onto the quartz fibers was tested by rubbing an aluminized test fiber onto Teflon and aluminum and evaluating the scratches with a microscope. Teflon and aluminum are in fact the two materials with which an aluminum fiber will most probably have contact during its mounting on the setup. The coating resisted quite well to soft contacts, however, the experiment hinted that the handling of the fibers once aluminized had to be done carefully because of the limited adhesion of the metal onto the quartz and onto the polymeric cladding.

5.3.3 Laser apparatus

The laser used for the tests is a pulsed nitrogen laser (MNL 200 [64]) followed by a tunable dye laser (UDL 100 [64]) and a frequency doubler (UV1 [64]). The nitrogen laser emits a monochromatic 700 ps pulse of 337.1 nm wavelength that serves to excite the dye laser. The dye output laser light wavelength can be changed by means of the solution used and then

Pulse duration	$<$700 μs
Stability	$\pm$3%
beam dimensions	2 mm^2
beam divergence	2$\times$3 mrad
monochromaticity	0.1 nm
maximum rate	20 Hz

DYE solution	Rhodamine 6G	Coumarine 307
Wavelength	Peak / Range (nm)	Peak / Range (nm)
before f.d.	581 / 573-618	504 / 478-547
after f.d.	290.5 / 286.5-309	252 / 239-273.5

Tab. 5.1: Laser apparatus performances.

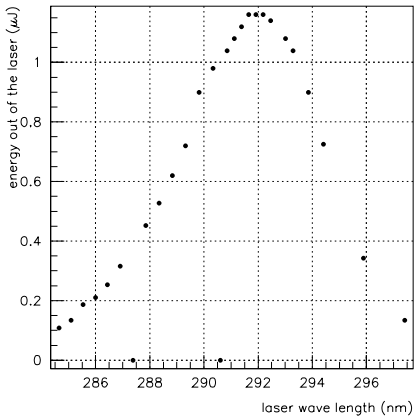

Fig. 5.3: Laser energy output as a function of the wavelength as measured with a pyro-electrical energy measurement device (LTB PEM 100 [64]).

fine tuned by means of a diffraction grating. We used a “Rhodamine B” dye solution [64], which highest emission takes place at 504 nm and can be tuned from 599 to 650 nm, as shown in Fig. 5.3 after the frequency doubler. The main specifications of the laser beam are reported in Tab. 5.1 as well as the main features of the two dye solutions used. After the frequency doubler, a customized fiber-optic connector feeds an optical fiber with the laser light. We have complemented the MNL 200 laser with a trigger system that generates a NIM signal when the laser pulses occur and with a pyro-electrical energy measurement device that allows for beam energy measurement before and after the optical fiber. A beam energy decrease has been reported as the laser shot rate is increased: a lowering of 20% is observed for the maximum rate of 20 Hz with respect to the minimum rate of 1 Hz. This decrease was not understood and not expected by the laser supplier. For this reason, all the measurements have been done at a constant rate of 5 Hz.

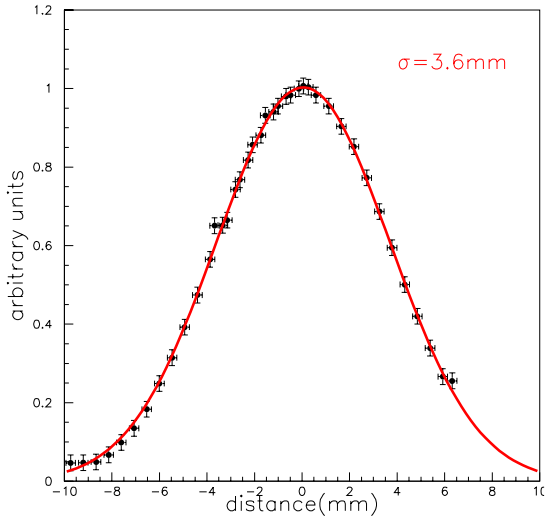

Fig. 5.4: Pad Response Function as measured in the TPCino prototype (dots). The curve corresponds to a Gaussian fit resulting in a σ=3.6 mm, which is in agreement with the theoretical one, Sec 3.5.1

5.3.4 Fiber cutting

In order to directly compare the signal generated by different fibers coated with different aluminum thickness, the difference in light yields due to different geometry of the fibers tip must be taken into account. Despite the attempts, commercial devices used in telecommunications for fiber cutting have not given the expected result. We believe this is due to the presence of a polymeric cladding around the fibers that does not allow diamonds to etch the larger fiber core through the cladding. The fibers were cut by means of a superficial cut followed by a mechanical bending until the breaking of the fibers. The light output of a fiber was measured after twenty consecutive cuts and the maximum spread of these measurements (15%) is considered as the systematic uncertainty on the fibre light output.

5.3.5 Results

A clear signal is generated by the 80 Å aluminum coated fiber correlated with the 293 wavelength laser pulses. The delay between the laser trigger and the signal occurrence depends on the chamber electric field as expected for drifting electrons. This signal has been used to measure the Pad Response Function (PRF) by measuring the amplitude of the signal generated on one pad as the transverse position of the field cage, and optical fiber, is shifted with respect to the pad plane in steps of 0.5 mm. The obtained PRF, reported in Fig. 5.4, is well fitted by a Gaussian giving a σ of 3.6 mm. The amplitude of the signals generated by the fibers with different aluminum coating have been measured and are reported in Tab 5.2. By changing the Rhodamine DYE solution by the Coumarine one, the signal yields at 248 nm wavelength have been analyzed. It has been measured that the signal yield at 248 nm is a factor 0.51$\pm$0.08 smaller than the one at 293. This is in accordance with the approximation of formula 5.1 and the photon flux measured with the pyrometer (0.46). We have verified that

Al thickness (Å)	Amplitude (arbitrary units)
40	0
80	1.0±0.15
120	0.75±0.11

Tab. 5.2: Signal generated with different fiber tips aluminum thickness.

λ (nm)	248
Max. pulse energy (mJ)	22
Max. Repetition Rate (Hz)	200
Average power (W)	4
Pulse duration (FWHM) (ns)	8
Pulse-to-Pulse stability %	¡5%

Tab. 5.3: LambdaPhysik excimer laser characteristics.

the output signal has a linear dependence with the laser intensity. From this measurement it has been extrapolated that in order to generate an easy detectable signal in the gas detector an intensity of 20 nJ per fiber is necessary at 293 nm wavelength and about twice as much at 248 nm wavelength.

5.4 The TPC laser system

In the HARP TPC a matrix of 198 aluminized fibers has been installed downstream the high voltage membrane. The aluminized ends of the fibers enter a few mm inside the gas volume through 3 mm diameter holes drilled on the HV membrane. The fibers are hold in place by a fiber glass-NOMEX honeycomb structure to which special metallic supports are glued. Behind the honeycomb structure all the fibers are gathered together inside a special flexible and protective cable which guides them to the laser . The fiber bundle is 5 m length in total, of which the last 2m are naked, separated fibers, and is connected, by an optical connector, to a Krypton Fluoride excimer laser.

5.4.1 The Krypton Fluoride excimer laser

The laser used in the TPC is a Krypton Fluoride excimer laser [67] which main specifications are described in Tab. 5.3. The laser beam is fed into the fiber bundle through the optical system of Fig. 5.5 [1]. By changing the distance between the bundle end and the diffuser, the bundle light collection can be varied by a factor ~ 5. The 1% filter in front of the bundle reduces the beam energy to our needs. In the bundle delivered to us, according to specifications, the light transmission is quite homogeneous: 90% of the fibres have a light transmission between 1 and 0.25, while 10% of them have a transmission below 0.25 (in arbitrary units). For example, 90% of the fibres will have a light emission above 60 nJ (per pulse) while none will exceed 240 nJ.

[1] This optical system has been designed and made by Lasertechnik Berlin [64]

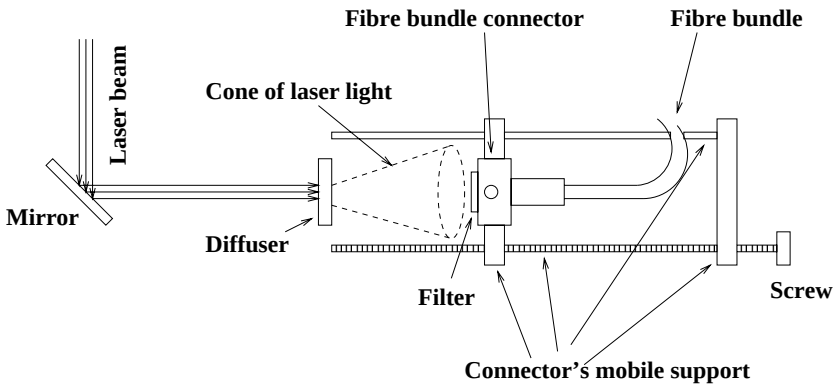

Fig. 5.5: Schematic layout of the optical connector connecting the optical fibers bundle and the laser.

5.4.2 Fiber position

The nominal position of the fibers has been chosen in order to assess field distortions in the regions where we expect them to be more severe. This regions are those close to the spokes and to the field cages (Fig. 5.1). The number of fibers has been chosen in order to have maximum redundancy without having superposition of signals onto any pad according to the PRF measured in the prototype. There are a total of 33 fibers per sector, covering essentially the sector boundaries. The fibers along the radius in the middle of the sector are intended to assess distortions, and any radial dependence of them, far from the spokes. The design distance between fibers is 49.5 mm in the radial direction and 29.25 (32.5) mm in the $r\phi$ direction for the innermost (outermost) row. The real position of the fibers, once mounted, was measured as explained further below in this section.

5.4.3 Mechanical support of the fibers

Fig. 5.6 shows a schematic layout of the mechanical structure that holds the fibers in place. The aluminized end of the fibers enters the drift volume through a matrix of holes on the HV membrane. These holes have a diameter of 3 mm and MC simulation has shown that they do not generate significant electric field distortions [34]. Each fiber is glued inside a metallic support like that of Fig. 5.7, which at its turn is kept in place by the honeycomb structure. The metallic supports traverse the honeycomb through a matrix of holes of 0.6 mm diameter, each at the nominal position of a fiber and produced by a numerically controlled machine. As explained in Chapter 4, both sides of the honeycomb are aluminized and kept at the same voltage as the HV membrane. The HV is provided to the aluminum fiber coating through the metallic supports which are glued with conductive glue to the aluminum coating at one side and to the aluminized honeycomb at the other. The mechanical support has therefore the following requirements:

- HV must be provided to the aluminum coating of the fiber.
- The honeycomb structure must be gas tight since the gas tightness of the detector relies on the honeycomb.

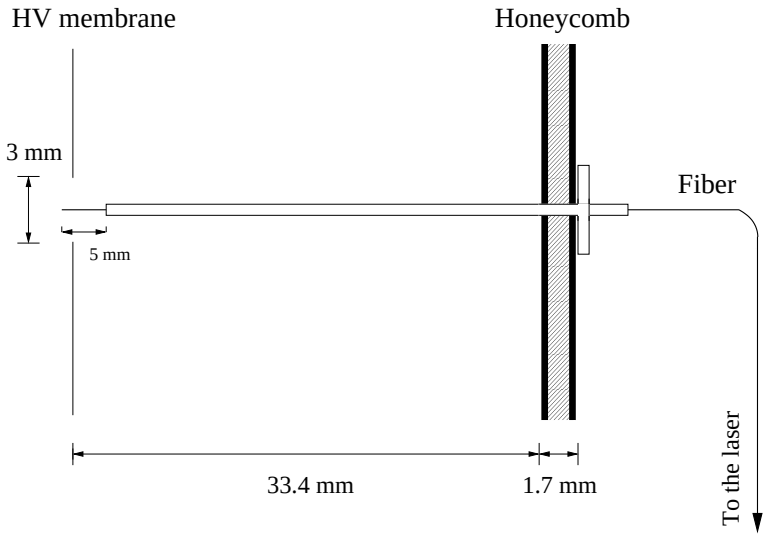

Fig. 5.6: Schematic layout of the fiber support structure.

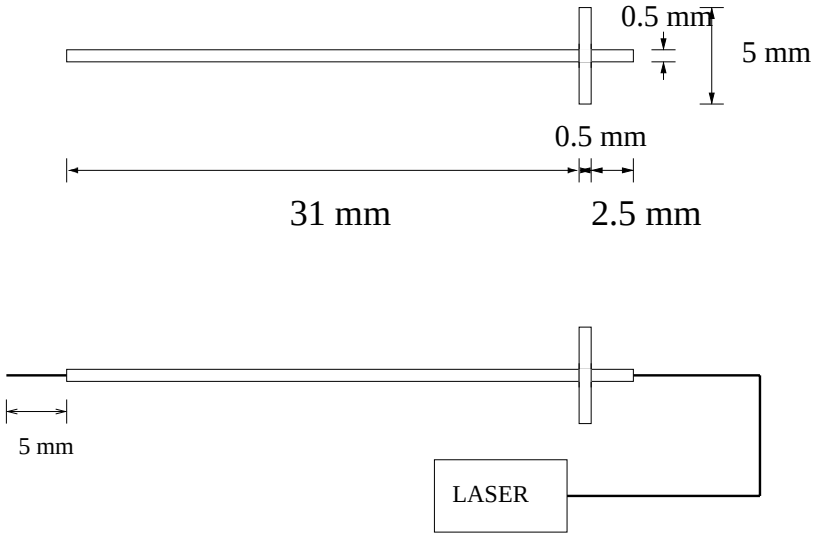

Fig. 5.7: Fiber support.

- Once the fibers are aluminized, any risk of rubbing with any material, especially metals, should be avoided.

5.4.4 Fiber support manufacture, fiber aluminisation and mounting on the honeycomb

In order to avoid any rubbing between the aluminum coating of the fibers and the metallic supports, the fibers have been aluminized once mounted on the supports. Due to the size of the honeycomb (800 mm diameter) it is not possible to aluminize the fibers once

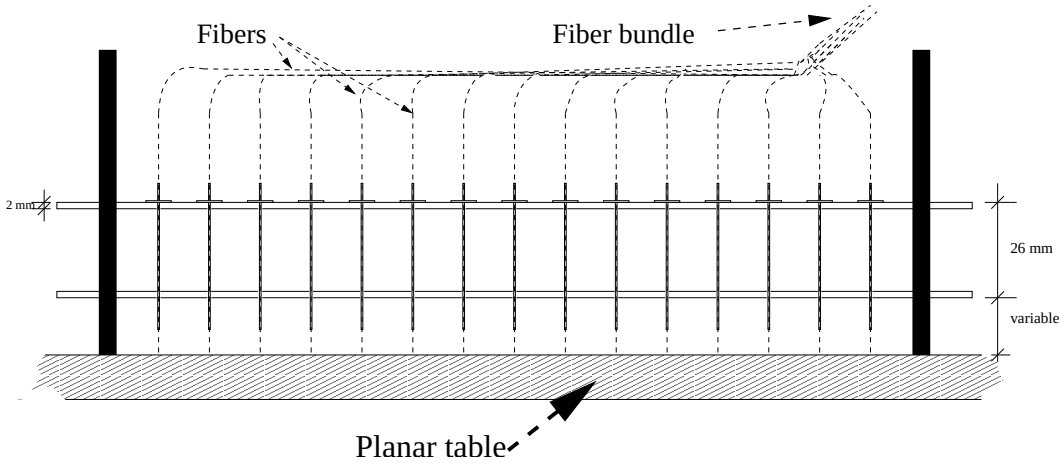

Fig. 5.8: Mechanical structure used to mount the fiber supports, fiber mounting and fiber aluminisation.

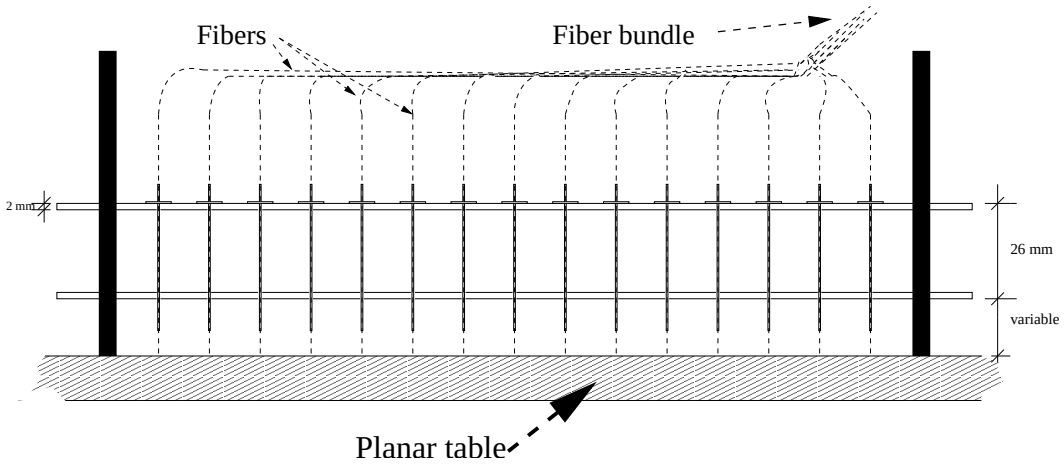

Fig. 5.9: Mechanical structure used to mount the fiber supports, fiber mounting and fiber aluminisation.

mounted on the honeycomb, the aluminum deposition inhomogeneity would be above requirements. Therefore we have first built the metallic supports and mounted the fibers in them. Then the fibers have been aluminized (and part of the supports) and afterwords they have been mounted on the honeycomb. Where necessary, electrical contact has been provided by means of conductive glue. The fibers have been aluminized down to 10 mm from the end and then pulled 5mm inside the supports. A drop of conductive glue between the fiber and the support assures the electrical contact between them.

All the process has been done by means of a mechanical jig that allows fiber support construction, fiber mounting, fiber aluminisation and fiber gluing to the fiber support, Fig. 5.9.

It consists of two parallel planes (40 $\times$40 cm^2) of aluminum separated by a 26 mm distance (outer faces) and kept parallel to a planar table at a variable distance. Each plane contains a matrix of 0.6 mm ϕ holes at a distance of 25 mm one from each other. The fiber

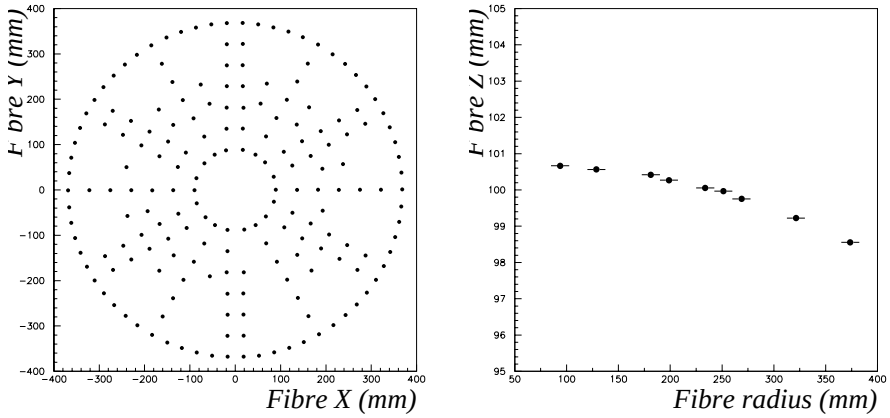

Fig. 5.10: Position of the fibers.

supports are an amagnetic steel capillary tube [63], of 0.28 mm inner diameter, glued with conductive glue to an aluminum disk of 5 mm outer diameter and 0.5 mm thickness. The capillary tubes were cut at CERN by electro-erosion. This technique was the only one among the various tried (micro-machining, chemical erosion, cutting) that did not distort the tube ends, which would prevent the fiber to enter into tube without damage. The aluminum disks were cut from an aluminum bar using the same technique and holes of 0.6 mm at the center of the disks were done using standard techniques. The jig of Fig. 5.9 allowed to glue the disks perpendicularly to the capillary tubes, as well as the fiber insertion and preliminary fixation into the tubes keeping the fibers ends 10 mm out of the tubes. All the fibers were aluminized kept together by the jig and then pulled until the end of the fibers was at 5 mm from the end of the tubes (the position had been previously marked on the fiber).The fibers were glued to the upper ends of the capillary tubes with epoxy deposited with a very thin needle in order to seal the space between the fibers and the walls of the tubes. Afterwords, the fibers, with the respective supports, were removed from the jig and introduced through their respective holes in the honeycomb, to which, the disks were glued by means of conductive glue. Finally, once mounted on the honeycomb, electrical contact between the aluminum coating of the fibers and the metallic supports was assured by means of conductive glue.

Measuring the fiber position

Once mounted on the honeycomb, the position of the aluminized end of each fiber with respect to a reference system on the ring supporting the honeycomb was measured by optical triangulation techniques [65]. Since the mechanical position of the honeycomb with respect to the TPC reference system is known to high accuracy the position of the fibers with respect to the TPC reference system is known with a precision of 0.1 mm. Fig. 5.10 shows the measured position of the fibers in the xy plane. Fig. 5.10 (right plot) shows the position of the fibers in the z coordinate as a function of the radius coordinate. The difference between the inner and the outer radius of ~ 3 mm is due to the fact that the honeycomb was glued to the support flange at a different temperature than the working one, leading to a deformation of the honeycomb at working temperature. Due to this deformation the fibers at the inner

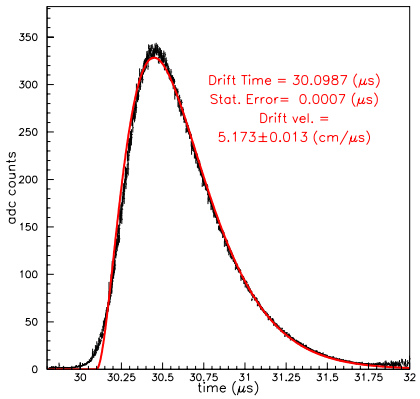

Fig. 5.11: The photoelectrons signal generated on a single pad as reconstructed with the "phase-lock" technique. The time binning is of 1 ns.

radius are $\sim$ 1 mm behind the HV membrane. However, MC simulation showed that the impact on the photoelectrons collection efficiency was negligible [34].

5.4.5 Laser trigger system

Laser data is embedded in physics data. The laser is shot about 4 times every 400 ms spill when a physics trigger occurs. The physics trigger is fed into a timer that produces a pulse of $\sim$ 100 ms which is used to veto other laser shots during the corresponding period. The laser is shot on the leading edge of the timer pulse and since the aluminized fibers are located at the downstream end of the TPC, the photo-electron signals arrive after any signal due to a track in the event that triggered the laser. The relative timing of the laser in the event is recorded in a Time to Digital converter (TDC).

5.4.6 Electron drift time monitoring

The drift time is the time delay between the laser trigger signal and the photoelectrons signals occurrence. The time of the occurrence of the signals is determined by fitting the recorded pulses to the expected pulse shape. Due to the ADC sampling frequency this results in a limited accuracy. In order to reduce this uncertainty the pulse shape is reconstructed from many events, by using the so-called "phase-lock technique", and then fitted. This technique relies on the multiple acquisition of one event, where all acquisitions have a different timing with respect to the reference "trigger". The multiple data can be used to reconstruct a much more refined information with respect to the data collected in a single event (Fig. 5.11). In HARP this technique is used to reconstruct the photoelectrons signals by using the single events occurred in one run, typically in time periods shorter than one hour, during which no big temperature or gas quality changes occur, and thus, the events are expected to be close to identical. The reconstructed signals are then fitted to the function:

$$f(t) = Q(\frac{t-t_0}{\tau})^2 \exp(-\frac{(t-t_0)}{\tau}) \tag{5.2}$$

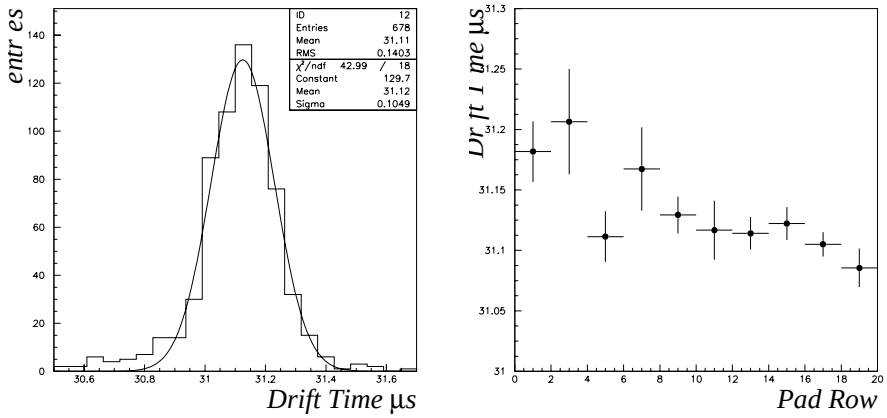

Fig. 5.12: Drift time distribution (left) and dependence with the pad row (right).

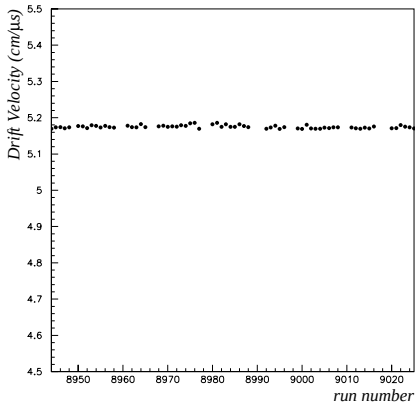

Fig. 5.13: Drift velocity for a series of 65 consecutive runs taken in 2001.

where the parameter Q is related to the charge of the input signal and t_0 is the time of its occurrence (Fig. 5.12). The drift velocity is determined from the drift time measured with the pads at a certain radius (so their signal can be related to the fibers at a constant radius) and the distance from the fibers that generated them to the anode wires (Fig. 5.13).

6. THE TPC ANALOG SIGNALS

6.1 Pulse shape

The signals generated by the preamplifiers / shapers, described in Chapter 4, differ from one preamplifier / shaper to another due to their production process. In order to characterize these signals and to study the extraction of information from the signals after the digitization process carried out in the ADC, one spare pad-plane PCB sector has been equipped with buffer cards and pico-coax cables and mounted on a setup that allows the excitation of a single pad by means of a probe directly soldered on the read-out pads. To best reproduce the signals generated in normal TPC working conditions, we have focused on the signal induced by the leading edge of a positive step function reaching the read-out pads through a capacitor of 15 pF. The positive step function emulates the positive charges cloud formation in the detector while the capacitor reproduces the coupling between the read-out pads and the detector volume. The signal generated in 46 different channels by the same input signal has been digitally recorded with a 2.5 Gs / s oscilloscope. Fig. 6.1 shows a typical pulse while the distributions of maximum amplitude and FWHM for the 46 recorded pulses are reported in Fig. 6.2. The average rise time (calculated as the time needed to go from 10% of the maximum amplitude to the maximum amplitude) is 51 ns on average with an RMS equal to 8 ns. Note that in this setup the ADC digitization in not performed and that the recorded

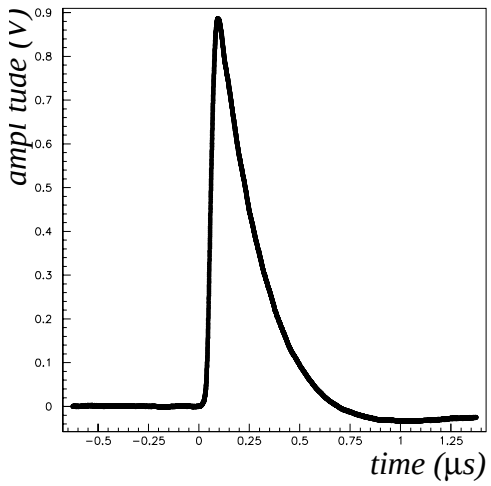

Fig. 6.1: A typical TPC analog signal as recorded with the oscilloscope at the output of the buffer card.

pulse shapes will slightly differ from those of the real setup. This difference can be quantified

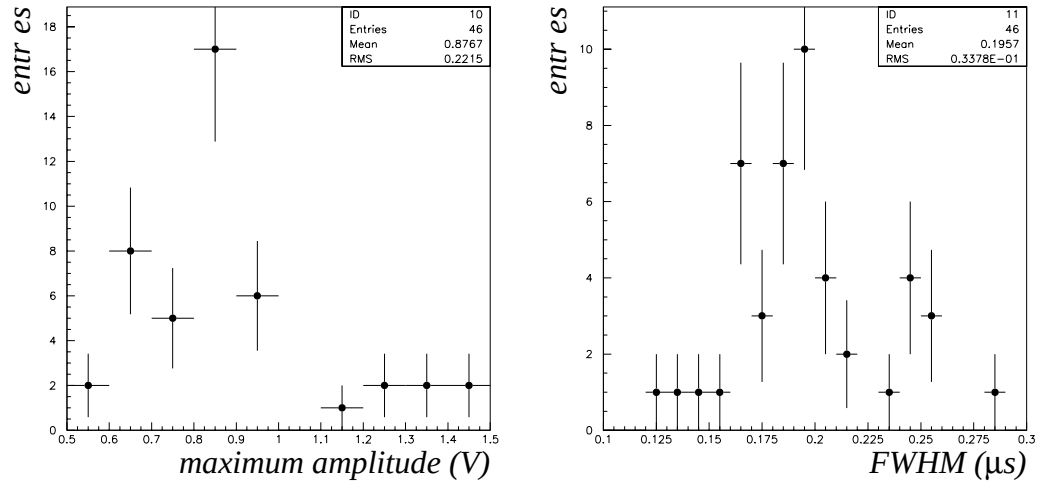

Fig. 6.2: Distribution of maximum amplitude and FWHM for a set of 46 channels. Each channel was excited individually and the signal generated by its preamplifier / shaper was recorded with an oscilloscope.

by simulation of the ADC equivalent circuit described in Sec. 4.6.

6.2 Digitization

In order to study the extraction of information from the digitized signals, the digitization process of each recorded pulse has been simulated taking into account the <100 ns jitter between the ADC start and the reference trigger. Different estimators for time and charge have been studied on a sample of 500 digitalizations of each recorded pulse.

6.3 Time and charge estimators

Due to the fast rise time of the generated pulses, different digitalizations of the same analog signal may differ significantly depending on the jitter phase, resulting on a limited resolution for time and charge estimators. The best estimators will be those which calculation requires less computing time for the best resolution. For the time estimator, the requirement on minimum bias for each pad is needed while this is not the case for the charge estimator since any bias will be taken into account by single pad calibration. The estimators we have studied are the following:

- Fit of the digitized signal by a "gamma" function:

$$f(t) = Q(\frac{t - t_0}{\tau})^2 e^{-\frac{(t-t_0)}{\tau}} \tag{6.1}$$

  Where Q is a constant linearly related to the input charge and t_0 is the time of its occurrence.

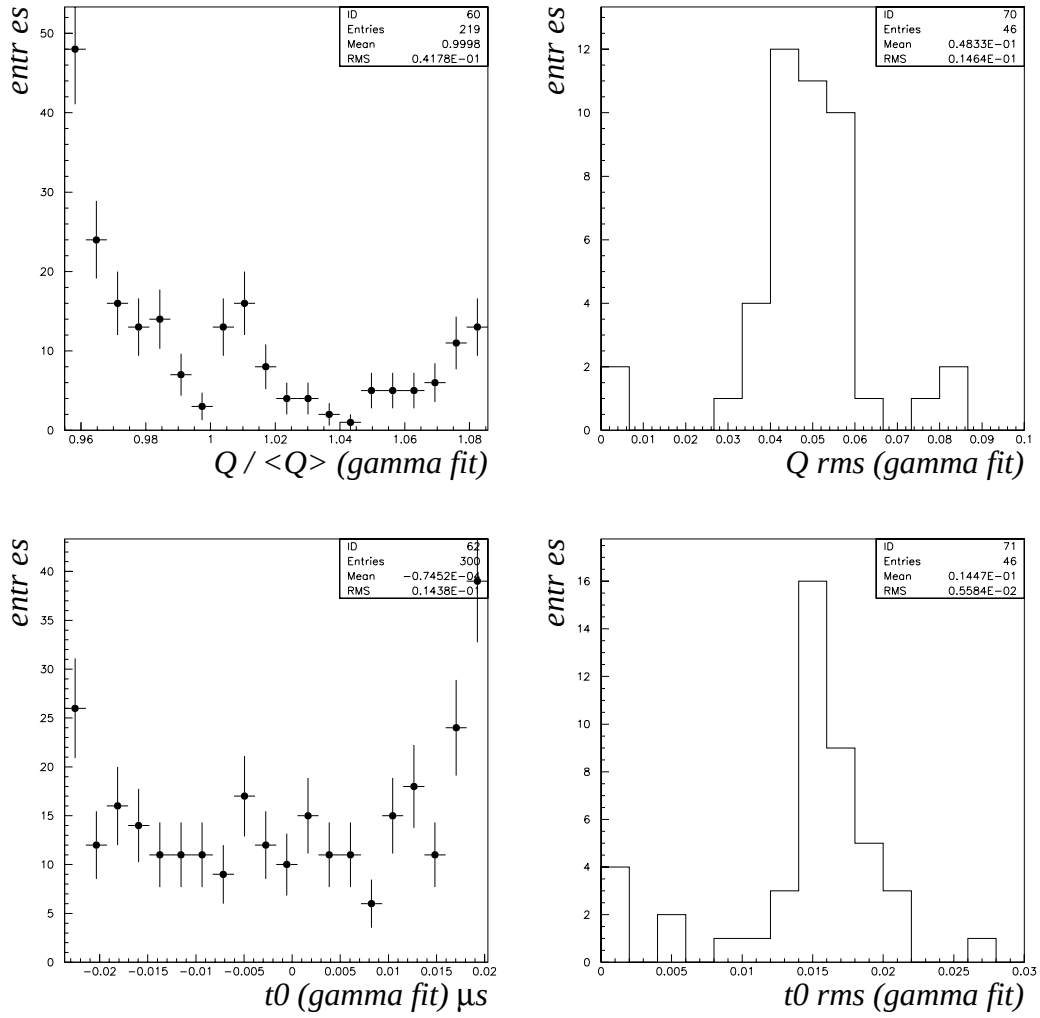

Fig. 6.3: Left: Distribution, for 500 digitalizations of the same pulse, of the parameter Q (t_0) -upper, down plot-, obtained by fitting the discrete pulses to a "gamma" function, divided by its mean value. Right: distribution of the root mean square of the distributions, like the ones to the left, obtained for the 46 recorded pulses.

- Fit of the digitized signal by a semi-gaussian function:

$$f(t) = Q(\frac{t - t_0}{\tau})^n e^{-n\frac{(t-t_0)}{\tau}} \tag{6.2}$$

  leaving n as a free parameter. Other parameters have the same meaning as in the "gamma" fit [1].

- Maximum of the digitized signal, hereafter referred to as DM. This is the maximum value among the discrete amplitude measurements in a single signal discretization.

[1] Both functions are motivated by the shape of the analog signals recorded with the oscilloscope and those resulting from the simulation of the preamplifier response. These, are very well fitted by both functions.

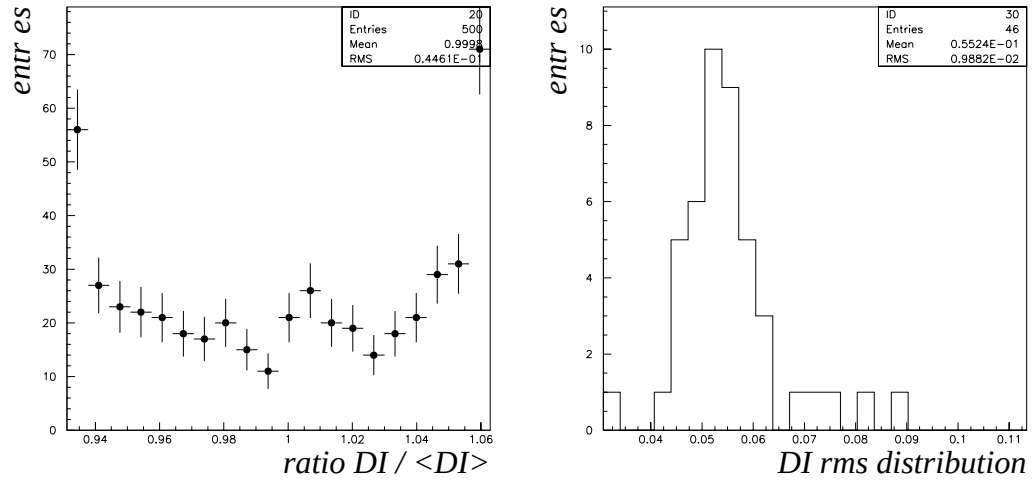

Fig. 6.4: Same distribution that in Fig. 6.3 but for the parameter DI.

- Discrete integral, hereafter referred to as DI. This is the sum of all discrete amplitude measurements in a single signal digitization.
- Linear approximation to t0, hereafter referred to as Dt_0. It is the position where the tangent to the pulse shape, computed on the leading edge for the time corresponding to half maximum amplitude, intercepts the time axis.

Both fits give similar results. For the case of the "gamma"fit the resulting resolutions are of 4.8% for Q and 14.5 ns for t_0, as reported in Fig. 6.3. Clear non gaussian effects are present in the distribution of Q and t_0 for the same pulse. These non-gaussian distributions come from the non gaussian dependence of the parameters with the phase of the jitter, mostly affected by the fast rise of the pulse. The resolutions obtained with the semi-gaussian fit are 4.4 % for Q and 14.3 ns for t_0.

The distribution of DI, DM and Dt_0 also have a non gaussian form, as illustrated by Fig 6.4 for the estimator DI, and the corresponding resolutions are 5.5% for DI (Fig. 6.4), 3.2 % for DM and 24 ns for Dt_0. The bias on Dt_0 is, averaged over the different pulse shapes, of 76 ns to the left ($Dt_0 < t_0$).

6.4 Estimators Correction

Fig. 6.5 shows the ratio between the reconstructed quantities and the average reconstructed quantity as a function of the simulated jitter. In practice, this phase is not known. However, any parameter built from amplitude measurements in a single discretized pulse is correlated with the phase of the jitter, and therefore, carries information about it. The aim of this study has been to extract this information from the pulse itself and use it to correct the value of the estimator. The following jitter estimators have been studied:

- ratio of the amplitude measurement immediately after the maximum amplitude measurement and the maximum amplitude measurement itself, hereafter called $r1$.

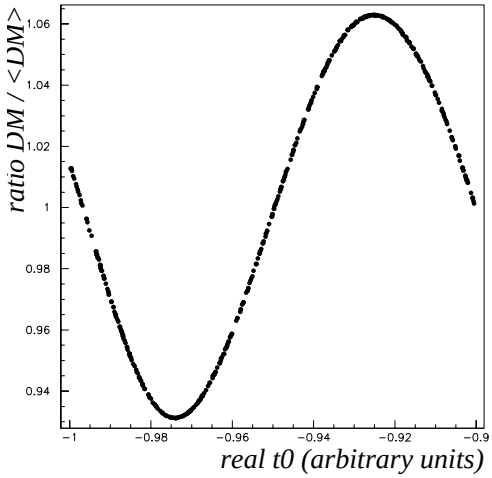

Fig. 6.5: Value of the DI estimator as a function of the the jitter value.

- ratio of the second amplitude measurement after the maximum amplitude measurement and the first amplitude measurement after the maximum, hereafter called $r2$.
- ratio of the amplitude measurement immediately before the maximum amplitude measurement and the maximum amplitude measurement, hereafter called $r3$
- ratio of the maximum amplitude measurement and the FWHM of the discrete pulse, hereafter called r4. The FWHM has been calculated as the distance between the two data points resulting from the intersection between the constant line at one half of the maximum discrete amplitude and the lines passing through the two points immediately above and below of this line.

The values of these parameters are correlated with the phase of the jitter and thus, with the estimators described previously. As an example, Fig. 6.6 shows the correlation of DI with the parameters described above. The $r3$ parameter is very sensitive to the jitter, this is due to the fact that one of the measurements used to build it sits on the fast raise of the pulse and depends strongly on the jitter phase. The $r4$ parameter is ambiguous. The correlations of the estimators with the parameters $r1$ and $r2$ have been used to built a correction of the estimators as a function of $r1$ and $r2$, independently (Fig. 6.7).

Correction functions for DI, DM and Dt_0 for each pulse, have been built with the two parameters independently. Resulting resolutions after correction are reported in Tab. 6.1.The correction functions as a function of $r2$ give slightly better resolutions. This is due to smoother dependency of the estimators with this parameter. Comparing Fig. 6.4 and Fig. 8.10 it is clear that after correcting, not only the resolutions are improved but 90% of the single measurements are within 0.12% of the central value, while before correction are within 6.0%. The dependence of these estimators on the pulse shape has been studied by:

- employing the correction functions of each single pad on the pulse shapes of other pads resulting in no improvement of the resolutions.

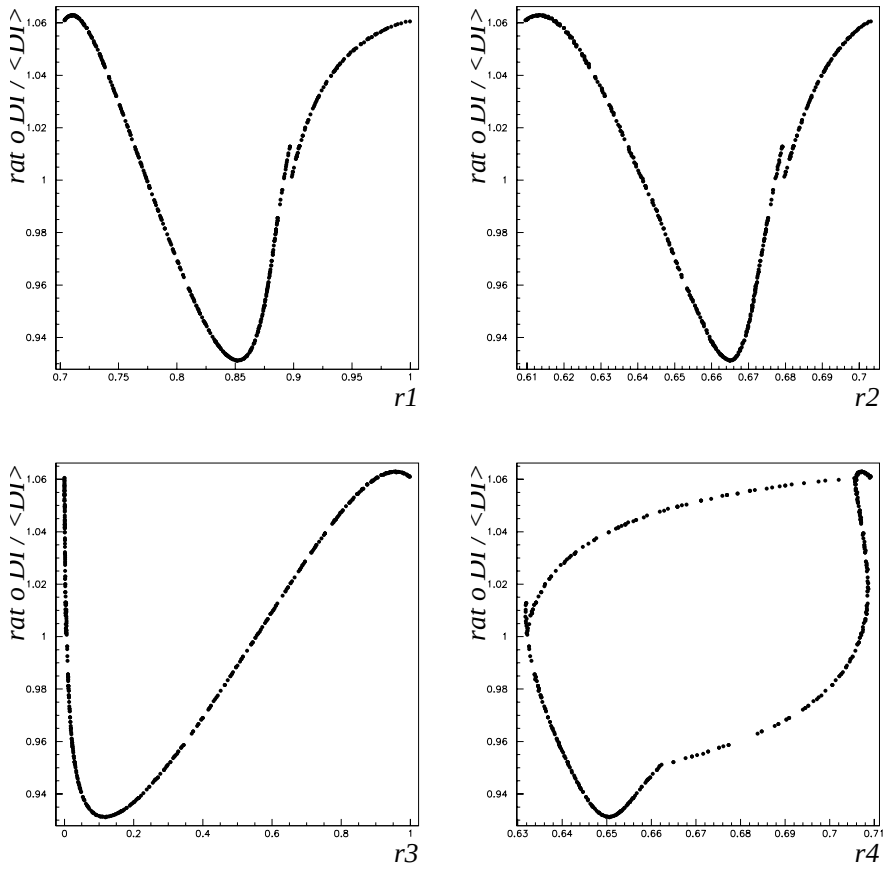

Fig. 6.6: Correlation of the DI estimator with the parameters $r1$, $r2$, $r3$ and $r4$.

	No correction	f_{r1} correction	f_{r2} correction
σ_{DI}	5.5%	0.7%	0.3%
σ_{DM}	3.2%	0.6%	0.2%
σ_{Dt_0}	24 ns	12 ns	12 ns

Tab. 6.1: Comparison of the resolutions obtained with the different correction factors.

- by applying the correction functions constructed with an average pulse shape on the pulse shapes of the specific pads. The average pulse shape has been computed by summing the 46 normalized recorded pulses, each shifted in time so the maximum amplitudes occur all at the same time. No improvement is reported due to the fact that this average pulse is smoother than the individual pulses and it has a bigger raise time (74 ns).

However, the two combined tests hint that knowledge of individual pulse shapes is of fundamental importance.

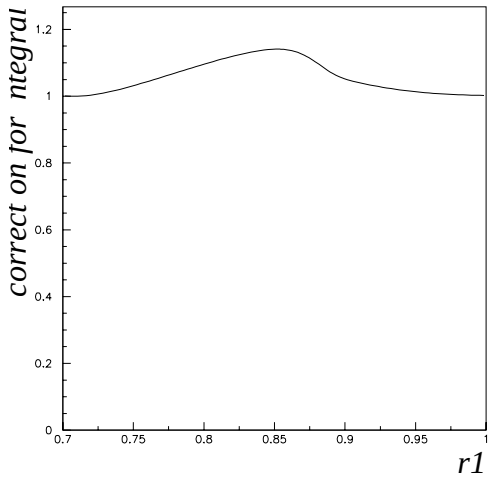

Fig. 6.7: Correction function for DI as a function of $r1$ for the pulse of Fig. 6.1.

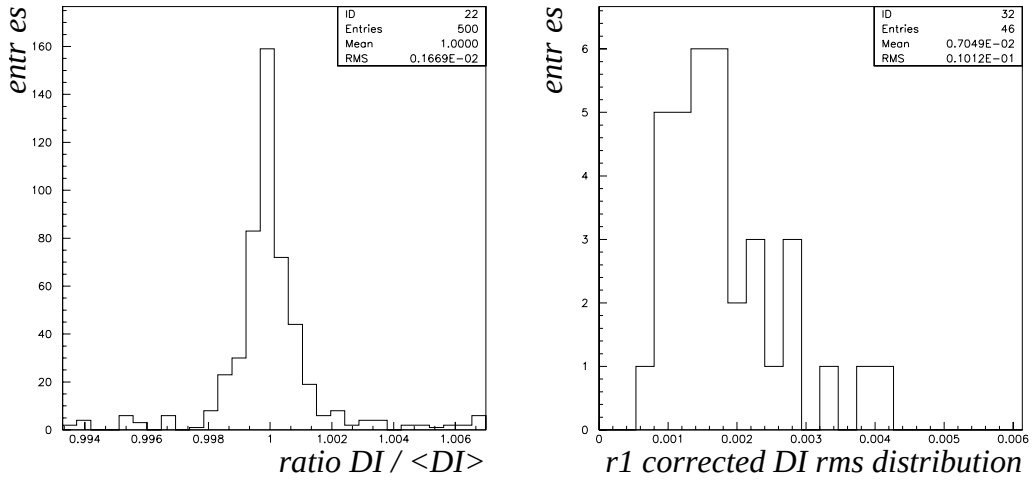

Fig. 6.8: Left: Distribution of corrected $DI/ < DI >$. The correction has been performed with the function of Fig 6.7 and over a sample of 500 simulated discrete measurements of the pulse of Fig. 6.1. The sample used to built the correction function is different from that on which has been tested. Right: Distribution of the rms of the corrected $DI/ < DI >$ according to the value of $r1$ for the 46 studied different pulses. A correction function for each pulse has been built and the samples on which resolution is tested are different from those used to built the functions.

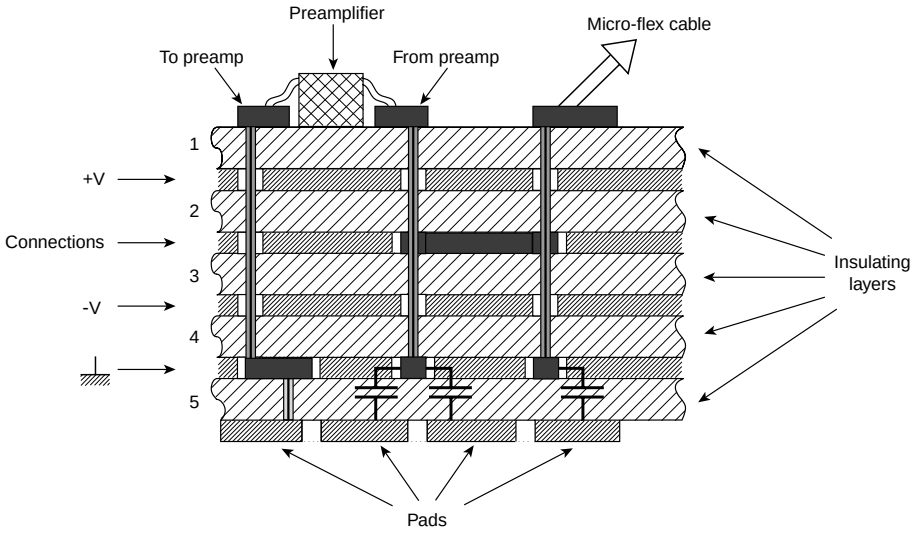

Fig. 6.9: Cross-section of the pad plane. The points of possible capacitive coupling between vias carrying signals before and after amplification are marked. Note that the vertical vias traverse almost all the pad plane independently of the distance between the layers they are putting in contact.

6.5 Cross-talk

In the TPC front-end electronics a cross-talk effect has been observed for a number of channels. We have traced this undesired effect to be generated by capacitive coupling between the output of one preamplifier and the input of another (possibly the same one) and it is due to the physical proximity inside the pad-plane of the vias carrying the signals before and after amplification (Fig 6.9). Due to the physical origin of the effect, we expect the capacity of the coupling to be symmetric between sectors up to 10%, which is the precision of the printing process of the pad-plane, mainly materials thickness, assembling and alignment. In order to identify the existing cross-talk relations and to model the effect, a series of tests with two spare sectors have been performed. Both sectors were already equipped with electronic components and micro-flex cables, and were attempt as substitutes of sectors of the pad plane in case of damage or malfunction. For the tests, they have been equipped with buffer cards and power supplies and they have been mounted in different setups that allow for pad excitation by means of a probe connected to a wave generator. Analysis of the data provided by both tests allows to localise, understand and quantify the cross-talk.

6.6 Cross-talk capacitive induction measurements

One sector has been mounted on a setup that allows to excite the pads by means of a probe connected to a wave generator. The probe is a simple conductor which is put in front of the pad. A backing layer of polyamide allows a signal to be induced on the pad by capacitive coupling. In order to produce a signal on the pad equivalent to the one generated by an avalanche, it is necessary to apply a step-function potential to the probe. The probe is posi-

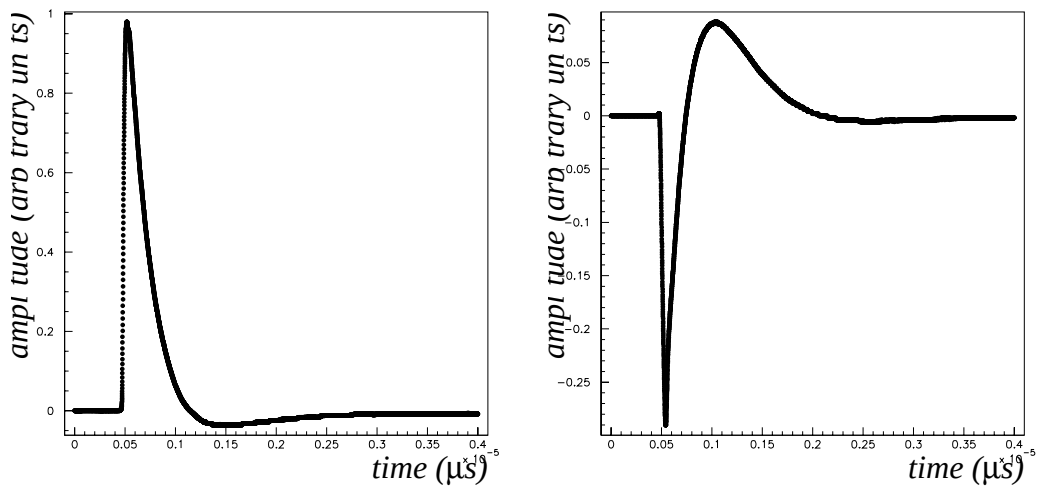

Fig. 6.10: Left: signal induced by the probe on one channel as measured with the oscilloscope. Right: cross-talk signal induced on one channel when a different one is excited by the probe.

tioned accurately in the middle of the pad by means of a mechanical pivoting support. On the contrary, the distance between the probe and the pad (nominally $\sim$1 mm) is not controlled accurately and therefore, the induced signals on different pads are not identical. As a consequence of this, no quantitative studies on cross-talk intensity are possible. In addition, we realized that also neighbouring pads are excited with a signal which is $\sim$10% the signal of the centred pad. For a limited number of excited channels, other channels belonging to the same micro-flex have been scanned with a digitising oscilloscope in order to find, and characterise, cross-talk signals induced by the excited channel (Fig. 6.10). For all channels of the sector, data has been collected in parallel by means of the TPC DAQ.

In order to make a digital map of the cross-talk relations, each channel has been excited while the data generated in all of them has been recorded. This method has an "a priory" limited efficiency due to the fact that cross-talk signals with a maximum positive amplitude below the ADC threshold (10 adc counts) are not recorded. In order to reduce this inefficiency, the input signal amplitude has been set to a large value corresponding to $\sim$ 200 ADC counts, which is about four times larger than those generated by a typical cosmic ray. Also, the negative part of the cross-talk signals is never recorded. In addition, the signal directly induced by the probe in the neighbouring pads superimpose on any possible cross-talk signal. Since the ADC only record the positive part of the signals, it can be evinced from Fig. 6.10 that cross-talk signals can be distinguished from direct signals by the time of maximum amplitude occurrence (Fig. 6.11).

The pulse shapes generated in each channel have been reconstructed using the "phase-lock" technique by taking $\sim$4000 measurements for each pad. Cross-talk signal identification has been performed automatically by an algorithm based on the time of maximum amplitude. Noisy signals have been removed by applying the following cuts:

- A signal to noise ratio > 6, for each bin, is required.

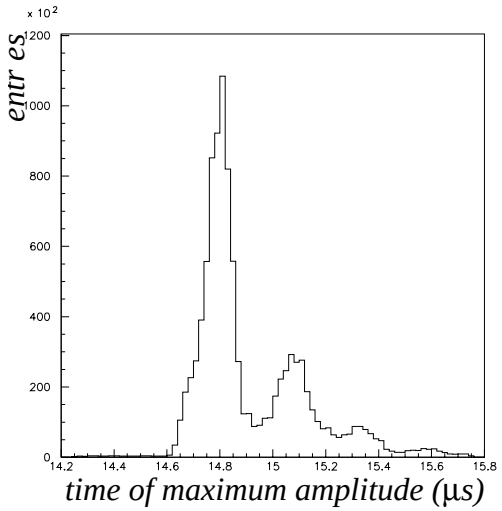

Fig. 6.11: Distribution, for raw data, of the time at which the amplitude is maximal. The first peak corresponds to the samples directly induced by the probe and the second one corresponds to first order cross-talk signals.

- More than 4 consecutive bins are required to define a pulse.
- A maximum amplitude bigger than 5% of that of the signal corresponding to the excited pad. This is to avoid noisy signals generated by channels with an atypical high gain.

Applying this cuts a 100% noisy signals rejection is achieved with a negligible reduction in efficiency verified by removing the cuts.

Of the initial 662 channels corresponding to one sector, this sector had 65 not working preamplifiers and 7 broken preamplifiers. The reason of such a high fraction of not working channels is that a few micro-flexes were badly soldered onto the PCB and did not transport correctly the power supply to the preamplifiers. In the remaining 590 channels, 644 cross-talk relations were found. The number of channels inducing a cross-talk signal (also called leading pads) is 364 and the number of pads that can receive a cross-talk signal (also called satellites) from $\geqslant$1 pad is 262, as reported in the first column of Tab. 6.2. The physical relative position between the involved pads is reported in Fig. 6.12. The purity of the map has been determined by eye-scanning the identified cross-talk signals with an oscilloscope and a purity >95% has been estimated.

6.7 Cross-talk direct signal injection measurements

On a sector different from the one used for the tests described above, a total of 46 channels, corresponding to two micro-flexes, have been excited by means of a probe directly soldered onto the readout pads. The probe is connected to a wave generator through a 15 pF capacitor. The aim of this capacitor is to emulate the coupling between the detector and the readout pads. Like in the previous setup, the wave generator provides a positive step function. We

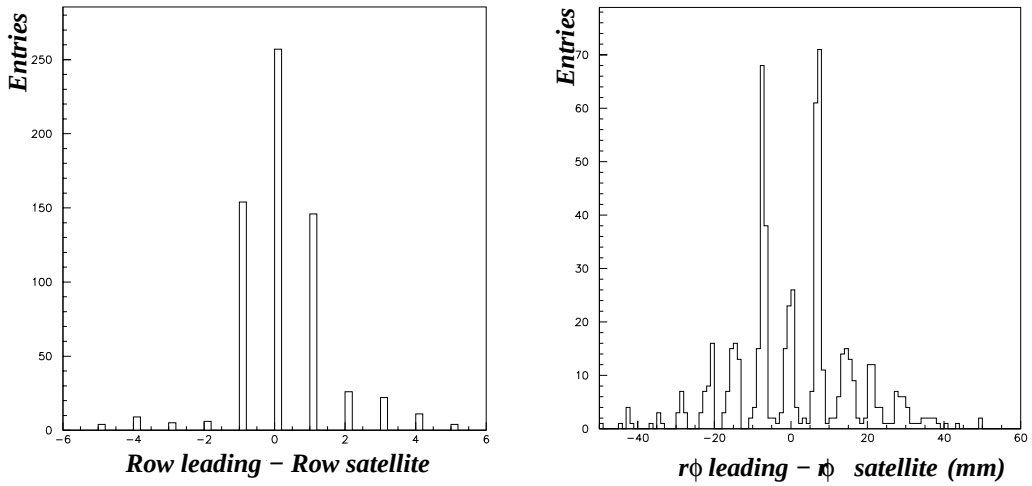

Fig. 6.12: Left: Distance, expressed in "row number", between the leading and the satellite pad. Right: Distance in the rϕ direction, expressed in mm, between the leading and the satellite pad.

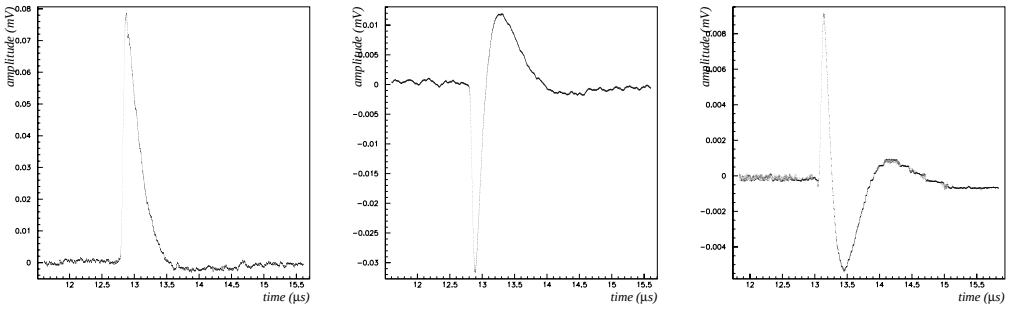

Fig. 6.13: Typical signals observed corresponding to: (left) direct excitation, (centre) first order cross-talk, (right) second order cross-talk.

have tuned the amplitude of the step function (4 mV) so that the average output signal maximum amplitude is similar to those produced by cosmic rays in the TPC. With this setup, the input signal injected in each pad is guaranteed to be equal and, in addition, one and only one pad is excited directly by the probe. For each excited pad, the signals generated in all the channels belonging to the same micro-flex have been digitally recorded by means of a 2.5 Gs/s oscilloscope. Fig. 6.13 shows the three different types of signals observed corresponding to direct signal, first order and second order cross-talk signal. We define second order signals the cross-talk that appears to be originated by a cross-talk signal, as will be directly verified later. Despite of the relative high amplitudes of the cross-talk signals, most of the area above zero cancels with that from the negative part, and, on average, the integral of the cross-talk signals is 5% that of the inducing signal. Fig. 6.14 shows the charge of the

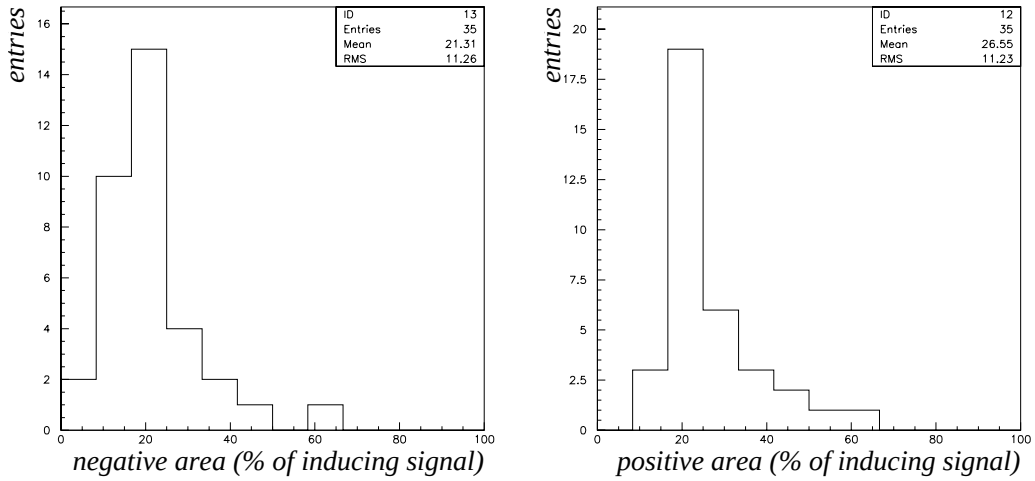

Fig. 6.14: Distribution of the integral of the negative (left) and positive (right) part of the observed cross-talk signals in units of percentage of the total integral of the inducing signal.

	Induced signal test	Directly injected signal
# of channels	590	46
# of 1st order relations	644	45
# of 2nd order relations	-	14
# of ch. with 0 satellites	226	12
# of ch. with 1 satellite	203	26
# of ch. with 2 satellites	86	7
# of ch. with 3 satellites	43	1
# of ch. with >3 satellites	32	0
# of ch. with 0 leadings	328	24
# of ch. with 1 leading	106	8
# of ch. with 2 leadings	70	9
# of ch. with 3 leadings	32	4
# of ch. with >3 leadings	54	1

Tab. 6.2: Comparison of the digital maps obtained in the two different setups.

cross-talk signals as a percentage of the charge of the inducing signals for the positive and negative part of the curve. The map of observed second order cross-talk is 100% coherent with that of first order cross-talk. This means that, for all events in which channel A generates a second order signal in channel C, it also generates a first order signal in channel B, which (when excited with the probe) generates a first order signal in channel C. The number of cross-talk relations that have been found, their type and the number of corresponding satellite and leading channels related to each channel are reported in the second column of Tab. 6.2.

6.8 Comparison of the cross-talk measurements

In order to cross-check the methods, we have compared overlapping data samples. These are the relations involving two channels for which data has been taken with both methods (all channels of direct injection measurement). For a total of 46 channels entering the sample, in the capacitive induction measurement we find a total of 26 first-order cross-talk relations to be compared with the 45 found in the direct injection measurement.

This hints that the direct injection method has a much higher efficiency than the one by capacity induction, and assuming an efficiency of 100% for the first (verified by eye scan with the oscilloscope) we estimate an efficiency of $\sim$70% for the latter method. Of the 26 relations found in the capacitive induction measurement 23 are present in the sample of the other method, This verifies that two different sectors behave almost identically. Given the higher quality of the direct injection data, the conclusions from this data are more meaningful, and could be summarised in:

- $\sim$26% of the channels have 0 satellites within the same micro-flex.
- $\sim$74% of the channels have $\geqslant$1 satellites within the same micro-flex.
- $\sim$52% of the channels have 0 leading pads within the same micro-flex.
- $\sim$28% of the channels have $\geqslant$1 leading pads within the same micro-flex.

6.9 Cross-talk model

Experimental evidence, mainly the form of the cross-talk signals (Fig. 6.13) and the unidirectionality of the effect hint that the effect we are dealing with is an input-output cross-talk resulting from a capacitive coupling. We intend to reproduce the cross-talk signals by studying, in the fourier space, the response of the preamplifiers, and considering a capacitive coupling between the output of the leading channel and the input of the satellite one. A capacitive cross-talk relation can be described on the basis of three elements (Fig 6.15):

- the capacitive coupling, characterised by a capacity C, between the leading channel preamplifier output and the satellite pad preamplifier input,
- the transfer function, $T_S(w)$, of the satellite channel preamplifier, defined as the response to an input of Dirac delta function of unitary charge,
- the leading preamplifier output signal.

The cross-talk signal, $X(w)$, in channel "S", resulting from an arbitrary excitation of pad "L" generating a signal $f(w)$ in channel "L" is:

$$X(w) = -iw\, C_{L\to S}\; f(w)\, T_S(w) \tag{6.3}$$

where $C_{L\to S}$ is the capacity of the coupling between the channels "L" and "S".

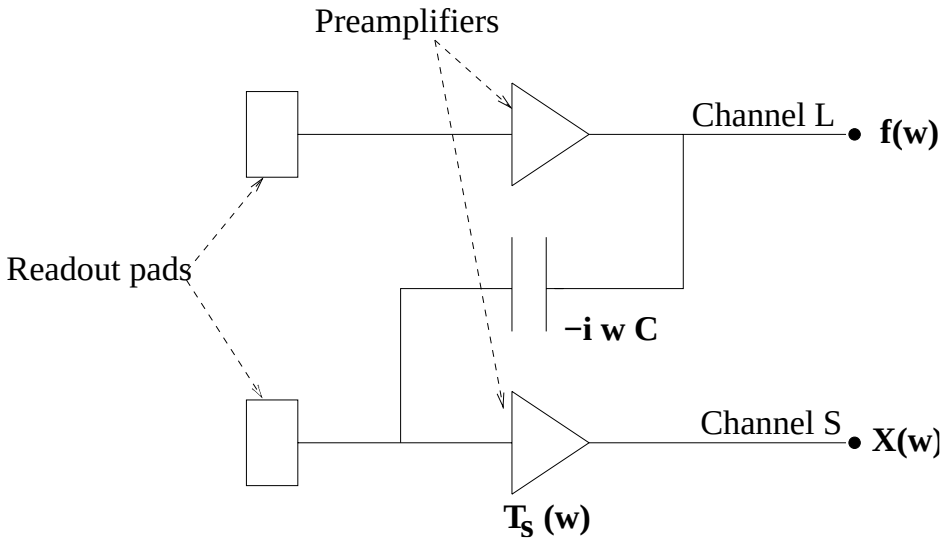

Fig. 6.15: Schematic layout of the capacitive preamplifier output-input capacitive coupling.

6.9.1 Preamplifiers transfer function

Under the hypothesis that the injected input signal (described in Sec. 6.7) is a Dirac delta function of charge Q, we can use the output signals generated in channel i, called $g_i(t)$, to build the transfer function of its preamplifier, $T_i(w)$, as the fast fourier transform [68] of the recorded signal $g_i(t)$ normalised to the input charge:

$$T_i(w) = \frac{FFT\{g_i(t)\}}{Q} \tag{6.4}$$

This method has an implicit error arising from the difference between the injected input signal generated in the laboratory and a theoretical Dirac delta function. Contrary to the theoretical delta function, which is composed of all frequencies with equal weights, the weights of the frequencies composing our input signal will be larger for lower frequencies than for higher ones. Thus, by assuming that our input signal is a Dirac delta, we are overestimating the response of the preamplifiers to low frequencies and underestimating it at high frequencies.

6.9.2 Determination of the cross-talk signals shape

For the cross-talk relations observed in the data described in Sec. 6.7, let us call $f_L(t)$ the observed signal in the channel "L" inducing the cross-talk (leading channel) and $X_S(t)$ the cross-talk signal observed in the channel "S" receiving the cross-talk (satellite channel) [2]. We can predict the the cross-talk signal by applying Eq. 8.2:

$$Y_{predicted}(w) = -iw\, C_{L\to S}\, f_L(w)\, T_S(w) \;=\; -iw\, C_{L\to S}\, FFT\{f_L(t)\}\, \frac{FFT\{g_S(t)\}}{Q} \tag{6.5}$$

[2] Note the different definition of $f_L(t)$ and $g_L(t)$. Both can be generated with the same input signal, formally $f_L(t)$ could be produced by any input signal while $g_L(t)$ is defined as the response of the channel to a precise input previously defined.

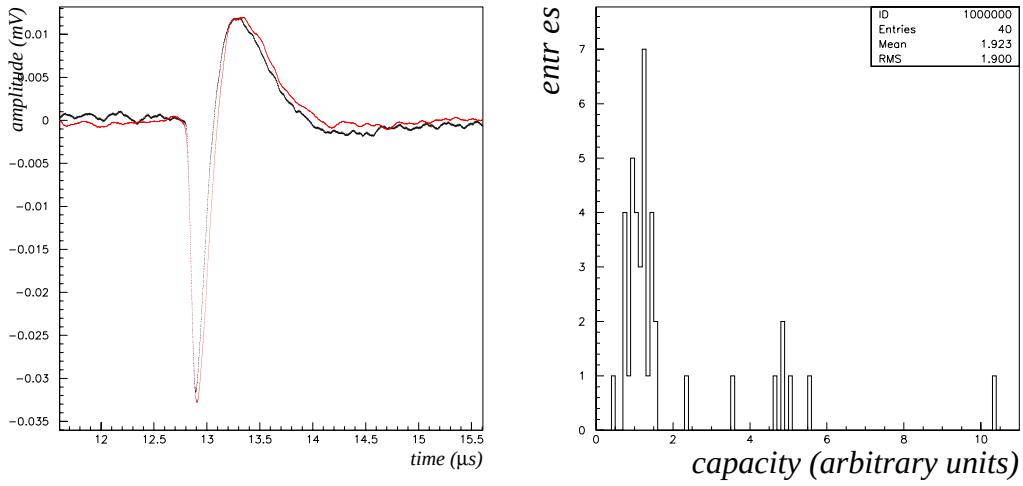

Fig. 6.16: Left: Black: measured first order cross-talk signal. Red: predicted cross-talk signal (normalised as explained in the text). Right: distribution of the measured capacity in arbitrary units.

Which shape is determined by:

$$X_{predicted}(w) = \quad -iw\, FFT\{f_L(t)\}\; FFT\{g_S(t)\} \tag{6.6}$$

Normalising $X_{predicted}(t)$ to the observed cross-talk signal, $X_S(t)$, maximum amplitude we obtain the value of $C_{L\to S}/Q$, Fig. 6.16. As shown in Fig. 6.16 and 6.17 the agreement between the predicted and the observed signals is satisfactory.

Second order cross-talk signal shapes can be predicted with the same formalism. In this case, the signal $f_L(t)$ will pass through the following elements (Fig 6.18):

- the capacitive coupling between channels “L” and “I”.
- the preamplifier of channel “I”.
- the capacitive coupling between channels “I” and “S”.
- the preamplifier of channel “S”.

Where “I” indicates the intermediate preamplifier. Thus, the predicted signal at the output of channel “S” is:

$$X_{predicted}(w) = (-iw\, C_{L\to I})\,(-iw\, C_{I\to S})\; FFT\{f_L(t)\}\; \frac{FFT\{g_I(t)\}}{Q}\; \frac{FFT\{g_S(t)\}}{Q} \tag{6.7}$$

As shown in Fig. 6.19 there is agreement between the predicted and measured shapes. Normalising the predicted signal to the measured one, we perform a measurement of the combined quantity:

$$C_{12} = \frac{C_{L\to I} C_{I\to S}}{Q^2} \tag{6.8}$$

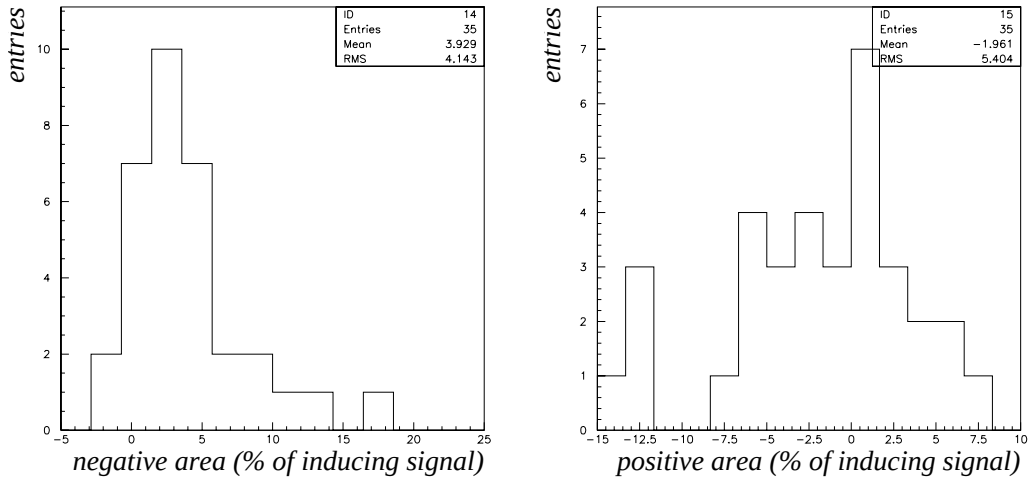

Fig. 6.17: Distribution of the integral of the negative (left) and positive (right) part of remaining area of the observed cross-talk signals once the predicted signal is subtracted. Units are in percentage of the total integral of the inducing signal.

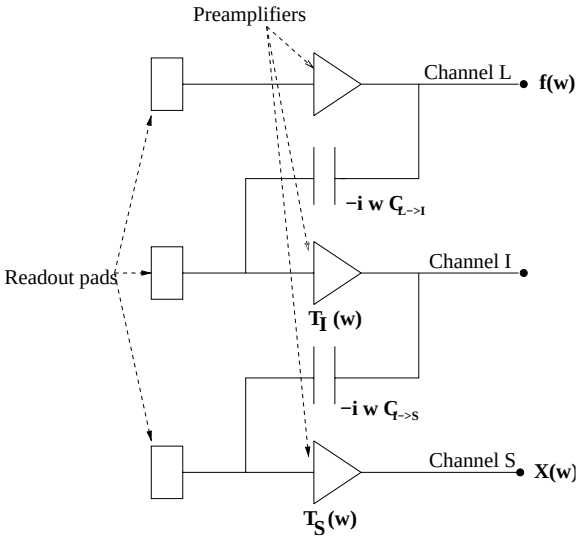

Fig. 6.18: Schematic layout of two consecutive preamplifier output-input capacitive coupling.

that can be compared to the individual measurements:

$$C_1 = \frac{C_{L\to I}}{Q} \tag{6.9}$$

$$C_2 = \frac{C_{I\to S}}{Q} \tag{6.10}$$

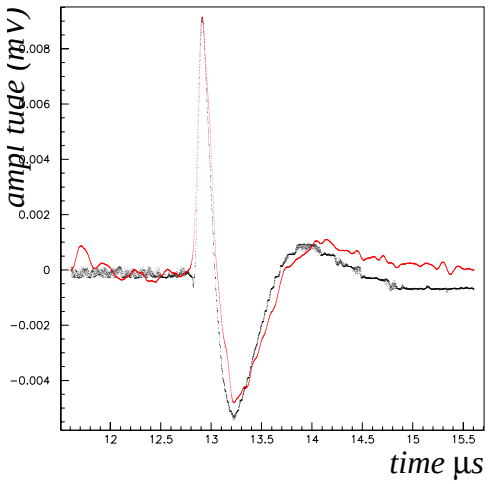

Fig. 6.19: Second order cross-talk signal. The black curve corresponds to the observed curve and the red (grey) to the predicted one once normalised to the observed one.

performed with the first order cross-talk signals. The distribution of the quantity:

$$R = \frac{C_{12} - C_1 C_2}{C_{12}^2} \tag{6.11}$$

for all found second order cross-talk relations, has a mean value of 0.2 and a root mean square of 7%. We interpret this 20% shift as an effect arising from the calculated preamplifiers transfer function. Qualitatively the input to the "S" preamplifier has a different frequency spectrum with respect to the input to the "I" preamplifier, specifically larger high frequency components. Therefore, as explained in Sec. 6.9.1, the method has a different sensitivity to the errors introduced in the measurements of the transfer function. The 7% rms allows us to estimate that the reproducibility of our measurements of C_i is of ∼3.5%, under the hypothesis that the measurement error on $C_1 C_2$ is equal to the measurement error on C_{12}.

6.9.3 Model verifications

We test the predictive behaviour of the model by looking to cross-talk signals, in channel "S", for different inputs. We have heated the preamplifier "L" in order to approach overshooting, and we have studied the cross-talk signal generated in channel "S" when channel "L" is excited. Applying the model described above we can predict the cross-talk shape as shown in Fig. 6.20, the comparison with observation is satisfactory despite the fact the input signal is far from normal.

In order to test the linearity of the model we have repeated the measurements described in Sec. 6.7 but with an input signal of different amplitudes up to ten times bigger as an extreme case (saturation). Apart from the saturated behaviour of the preamplifiers, that the model does not take into account since we measure the transfer function in the domain of linearity, the agreement of the model prediction with data with data is good even in this conditions (Fig. 6.21) and shows that the cross-talk effect is linear as expected. We conclude by

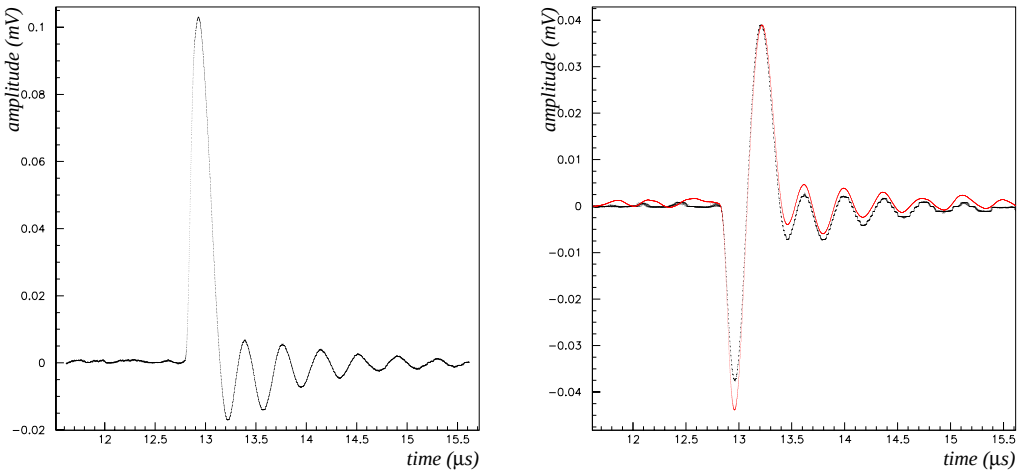

Fig. 6.20: Left: Overshooting signal generated by an overheated preamplifier. Right: Cross-talk signal induced by the signal on the left, the black (dark) curve corresponds to the measured signal and the red (grey) one corresponds to the predicted one, after normalisation.

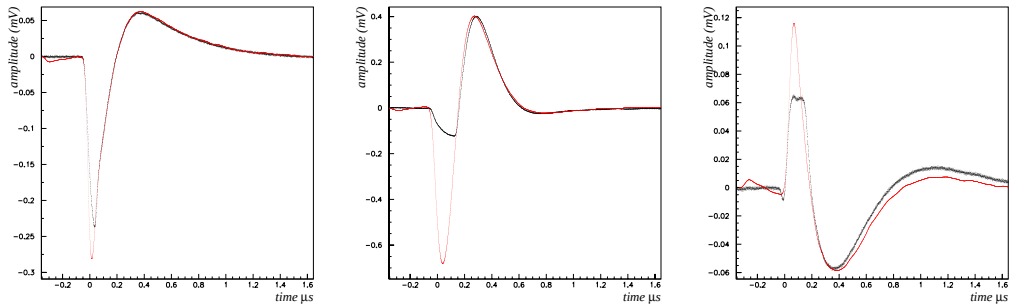

Fig. 6.21: Cross-talk signals generated with a input signal big enough to saturate the preamplifiers. The left (centre) plot corresponds to a first-order cross-talk signal generated on a preamplifier close to saturation (completely saturating). The right plot corresponds to a second order cross-talk signal where the intermediate preamplifier is in saturation. It should be noted that, outside saturation, the agreement with data remains satisfactory.

stating that the model of cross-talk, when applied to real data, reproduces the observations in the operational regime of the TPC and, by appropiate measurements, allows to correct the signals subtracting the undesired cross-talk.

7. CONCLUSIONS

A novel apparatus for the calibration of the HARP Time Projection Chamber has been designed, developed and built. The apparatus consists of a large number of point-like photoelectron sources located at precise positions inside the detector volume. The photo-electron sources are optical quartz fibers on which one end is coated with an aluminum layer of $\sim$80Å thickness and are held in place on the High Voltage membrane. The fibers are used to guide UV laser light pulses that generate photoelectrons on the fiber tips and these act as photoelectron emitters. The photoelectrons drift inside the detector and produce the calibration signals. The technique allows to asses $E \times B$ distortions and to measure drift velocity, ion feedback and time stability in real time.

The analog signals generated by the TPC front-end electronics have been characterized. Different methods to extract the amplitude and time of occurrence from the digitized signals have been studied and compared. Fast estimators, like the sum of all the discrete amplitude measurements inside one pulse, show a reconstructed amplitude and time of occurrence resolution comparable to those achieved by fitting the discrete amplitude measurements to the expected pulse shapes. The obtained relative resolutions ($\sim$5%) are limited by the aliasing effect and can be improved by an order of magnitude (up to $\sim$0.3%) by applying a correction to the estimators value which is constructed from the knowledge of the response of the preamplifier and the digitization procedure.

An undesired cross-talk effect in the TPC front-end electronics has been found and traced to a capacitive coupling between the input and output of the preamplifiers. The cross-talk analog signals have an area which is, on average, $\sim$5% of that of the inducing signal. However, because of the different pulse shape, after the digitization process, these cross-talk signals can produce areas which reach $\sim$25% that of the original signal. A model has been identified, developed and tested to achieve a reduction of one order of magnitude in the cross-talk intensity.

8. RESUMEN EN ESPAÑOL

8.1 Sumario

En el capítulo 1 se describen las motivaciones y objetivos del experimento HARP. El experimento ha sido motivado por la falta de datos experimentales necesarios para calcular con precisión el flujo hadrónico producido en la atmosféra por los rayos cósmicos, y que resulta en el flujo de neutrinos atmosféricos, así como el generado en aceleradores (al incidir un haz de protones sobre un blanco pesado) y utilizado para crear haces de neutrinos. Así pues, el objetivo del experimento es la medida de la sección eficaz de producción de hadrones secundarios en colisiones protón-nucleo con momento del protón incidente de entre 2 a 15 GeV/c, rango en el que la falta de datos experimentales es más acusada.

En el capítulo 2 se describe el aparato experimental de HARP. Un haz de protones y piones incide sobre blancos fijos produciendo hadrones secundarios que son detectados y medidos por varios subdetectores. Uno de los principales subdetectores del experimento, la Cámara de Proyección Temporal, no se describe en este capítulo por hacerse en uno aparte. Los demas subdetectores son descritos dando énfasis a su funcionalidad.

En el capítulo 3 se describen los principios de funcionamiento de una Cámara de Proyección Temporal (TPC), uno de los subdetectores más importantes del experimento. Una TPC es un detector de gas con capacidad para identificar partículas y reconstruir sus trayectorias en tres dimensiones. La detección de partículas con este tipo de detectores implica diferentes procesos, principalmente: ionización del gas, deriva de electrones de baja energía a través del gas y creación de avalanchas en una cámara de hilos.

En el capítulo 4 se describe la TPC del experimento HARP. Haciendo referencia a los principios de funcionamiento descritos en el capítulo anterior se detallan la estructura mecánica del detector, su configuración electrostática, la mezcla de gas usada en su operación, la electrónica -analógica y digital- de lectura de las señales, el sitema de adquisición de datos, el sistema de alto voltage y el sistema de refrigeración.

En el capítulo 5 se describe el sistema de calibración por láser de la TPC. Este sistema se basa en una nueva técnica que hemos desarrollado en el experimento. Esta consiste en una matriz de fibras ópticas uno de cuyos extremos está recubierto de una fina capa de aluminio, mientras que el otro está conectado a un emisor de luz láser ultra violeta. Los extremos aluminizados de las fibras están precisamente colocados dentro del volumen de detección. Impulsos de luz laser arrancan fotoelectrones de los extremos de las fibras ópticas. Dichos fotoelectrones, cuyo origen se conoze con precisión, derivan a través de todo el volumen activo del detector y producen las señales de calibración. El funcionamiento de la técnica ha sido probado en un prototipo. En este también se han medido los parámetros relevantes para el diseño de un sistema apropiado para el detector final. Dicho sistema ha sido diseñado, construido e implementado en la TPC del experimento HARP.

En el capítulo 6 se tratan las señales electrónicas de los canales de lectura de la TPC.

Se caracterizan las señales analógicas y se describen y comparan los diferentes métodos de extracción de información de las señales una vez digitalizadas. En la electrónica analógica, llamada de “front-end”, hemos encontrado un effecto de “cross-talk” entre canales. Hemos llevado a cabo una serie de medidas con el fin de localizar, cuantificar, y modelizar este efecto efecto. Dichas medidas consisten básicamente en la excitación de determinados canales mientras las señales inducidas en todos los canales son registradas y estudiadas “a posteriori”

8.2 Motivación

El experimento HARP está llevando a cabo la medida de hadrones secundarios -para todo ángulo sólido- producidos en blancos fijos por haces de protones con momento entre 2 y 15 GeV/c. El objetivo es realizar la medida de las secciones eficazes -total y diferencial- de producción de hadrones en este rango de momento con una precisión del 2%. Las motivaciones físicas de tal medida son las siguientes:

- Mejorar substancialmente el cálculo del flujo de neutrinos atmosféricos. Esto es necesario para contribuir a una interpretación detallada de la reciente evidencia de oscilaciones experimentadas por los neutrinos producidos en la atmósfera. El actual conocimiento del flujo de neutrinos atmosféricos está dominado por un error del 30%. Las fuentes de este error son la falta de conocimiento, por una parte, del espectro y composición química de los rayos cósmicos primarios, y por otra, de la producción hadrónica en las colisiones entre rayos cósmicos y núcleos de nitrógeno y oxigeno que tienen lugar en la atmósfera. El flujo, espectro y composición química de los rayos cósmicos está siendo medido en la actualidad por una serie de experimentos y se espera que en un par de años, el error en estas magnitudes será negligible en cuanto se refiere a la determinación del flujo de neutrinos atmosféricos. Esto deja a la producción hadrónica como el último obstáculo para el cálculo preciso del flujo de neutrinos atmosféricos.

- Mejorar substancialmente el cálculo del flujo de neutrinos en los haces ya existentes. Actualmente, en el “Fermilab booster neutrino beam-line” y el “KEK PS neutrino beam-line” se producen haces de neutrinos de gran intensidad a partir de haces intensos de protones de baja energía (8 y 12 GeV/c respectivamente) que inciden sobre blancos fijos. Las propiedades de estos haces no se pueden calcular con precisión si no es con la aportación de datos experimentales hecha por HARP. Por esta razón, HARP a llevado a cabo, en colaboracion con los experimentos MiniBoone y K2K que usan los haces del Fermilab y del KEK PS respectivamente, una serie de medidas con los blancos usados para producir dichos haces.

- Optimizar el diseño del blanco de una “Neutrino Factory”. La “Neutrino Factory” es una máquina propuesta en la que se producen neutrinos a partir de la desintegración de muones que circulan en un anillo de almacenamiento. En esta máquina un haz intenso de protones de bajo momento (pocos GeV/c, se barajan distintas posibilidades en distintas propuestas) incide sobre un blanco fijo produciendo hadrones secundarios, que a su vez se desintegran generando los muones que son almacenados en un anillo de almacenamiento. Las actuales simulaciones de la produccion hadrónica conllevan

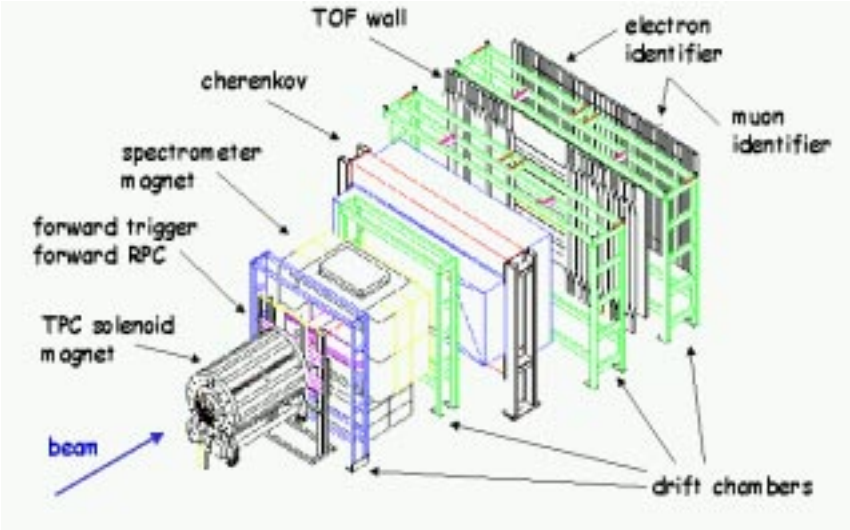

Fig. 8.1: El sistema experimental de HARP.

discrepancias del 30 al 100% debido a la modelización de este mecanismo junto con la falta de datos experimentales.

8.3 El aparato experimental

Como se ha dicho en la sección anterior, el objetivo del experimento es la medida, en bines de momento y ángulo sólido, de la producción hadrónica en blancos fijos por un haz de protones de momento entre 2 y 15 GeV/c. Esto es equivalente a contar las partículas secundarias de cada especie en bines de momento y ángulo sólido:

$$\frac{d\sigma}{dpd\Omega} = \frac{N(p,\Omega)}{\phi} \tag{8.1}$$

donde ϕ es el flujo incidente.

El dispositivo experimental consiste en un blanco fijo en el que incide un haz de protones de momento regulable entre 2 y 15 GeV/c y con una resolución del 0.24%, y un sistema de 15 subdetectores que permite la medida del momento de las partículas secundarias y su identificación en todo el ángulo sólido con máxima eficiencia. Es necesario en este punto decir que para abaratar la construcción del experimento se ha explotado al máximo posible el material y equipamiento ya existente. La Fig. 8.1 muestra un esquema del aparato. En referencia a los subdetectores más importantes, podemos considerar dos zonas diferentes del detector: un espectrómetro delantero, que cubre el cono delantero del ángulo sólido y un espectrómetro de gran ángulo que, rodeando el blanco, cubre la parte del ángulo sólido fuera del cono delantero.

En el espectrómetro delantero, se identifican las partículas mediante un detector de umbral de luz Cherenkov y un detector de tiempo de vuelo. Estos dos sistemas cubren regiones distintas del rango de momento de las partículas secundarias y se complementan por un calorímetro electromagnético y un detector de muones. En el espectrómetro delantero, tanto

la medida del momento de las partículas secundarias como el traceo de sus trayectorias se hace mediante un conjunto de cámaras de deriva que miden la desviación sufrida por las partículas al atraversar el campo magnético generado por un dipolo.

8.4 La Cámara de Proyección Temporal

8.4.1 Principios de funcionamiento

Una Cámara de Proyección Temporal es un detector de gas con capacidad para reconstruir las trayectorias de las partículas tridimensionalmente así como de medir su pérdida de energía en el medio del detector. Consiste en un volumen de gas y una camara de hilos, sumergidos en un campo eléctrico, a menudo complementado por un campo magnético que permite la medida del momento de las partículas cargadas. Una partícula cargada que atraviesa el volumen activo ioniza y excita las moléculas del gas a lo largo de toda su trayectoria. Los campos eléctrico y magnético estan orientados de manera tal que los electrones generados a lo largo de la trayectoria de la partícula derivan hacia la cámara de hilos a velocidad constante. La cámara de hilos registra la posición bidimensional de dichos electrones en el plano perpendicular a su movimiento de deriva. La coordenada restante se determina a partir del tiempo de deriva de los electrones (que es el tiempo transcurrido entre el paso de la partícula a traves del volumen activo, típicamente registrado por otro detector y la llegada de los electrones a la cámara de hilos). La magnitud y orientación de los campos eléctrico y magnético, así como la naturaleza, presión y temperatura del gas del volumen activo se escogen de tal manera que generen una velocidad de deriva constante y uniforme en todo el volumen de detección. La medida de la curvatura de las trayectorias de las partículas, debida al campo magnético, permite la determinación del momento de estas. A partir de la amplitud de las señales, combinado con la apropiada calibración del detector, puede medirse la pérdida de energía de la partícula en el medio. La combinación de estas dos medidas permite identificar la partícula.

8.4.2 La Cámara de Proyección Temporal de HARP

La TPC del experimento HARP tiene forma cilíndrica con el eje de simetría coaxial al haz primario, Fig 8.2. Su estructura básica está formada por dos cilindros coaxiales de radios diferentes que confinan el volumen de detección del aparato. El cilindro menor aloja en su interior -fuera del volumen activo- el blanco en el que ocurren las interacciones. Los dos extremos del volumen de detección estan cerrados por placas sujetas al cilindro exterior. Una de las placas, la de la parte por la que llega el haz al detector, sirve de soporte al cilindro menor y a la electrónica de lectura. Los campos eléctrico y magnético están orientados paralelamente al eje de simetría del detector. El campo eléctrico se genera por un sistema de tiras metálicas sujetas a las superficies internas de los cilindros y mantenidas a potenciales precisos, cuya intensidad se degrada controladamente a lo largo del cilindro. Un solenoide que rodea la TPC genera el campo magnético. El gas usado es una mezcla de argón y metano (91%-9%) cuyas propiedades son conocidas y que ya ha sido usado previamente en este tipo de detectores en los experimentos ALEPH y DELPHI en el CERN. Uno de los extremos del volumen, el de la parte por la que llega el haz al detector, esta instrumentado con una cámara de hilos paralela a dicha y, además, contiene la electrónica de lectura. La cámara de hilos está compuesta por un plano de “pads” de lectura, un plano de hilos que funciona como ánodo,

un plano de hilos que funciona como cátodo y un plano de hilos que, mediante el potencial al que estan los hilos, deja pasar o no los electrones de deriva hacia la cámara y los iones desde esta hacia el volumen activo, Fig 8.3. El ancho total de la cámara es de 21 mm y cubre el 97% del volumen activo de la TPC. El plano de “pads” está físicamente impreso en la misma carta de circuito estampado (PCB) que contiene la electrónica de “front-end”. Las señales analógicas inducidas en los pads son digitalizadas por un ADC (Analog to Digital Converter) de 10 bits de precisión y registradas por un sistema de adquisición de datos.

8.5 El sistema de calibracion láser de la TPC

En una TPC con campos eléctrico y magnético paralelos, como la de HARP, el efecto de un pequeño desalineamiento entre ambos resulta en un desplazamiento de cada elemento de traza proporcional a la longitud de deriva de los electrones. De la experiencia existente, por ejemplo ALEPH [60] y DELPHI [61], se sabe que las distorsiones de los campos eléctrico y magnético necesitan ser evaluadas. Esto se puede hacer mirando donde se reconstruyen los electrones de deriva cuyo origen se conoce con precisión. En otros experimentos [60] [61] se han utilizados haces de luz láser que ionizan directamente el gas dentro de la TPC [45]. En el experimento HARP hemos desarollado una técnica basada en fuentes puntuales de fotoelectrones situadas con precisión dentro del volumen del detector. Dichas fuentes consisten en fibras ópticas de quarzo uno de cuyos extremos está conectado a un emisor de luz laser de 248 nm de longitud de onda y el otro está recubierto por una capa de aluminio de entre 80 y 120 Å de espesor y que se posiciona dentro del volumen del detector. Cuando un impulso de luz láser incide sobre la capa de aluminio se emiten fotoelectrones, produciendo las señales de calibración.

El funcionamiento de la técnica se probó en el prototipo de la Fig 8.4. Este consiste en un volumen de deriva rectangular, cerrado por membrana de Mylar aluminizado por una parte,

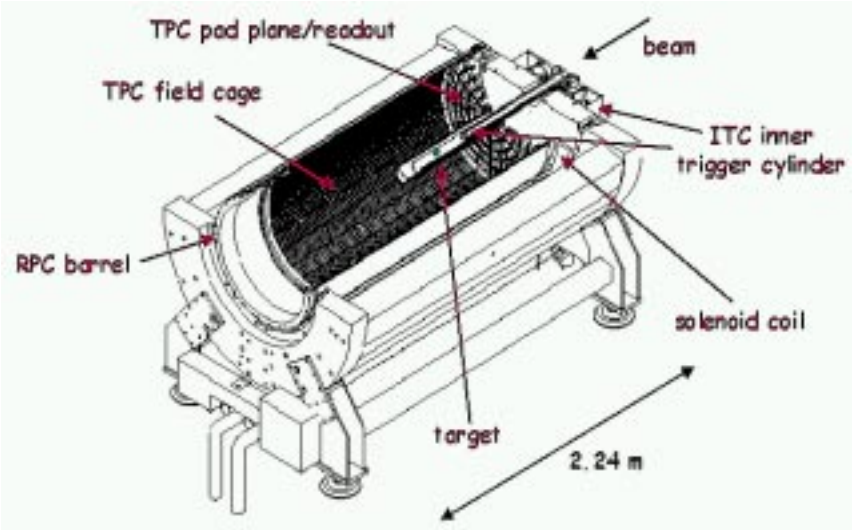

Fig. 8.2: Esquema de la TPC donde se pueden ver la TPC, el solenoide y el soporte de los blancos.

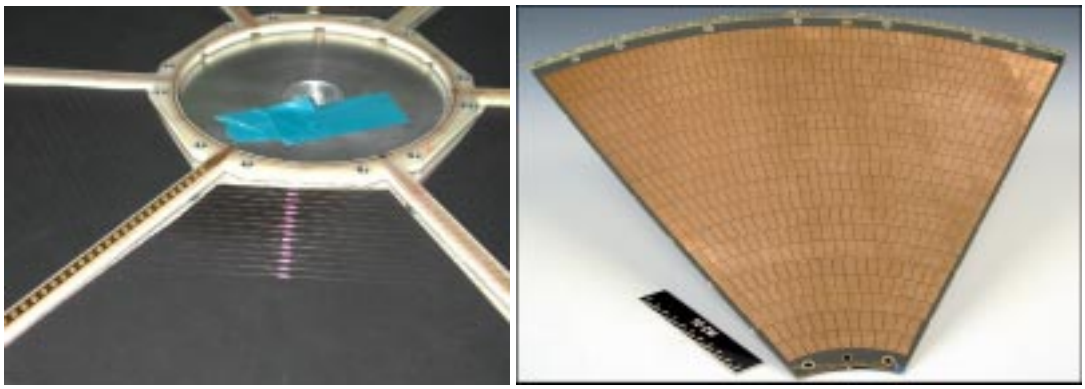

Fig. 8.3: Fotografías de uno de los planos de hilos (izquierda) y de un sector de pads de lectura (derecha) antes de ser montados en la TPC.

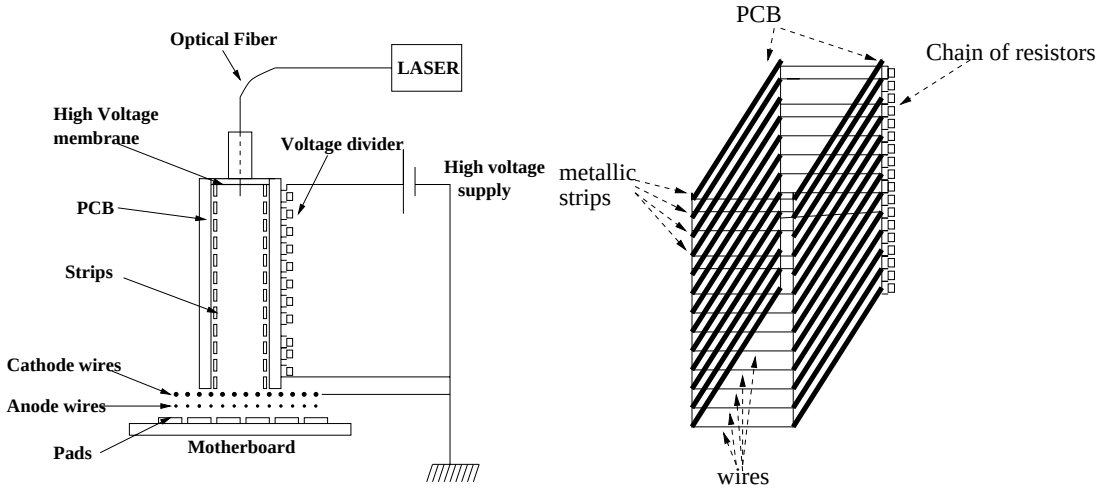

Fig. 8.4: Esquema del prototipo (izquierda) y del "field cage" que genera el campo eléctrico dentro del volumen del prototipo (derecha).

y por una cámara de hilos por la otra. Esta última ha sido construida con los mismos componentes usados también en la TPC siempre que la geometría lo ha permitido. Como indica la Fig 8.4, se ha introducido en el volumen de deriva el extremo aluminizado de una fibra óptica conectada a un laser que emite impulsos de luz ultra violeta. Con este dispositivo, además de probar el funcionamiento de la técnica, hemos medido los parámetros relevantes a la construcción del sistema de calibración de la TPC: espesor de aluminio a depositar en los extremos de las fibras, longitud de onda de la luz láser, radio de las fibras, energía mínima necesaria para generar una señal detectable en la cámara (en función de la longitud de onda) y las dimensiones espaciales de las señales de calilbración, determinadas por la "Pad Response Function", Fig 8.5.

El sistema que hemos construido para la TPC de HARP consiste en 198 de estas fibras cuyos extremos aluminizados están situados en la placa que cierra el volumen del detector (por la parte opuesta a la que aloja la cámara de hilos). El número de fuentes usadas se ha

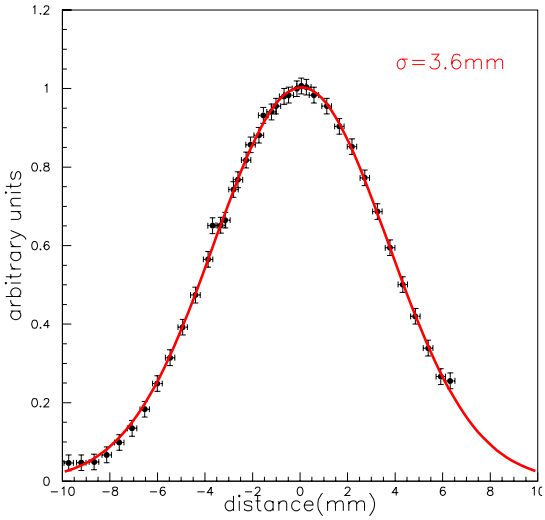

Fig. 8.5: "Pad Response Function" medida en el prototipo. Su medida ha sido posible gracias a la posibilidad de desplazar el volumen de deriva, y así el extremo aluminizado de la fibra, con respecto a la cámara de hilos.

escogido de manera tal que proporcione el máximo de redundancia, sin provocar la superimposición de señales provenientes de distintas fuentes. Las fuentes están distribuidas en el plano de la placa que las soporta de manera que se puedan evaluar tanto las distorsiones del detector como sus dependencias radiales y angulares. Los fotoelectrones emitidos derivan a lo largo de todo el detector y, al llegar a la cámara de hilos, producen las señales de calibración. Esta técnica permite la medida de distorsiones; la medida del tiempo de deriva; la medida de la retroalimentación de iones y la medida de la estabilidad del detector, todo ello en tiempo real. Debido a que todos los fotoelectrones se crean en el extremo opuesto de la cámara de hilos, sólo se pueden determinar correcciones integrales. A pesar de ello, esta información permite la cuantificación de las distorsiones generadas ya sea por la heterogeneidad del campo magnético con respecto al eléctrico o por la estructura de la cámara de hilos, Fig 8.6.

8.6 Las señales analógicas de la TPC

8.6.1 Estimadores de carga y tiempo de ocurrencia de las señales

En la Fig 8.7 se puede ver una señal análogica típica de un canal de lectura de la TPC. Cuando el sitema de detectores que forman el "trigger" detecta una partícula dentro de la TPC manda una señal al sistema de Adquisición de Datos (DAQ) y las señales generadas en la TPC son digitalizadas y registradas en una base de datos. Un "Analog to Digital Converter" (ADC) muestrea las señales analógicas con una frecuencia de 10 MHz, o sea, toma una muestra cada 100 ns. Al recibir la orden, el sistema de DAQ necesita un tiempo entre 0 y 100 ns para sincronizar los 4000 canales de los que consta la TPC. Este tiempo varía de un suceso a otro siguiendo una distribución plana y recibe el nombre de "jitter". Este proceso resulta en un desfase entre distintas digitalizaciones de una misma señal analógica, hechas en

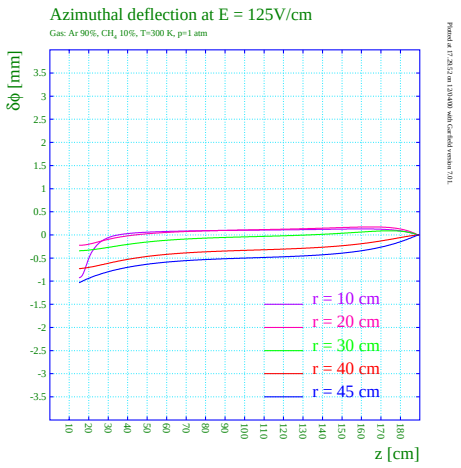

Fig. 8.6: Deflección azimutal. Según las simulaciones de Monte-Carlo [34], las distorsiones del campo magnético con respecto al eléctrico son más severas en las zonas vecinas a la cámara de hilos y a los límites del volumen activo.

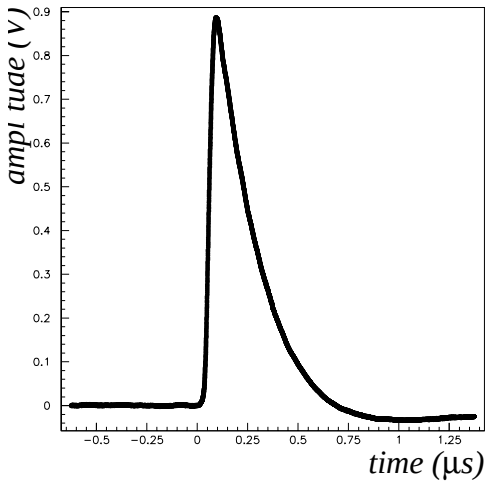

Fig. 8.7: Una señal analógica típica registrada con un osciloscopio digital.

sucesos distintos. Debido al rápido tiempo de subida de las señales analógicas, ∼50 ns, con respecto al "jitter", 100 ns, diferentes digitalizaciones de impulsos idénticos pueden diferir substancialmente dependiendo de la fase del "jitter". Esto resulta en una limitación de la resolución de los estimadores de la carga y del tiempo de ocurrencia de los impulsos.

Nosotros hemos estudiado estas resoluciones simulando el proceso de digitalización (incluyendo el jitter) sobre las señales analógicas generadas experimentalmente en una serie de canales mediante una sonda directamente soldada en los pads de lectura de un sector de repuesto, y medidas con un osciloscopio digital. Para reproducir las señales generadas por una partícula cargada dentro de la TPC, ha sido necesario utilizar el "leading edge" de una

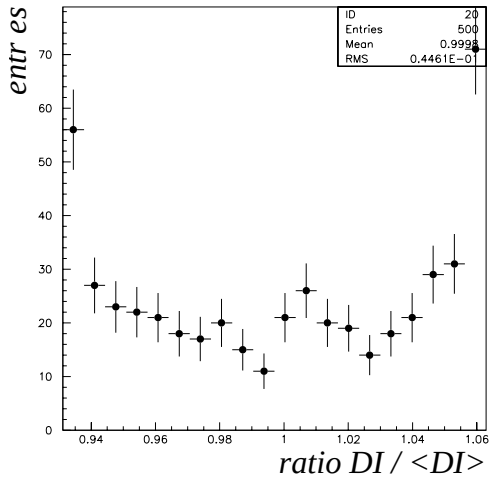

Fig. 8.8: Izquierda: Distribución del estimador DI, dividido por el valor medio de la distribución, obtenida al digitalizar 500 veces el mismo impulso.

función escalón que llega al pad a través de una capacidad de 15 pF. Hemos simulado la digitalización de estas señales un total de 500 veces y las resolución de los estimadores se ha determinado en estas muestras. La Fig 8.8 muestra la distribución del estimador DI definido como la suma de todos las medidas discretas de la amplitud en un pulso. Con estimadores veloces, como DI o el máximo de las medidas discretas de la amplitud en un impulso, se consiguen una resolución de reconstrucción de la carga y del tiempo de ocurrencia comparables a la obtenida ajustando las medidas discretas a las formas de los impulsos esperadas (siendo del orden del 5% para la carga y de 25 ns para el tiempo de ocurrencia).

El efecto del "jitter" se traduce en la dispersión y no gausianidad de la distribución de los valores de un estimador determinado obtenidas en distintas digitalizaciones del mismo ipulso, como muestra la Fig 8.8.

Nosotros hemos construido estimadores del "jitter" a partir de la medida de la respuesta de los preamplificadores. Por ejemplo, uno de estos estimadores es el cociente entre la máxima medida discreta de la amplitud y el valor de la medida tomada inmediatamente después de la máxima. Explotando las correlaciones existentes entre los valores de los estimadores de carga y tiempo con los del "jitter" hemos construido funciones de correción para los primeros, Fig 8.9, que, aplicadas, mejoran las resoluciones de los estimadores de carga en un orden de magnitud (0.3 %) y la del tiempo de ocurrencia de los impulsos hasta $\sim$ 12 ns.

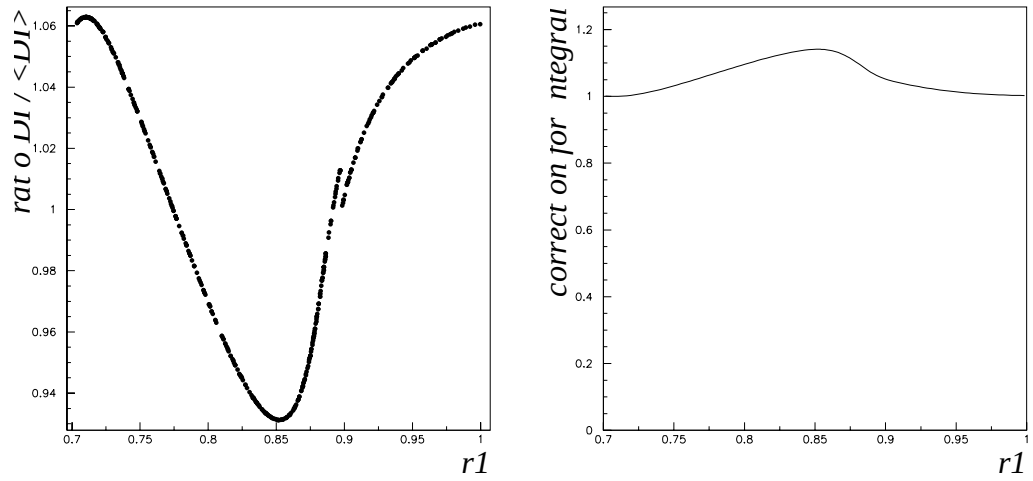

Fig. 8.9: Izquierda: Correlación entre el valor del estimador DI y el del estimador del jitter. Derecha: Función de correción de DI en función del valor del estimador del jitter. La función se ha construido a partir de los datos de la figura a la izquierda.

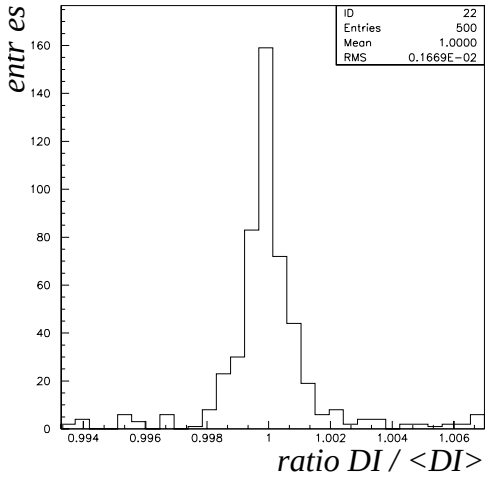

Fig. 8.10: Izquierda: Distribución del estimador corregido $DI/ < DI >$. La correcion se ha llevado a cabo mediante la función de la Fig 8.9. La muestra corregida es diferentede la usada para costruir la función de correción.

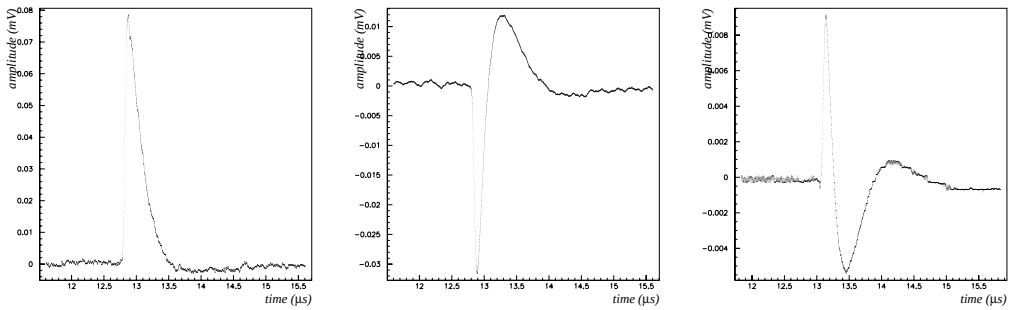

Fig. 8.11: Tipos de señal observados: (izquierda) excitación directa, (centro) "cross-talk" de primer orden, (derecha) "cross-talk" de segundo orden.

8.6.2 Cross-talk

Entre ciertos canales de la electrónica analógica de "front-end", hemos observado un efecto no deseado de "cross-talk". Hemos encontrado el origen de este efecto en el acoplamiento capacitivo entre la salida de ciertos preamplificador y la entrada de otros. Dicho acomplamiento es debido a la proximidad física -dentro de la carta de circuito estampado que contiene la electrónica- entre conductos que trasportan señales sin amplificar y conductos que trasportan señales ya aplificadas. Para identificar las relaciones existentes de "cross-talk", y para modelizar y cuantificar el efecto, hemos llevado a cabo una serie de tests en dos sectores de repuesto de la carta.

Uno de los sectores ha sido montado en un sistema que permite la excitación de los pads por medio de una sonda conectada a un generador de funciones. La sonda es un simple conductor que se sitúa en frente de los pads. Para producir una señal equivalente a las generadas por una avalancha, es necesario aplicar a la sonda un escalón de potencial. Debido a que la distancia entre el pad y la sonda no se controla con precisón, la señal de entrada es diferente para pads diferentes y no se pueden llevar a cabo, con este dispositivo, estudios cuantitativos de la intensidad del "cross-talk". Además del pad excitado, la sonda también excita los pads colindantes con una señal del $\sim$ 10% de la del pad central, que se superimpone a una posible señal de "cross-talk", dificultando así su identificación. Con el fin de hacer un mapa digital de las relaciones de "cross-talk", hemos excitado todos los pads del sector uno por uno, y las señales generadas en todos los canales han sido registradas por medio del sistema de adquisición de datos de la TPC. Hemos deducido la eficiencia y pureza del mapa así obtenido, por comparación con el mapa obtenido con el dispositivo descrito a continuación, ideado para evitar los problemas intrínsecos de este sistema y poder realizar estudios cuantitativos.

En el otro sector, hemos excitado un total de 46 pads por medio de una sonda directamente soldada sobre ellos. Los pads son excitados con una función delta de potencial conseguida a partir de un escalón de potencial y una capacidad. Este sistema garantiza la identidad de la señal en la entrada de los "pads" y la excitación de un solo pad a la vez. Para cada pad excitado, las señales generadas en los demás canales han sido registradas por medio de un osciloscopio digital de 2.5 Gs/s. La Fig 8.11 muestra los tres tipos de señal observados que corresponden a: la señal directa, la señal de "cross-talk" primario y la señal

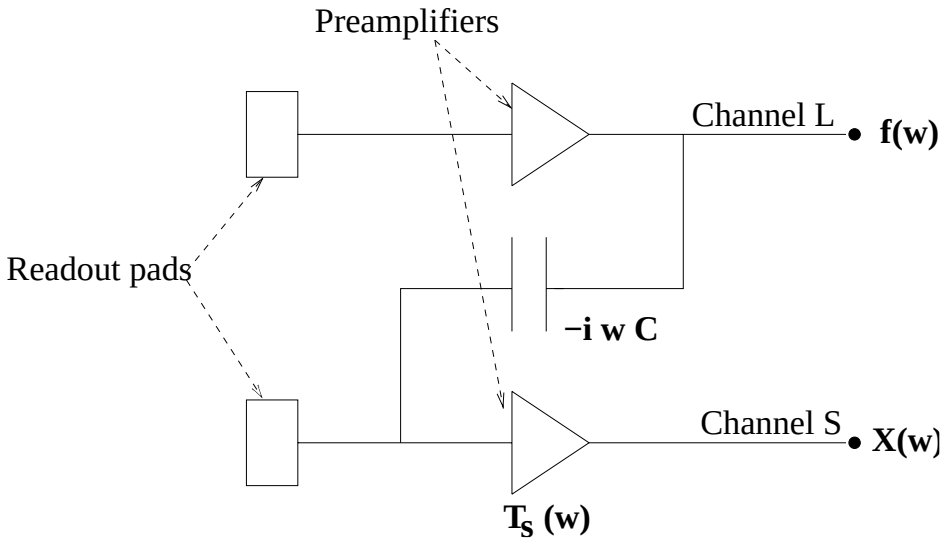

Fig. 8.12: Esquema del acoplamiento entrada-salida.

de “cross-talk” secundario. El “cross-talk” secundario es la señal de “cross-talk” generada por una señal que, a su vez, era ya de “cross-talk”. Tenemos la intención de reproducir las señales de “cross-talk” estudiando, en el espacio de Fourier, la respuesta de los preamplificadores, y considerando un acoplamiento capacitivo entre la salida del canal inductor y la entrada del canal receptor, Fig 8.12.

La señal de cross-talk en el canal “S”, $X(w)$, que resulta de una excitación arbitraria del pad “L” que, a su vez, genera una señal $f(w)$ en el canal “L” es:

$$X(w) = -iw\, C_{L\to S}\, f(w)\, T_S(w) \tag{8.2}$$

donde $C_{L\to S}$ es la capacidad del acoplamiento entre los canales “L” y “S”.

En la hipótesis de que la señal inyectada a la entrada de los preamplificadores es una delta de Dirac con carga Q, la señal a la salida de los preamplificadores es la respuesta de éstos en el espacio de tiempo, y su transformada de Fourier, la respuesta en el espacio de frecuencias. Si $g_i(t)$ es la señal observada en el canal i cuando éste es excitado, la respuesta de este canal en el espacio de frecuencias puede ser calculada como:

$$T_i(w) = \frac{FFT\{g_i(t)\}}{Q} \tag{8.3}$$

Donde Q permanece como una constante desconocida y FFT significa la transformada rápida de Fourier. Aplicando la fórmula 8.3 a la fórmula 8.2 se puede calcular la forma de la señal de “cross-talk” inducida en el canal “S”, cuando en el canal “L” se observa una señal $g_L(t)$ producto de su excitación, como:

$$X(w) = -iw\, FFT\{g_L(t)\}\, FFT\{g_S(t)\} \tag{8.4}$$

Donde $g_S(t)$ es la respuesta del canal “S” al ser escitado. La Fig 8.13 muestra una señal de “cross-talk” tpica, superpuesta a la predicción resultante de aplicar el modelo explicado, una

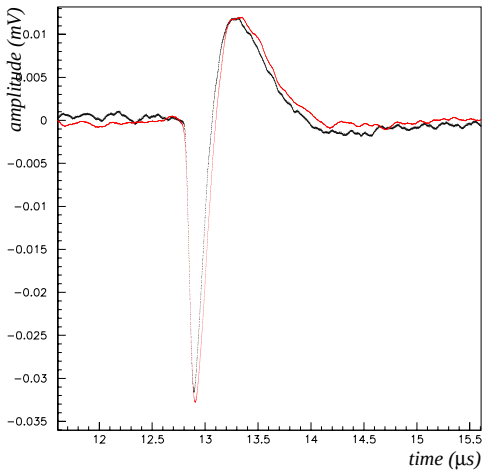

Fig. 8.13: Senñal de “cross-talk” registrada con el osciloscopio (en negro) , superpuesta a la predicha por el modelo (en rojo) una vez normalizadas como se explica en el texto.

vez normalizadas a mano la una a la otra. El modelo se ajusta a los datos satisfactoriamente.

Hemos probado la robustez y la capcidad predictiva del modelo mediante su aplicación a señales inducidas por preamplificadores sobrecalentados y por preamplificadores es saturación. Considerando la nomenclatura de la Fig 8.12, hemos calentado el premaplificador “L” para conseguir a su salida, cuando es excitado, una señal oscilante, Fig 8.14 (izquierda). Hemos estudiado la señal de cross-talk generada en el canal “S”. Como muestra la Fig 8.14 (derecha), el modelo predice esta señal satisfactoriamente aún cuando la señal de entrada al preamplificador “S” es muy distinta de la normal.

Para probar la linearidad del modelo hemos repetido las medidas descritas al principio de esta sección pero con diferentes amplitudes de las señales de entrada a los pads, hasta llegar a señales de entrada un orden de magnitud mas grandes que las usadas anteriormente, con el fin de llevar el comportamiento de los premplificadores a la saturación, Fig 8.15. Aparte de dicha saturación, que el modelo no tiene en cuenta por usar funciones de transferencia medidas en el régimen lineal, la predicción del modelo reproduce satisfactoriamente las señales medidas, Fig 8.15, y muestra que el efecto de cross-talk es, como se esperaba, lineal.

También hemos aplicado el modelo a señales de “cross-talk” secundario obteniendo resultados satisfactorios.

La magnitud de la señal de “cross-talk” depende de los valores de $C_{L\to S}$ y Q. Como Q es una constante que no depende de la identidad de los canales excitados, la constante de normalización que se obtiene al ajustar el modelo a los datos es una medida directa de la capacidad de acoplamiento (excepto un factor de escala).

8.7 Conclusiones

Para la calibración de la Time Projection Chamber hemos diseñado, desarrollado y construido un nuevo sistema de calibración. El aparato consiste en una matriz de fuentes puntuales de fotoelectrones posicionadas con precisión dentro del volumen del detector. Estas fuentes son extremos de fibras ópticas de quarzo en los que hemos depositado una fina capa de aluminio ($\sim$80 $\mathring{A}$). Las fibras guían luz láser ultravioleta que, al incidir sobre el aluminio arranca fotoelectrones. Los extremos aluminizados de las fibras están afirmados sobre la membrana de alto voltage de la TPC. Los fotoelectrones emitidos derivan dentro del detector y producen las señales de calibración. La técnica permite evaluar las distorsiones $\vec{E} \times \vec{B}$ y la medida de la velocidad de deriva, retroalimentación de iones y estabilidad del detector.

Hemos caracterizado las señales analógicas generadas por la electrónica de front-end. Hemos estudiado y comparado diferentes métodos de extracción de la amplitud de los pulsos y del tiempo de su ocurrecia una vez digitalizados. Con estimadores rápidos de estas cantidades, como la suma de todas las medidas discretas de la amplitud en un mismo impulso, hemos obtenido una resolución de reconstrucción comparable a la obtenida al ajustar las medidas discretas de amplitud a la forma de los impulsos esperada. Las resoluciones relativas obtenidas ($\sim$ 5%) están limitadas por efecto de "aliasing". Estas pueden ser mejoradas en un orden de magnitud aplicando una correción a los valores de los estimadores que se construye a partir del conocimiento de la respuesta del preamplificador y del proceso de digitalización.

Hemos observado un no deseado efecto de "cross-talk" en la electrónica de "front-end" de la TPC. Hemos identifcado su origen en el acoplamiento capacitivo entre la entrada y la salida de los preamplificadores. Las señales analógicas de "cross-talk" tienen un área, en promedio, del $\sim$ 5% la de la señal que las induce. Sin embargo, debido a la diversa forma de estas señales, una vez digitalizadas sus áreas pueden llegar a alcanzar el $\sim$ 25% la de la señal que las induce. Hemos desarrollado un modelo de este efecto que reproduce satisfactoriamente las observaciones experimentales y cuya aplicación permite reducir en un orden de magnitud la intensidad del "cross-talk".

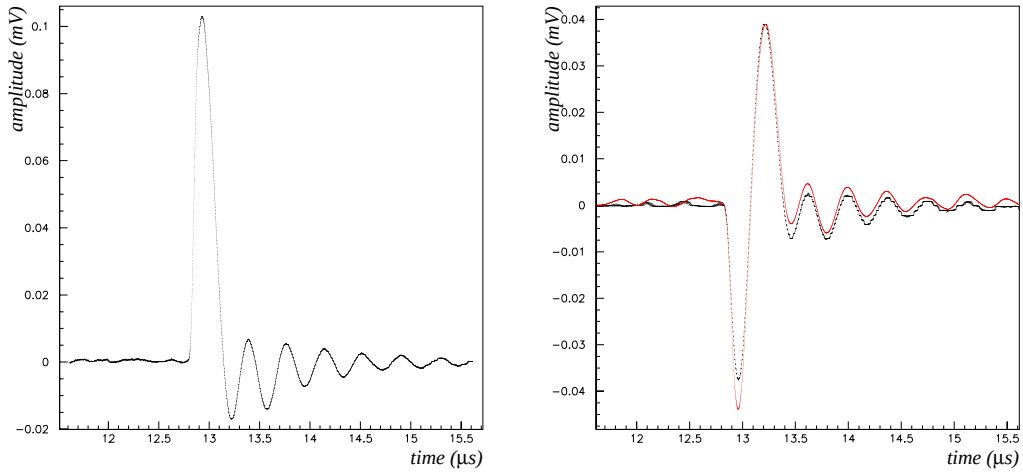

Fig. 8.14: Izquierda: Señal oscilante generada por un preamplificador sobrecalentado cuando es excitado como se indica en el texto. Derecha: Señal de cross-talk inducida por la señal de la izquierda. La curva negra (oscura) corresponde a la señal medida, mientras que la roja (clara) corresponde a la predicha por el modelo, una vez normalizada.

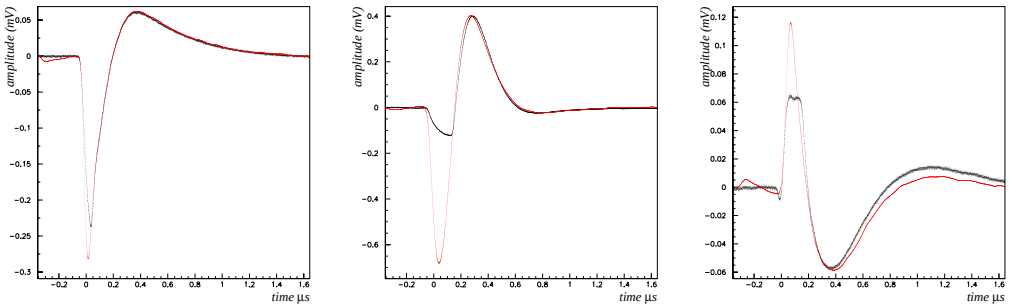

Fig. 8.15: Señales de cross-talk generadas por una señal a la entrada de los pads lo suficientemente grande como para saturar los preamplificadores. La figura de la izquierda(centro) corresponde a la señal de cross-talk de primer orden generada en un preamplificador cercano a la saturación (en saturación completa para la figura del centro). La figura de la derecha corresponde a la señal de cross-talk secundario donde el preamplificador intermedio está en saturación. Notar que, aparte el efecto de saturación que el modelo no tiene en cuenta,el modelo reproduce los datos satisfactoriamente.

BIBLIOGRAPHY

[1] Pion Production in Proton Collisions With Light Nuclei: Implications for Atmospheric Neutrinos. Engel *et al.* November 16, 1999. hep-ph/9911394

[2] Flux of Atmospheric Neutrinos. hep-ph/0203272. To be published in Annual Review of Nuclear & Particle Science Vol. 52 in December 2002

[3] Webber WR. Golden RL, Stephens SA. Proc. 20th Int. Cosmic Ray Conf. 1:325 (1987)

[4] Seo E-S, et al. Astrophys. J. 378:763 (1991)

[5] Pappini P, et al. Proc 23rd Int Cosmic Ray Conf. 1:579 (1993)

[6] Boezio M, et al. Astrophys. J. 518:457 (1999)

[7] Menn W, et al. Astrophys. J. 533:281 (2000)

[8] Sanuki T, et al. Astrophys. J. 545:1135 (2000)

[9] Alcarez J, Phys. Lett. B490:27 (2000)

[10] Ryan MJ, Ormes JF, Balasubrahmanyan VK. Phys. Rev. Lett. 28:985, E1497 (1972)

[11] Asakamori K, et al. Ap. J. 502:278 (1998)

[12] Ivanenko IP, et al. Proc 23rd Int. Cosmic Ray Conf. 2:17 (1993)

[13] Kawamura Y, et al. Phys. Rev. D40:729 (1989)

[14] Apanasenko AV, et al. Atropart. Phys. 16:13 (2001)

[15] Y. Fukuda et al., Phys. Lett. B227 (1999) 9.

[16] A. Blondel et. al. MICE-NOTE-GEN-0004. http://hep04.phys.iit.edu/cgi-bin/noteModSel

[17] Garoby, R. "Current Activities for a Neutrino Factory at CERN" CERN-OPEN-2001-040.

[18] Biagio Saitta. Oscillations with laboratory neutrinos. Nuc. Phys. B Proc. Sup., Vol. 100(1-3) 217-231 (2001)

[19] A. Alfred, I.F. Christoph. Layout of the new CERN neutrino beam. CERN Yellow Report CERN-66-24, 4 Jul 1966.

[20] E. Church et. al.. A proposal for an experiment to measure $\nu_\mu \rightarrow \nu_e$ oscillations and ν_μ disappearence at the Fermilab Booster: BooNE. December 7, 1997. http://www-boone.fnal.gov/

[21] Y. Oyama. K2K neutrino-oscillation experiment at KEK-PS. hep-ex/9803014. 18/3/98

[22] Y.Itow et al. The JHF-Kamioka neutrino project. hep-ex/0106019 (5/06/01)

[23] A 2 GeV superconducting proton linac at CERN. http://ps-div.web.cern.ch/ps-div/SPL_SG/

[24] T.Eichten *et al.* Nucl. Phys. B44 (1972) 333

[25] J.V.Allaby *et al.* CERN Yellow Report 70-12, 1970

[26] T.Abbott *et al.* Phys. Rev. D45 (1992) 3906

[27] D.D Armutliiski et al. Sov. J. Nucl. Phys 48(1) (1998) 101

[28] H.N. Agakishiyev et al: Z Phys C 27 (1985) 177

[29] B.Cole *et al.* BNL Proposal 910 (1994), AGS proposal: "A Facility to study proton-nucleus and heavy ion collisions using a large acceptance detector with particle identification capabilities"

[30] D.M Ritson. Techniques of high energy physics.Interscience publishers, Inc., New York 1961

[31] W.W.M Allison and J.H. Cobb. Ann. Rev. Nucl. Sci 30, 253 (1980)

[32] Harris et al. 1977

[33] http://magboltz.web.cern.ch/magboltz/

[34] Rob Veenhof web page: http://rjd.home.cern.ch/rjd/

[35] N.I. Bozhko *et al.* Sov. J. Nucl. Phys. 29(3) (1979) 347

[36] NA56/SPY Colab. Eur. Phys. J. C 10, 605-627 (1999)

[37] The NOMAD Collab. Nucl. Instrum. Methods Phys. Res. A 404 (1998) 96

[38] M. Anfreville et al. Nucl.Instrum.Meth. A481 (2002) 339-364

[39] The CHORUS Collab. Phys. Lett. B 497 (2001) 8

[40] Petr Gourbonov. Private comunication

[41] F. Sauli. CERN Report 77-09 (1977)

[42] Particle Data Group. Review of Particle Physics. Springler, 1998

[43] Agnes Lundborg master thesis. The Time Projection Chamber of the HARP experiment

[44] Proposal to study hadron production for the neutrino factory and for the atmospheric neutrino flux. CERN-SPSC/99-35 15 November, 1999

[45] W.Blum, L.Rolandi. Particle Detection with Drift Chambers. Springler-Verlag (1993)

[46] G.A. Erskine, Nuclear Instrum. Methods 105, 565 (1972)

[47] G. Charpak et. al Nuclear Instrum. Methods 62, 235 (1968)

[48] D.L. Fancher and A.C. Schafer, Experimental study of the signals from segmented cathode drift chambers, IEEE Trans. Nucl. Sci NS-26, 150 (1979)

[49] Christian Joram. Particle Detectors. CERN Academic Training Lectures 1998

[50] Deformation of the HARP TPC wheels. Anders Angantyr Thesis. CERN / TA1 / 00-06

[51] Luciano Musa, private communication

[52] Alice DATE users manual, ALICE-INT-2000-31

[53] W.R. Leo. "Techniques for nuclear and particle physics experiments". Springler-Verlag Heidelberg, 1994

[54] Lohse and Witzeling, Instrumentation in High Energy Physics, World Scientific, 1992

[55] A. Breskin et al. Nuclear Instruments and Methods 124, 189 (1975)

[56] C.M. Davisson "Interaction of Gamma radiation with Matter" in Alpha-,Beta- and Gamma Ray Spectroscopy, ed by K. Siegbahn, North-Holland, Amsterdam 1968)

[57] Yuichi Oyama. hep-ex / 9803014

[58] J. collot et al. Particle production comparisons between MARS, FLUKA and E910, talk given at Nufact'99 in Lyon, to be published in Nucl. Instrum. Meth.

[59] R.L Gluckstem, NIM 24 (1963) 381

[60] Performance of the ALEPH Time Projection Chamber. W.B. Atwood et. al. Nucl. Ins. Meth. A306(1991) 446-458

[61] The DELPHI time projection chamber. Y. Sacquin. Nucl. Ins and Methods. A323(1992)209-212

[62] Valeri Serdiouk, HARP Collaboration meeting Dec. 2001.

[63] http: / / www.goodfellow.com

[64] Lasertechnik Berlin web page: http: / / www.ltb-berlin.de / products.html

[65] CERN Positioning Metrology and Surveying Group. http: / / est-su.web.cern.ch / est-su / SUexperiments.htm

[66] http: / / www.physics.nist.gov / cgi-bin / Xcom / xcom2

[67] http: / / www.lambdaphysik.com

[68] Fast Fourier Transforms have been performed with the C06EAF subroutine of the NAG library (www.nag.co.uk). Inverse transforms have been performed with the C06EBF subroutine of the same library.